University of Nevada, Reno

Pre-eruptive storage constraints of an active crystal mush using mineral-scale techniques

A dissertation submitted in partial fulfillment of the
requirements for the degree of Doctor of Philosophy in
Geology

by

Heather B. Winslow

Dr. Philipp Ruprecht/Dissertation Advisor

May 2023

THE GRADUATE SCHOOL

We recommend that the dissertation
prepared under our supervision by

entitled

be accepted in partial fulfillment of the
requirements for the degree of

Advisor

Committee Member

Committee Member

Committee Member

Graduate School Representative

Markus Kemmelmeier, Ph.D., Dean
Graduate School

Abstract

Crystal mushes are common conceptual models used to interpret the structure of a magmatic reservoirs in many volcanic environments and are drivers of differentiation that can generate explosive silicic eruptions. They are composed of a crystal-rich (45-65 vol%) framework, that may represent a plexus of intrusions, and their high crystallinity produces differentiated interstitial melt that is extracted to form an eruptible crystal-poor silicic melt lens cap. Here, I present a comprehensive study to determine petrologic constraints of an active crystal mush system that is hosted within a continental arc. I focus on crystal-rich mafic enclaves that are interpreted to represent fragments of a crystal mush and were hosted in a crystal-poor rhyolite flow from the 2011-12 eruption of Cordón Caulle, Chile. Mafic enclaves are commonly associated with mafic injection origins, but this study utilizes mineral textures, whole-rock geochemistry, and mineral chemistry and chemical zonation to argue for a more nuanced investigation of highly crystalline enclaves that points toward crystal mush origins. The Cordón Caulle mafic enclaves are basaltic endmembers in comparison to enclaves globally and display interlocking grain textures with simple zonation patterns indicative of slow continual growth within a crystal mush. Melt chemistry from the interstitial glass of the mafic enclaves determined a genetic relationship between the enclaves and their host lavas. This further corroborated the mush conceptual model as opposed to mafic injection magmas that intrude chemically distinct and pre-existing reservoirs. I determine quantitative storage constraints of the crystal mush using a variety of thermobarometers (Mg in plagioclase thermometer, Al in olivine-spinel thermometer, clinopyroxene-liquid barometer) that utilize chemical zonation in individual crystals. These methods reveal the basaltic mush resides at shallow crustal levels and relatively cooler temperatures compared to typical basalts (~100-350 MPa, ~920-970°C). Diffusion chronometry,

which takes advantage of the chemical gradients in crystals, is used to determine timescales of magma residence (~10^4 yr), cooling paths (~10^3 yr), and the final stages of differentiation prior to eruption (~months to years) at Cordón Caulle. This study reports first-ever parameters on the underlying crystal mush that generated explosive silicic eruptions but can also be used as a model to interpret crystal mush systems globally and better understand the dynamics of rhyolite formation in continental arcs.

Acknowledgments

I had a non-traditional path into geology that has been filled with many challenges and obstacles but has also been filled with many opportunities for growth as a scientist as well as a person. I am very fortunate for a large and ever-growing support system and cannot emphasize enough how appreciative I am of that support along the way.

My advisor, Dr. Philipp Ruprecht, played a major role in my development as a scientist through both my master's and PhD research. Philipp consistently challenged me while simultaneously providing guidance and advice. I had the freedom to explore many avenues of interest in my research which was critical to finding my place in the volcanology field. I would not be where I am today without his constant support, commitment to conducting influential science, and dedication toward seeing his students succeed. I have significantly improved as a scientist since starting my master's in 2016, and I hope I continue to apply all that I have learned from Philipp into my future endeavors.

I would also like to thank my committee members Drs. Stacia Gordon, Carolina Muñoz-Saez, Wenrong Cao, Kent Ervin, and Bridget Ayling for their genuine interest in my research and dedication to helping me improve as a scientist. I have appreciated the feedback, coursework, conversations, field excursions, and mentorship over the years. In addition to my committee members, I am extremely grateful to Joel DesOrmeau who has taught me the ins and outs of using several analytical instruments. While I learned how to operate the SEM-EDS, the laser, and the microprobe, Joel also became a friend and support system. Our interactions were filled with venting sessions, life advice, and sarcastic retorts. He also managed to accommodate my frequent last-minute requests to collect more data, and I cannot thank him enough.

During my PhD, I was fortunate to be a part of an interdisciplinary group of scientists all working on Cordón Caulle. I learned so much from my collaborators and co-authors including Helge Gonnermann, Patrick Phelps, Carolina Muñoz-Saez, Matt Pritchard, Francisco Delgado, Diego Lobos, Josh Weijaczka, and Alvaro Amigo. Over the years, we have had countless zoom meetings, conference meetups, and field campaigns all to discuss our science and provide feedback for each other, and I greatly appreciate it.

My time at UNR would not be the same without the support of my peers in the Department of Geological Sciences and Engineering. Thank you to all of my fellow students along the way who created a fun and supportive community including Ellyn Huggins, Drew Levy, Erika Groh, Justin Toller, Kurt Kraal, Alex Holmwood, Neal Mankins, Pooja Sheevam, Mike Say, Iza Ogilvie, Wes Johns, Sophie Rothman, Luz Lim, Dominik Vlaha, Alex Hoinville, Shasta Longo, Emily Dektar, and many others. I will always cherish the memories of playing spike ball at Lake Tahoe, beers in the park, department events, football games, hot air balloon weekends, and camping trips. I would like to specifically thank Ellyn Huggins for being the most amazing office mate and friend over the years. She has listened to countless practice talks, helped problem solve issues with datasets, and always provides encouragement when I need it most. We've experienced conferences together, a ~2-month research expedition to the South Atlantic Ocean, the ups and downs of grad school, both getting very cute pups, and so much more. Thank you for everything!

My journey into science and igneous petrology was heavily influenced by the professors and mentors I had prior to graduate school including, Melissa Hage, Katja Meyer, Lily Claiborne, Nick Lange, Calvin Miller, and Anthony Koppers. They provided invaluable guidance and support, research opportunities, jobs where I acquired new skill sets, and so much more.

To my family and friends back home, I cannot thank you enough for the unwavering support and encouragement as I pursued a career in geology. It means the world to me that you all were there for my graduation in addition to the many years leading up to that moment. Mom, thank you for always asking questions about my research and taking the time to discuss it. I can't tell you how much it meant to me. Yvonne, thank you for being the best roommate and friend even through undergrad. You have heard me constantly talk about crystal mushes, olivine, volcanoes, and everything else under the sun. You have been there for so many changes and big moments in my life, and you helped me get through it all with relentless positivity and support.

To Scott Feehan:

I am beyond grateful to have you in my life, and I could not have done this without you. You have been my partner, my confidant, and my biggest fan for the past seven years. You inspire me daily with your work ethic, dedication, and creativity in your own dissertation. I am so proud of what you've accomplished in and out of your PhD. You have been there through all of the late nights, the accomplishments, and everything in between. You always make me laugh when I am at my most stressed, and I cannot thank you enough for believing in me every step of the way. I am so excited we get to close this chapter together and can't wait to take the next steps in our career together as well. You mean the world to me.

Table of Contents

List of Tables

List of Figures

Chapter 1

Introduction

Crystal mushes are an increasingly accepted conceptual model for how we envision the structure and makeup of magma chambers (Cashman et al., 2017; Holness et al., 2018; Lissenberg et al., 2018). Crystal mushes are made up of a crystal-dominated framework (~45-65 vol% crystallinity) with evolved interstitial liquid that can be extracted to form an eruptible crystal-poor melt lens (Hildreth, 2004). Previously, melt-dominated reservoirs were the traditional interpretation; however, this model came with challenges specifically about how to thermally sustain such large liquid bodies in the shallow crust, but also geophysical imaging has been unable to identify liquid-dominated reservoirs in many of these environments (Sinton & Detrick, 1992; Holness et al., 2018; Lissenberg et al., 2018). The frontier of this research and evolution of the crystal mush paradigm originated in mid-ocean ridge environments due to their volcanically active nature and the accessibility of plutonic and volcanic sections that can be paired with geophysical surveys to better constrain findings (Sinton & Detrick, 1992; Lissenberg et al., 2018). The crystal mush paradigm has become a widespread interpretation for many volcanic environments such as the Kameni Islands in Santorini, super-eruption systems like that of Long Valley Caldera, CA, or Fish Canyon Tuff in the San Juan Volcanic Field, and has been applied to stratovolcanoes in continental arcs (i.e., Mount St. Helens, Mount Unzen) (Nakamura, 1995; Bachmann & Bergantz, 2003; Hildreth, 2004; Holness et al., 2018; Wanke et al., 2019).

Most petrologic studies either focus on intrusive plutons from old volcanic environments or on erupted crystal-poor products such as rhyolitic ignimbrites or lava flows. While both aspects present valuable information, the perspective is from one part of the crystal mush

structure. Silicic ignimbrites or lava flows represent the crystal-poor melt lens and intrusive plutons preserve more insight toward the crystal-rich mush. Many times, either of these options are studied from eruptions that pre-date humans or are from eruptions that do not have geophysical monitoring. This study presents a unique opportunity to alleviate these challenges and investigates crystal mush constraints from the active volcanic complex, Puyehue-Cordón Caulle, Chile (PCC). PCC contains both aspects of the crystal mush structure with crystal-rich mafic enclaves hosted in crystal-poor rhyolite and has had three major eruptions in the last century (Singer et al., 2008; Delgado, 2021). This research reveals interpretations that the mafic enclaves represent fragments of the underlying crystal-rich mush while the rhyolite is the eruptible crystal-poor melt lens cap. PCC is a well-monitored volcanic complex and surface deformation was recorded pre-, syn-, and post- the 2011-12 eruption via geophysical monitoring (Delgado et al., 2016). The geophysical data continues to show episodic inflation into 2020 (Delgado, 2021). Here, we take advantage of the high crystallinity nature of the mafic enclaves to determine the pre-eruptive storage conditions, thermal history, and timescales of ongoing magmatic processes of an active crystal mush using a variety of mineral-scale techniques. This dissertation will contribute toward a better understanding of silicic magma generation at crystal mush systems globally, as well as provide petrologic constraints that can be paired with deformation data to improve interpretations of pre-eruptive signals at active volcanic centers.

Chapter Summaries

In Chapter 2, I utilize textural observations from rock samples and thin sections, bulk rock chemistry, and mineral chemistry to provide the first petrologic constraints on a crystal mush system at Cordón Caulle, Chile. Analyses are conducted on crystal rich mafic enclaves hosted within crystal poor rhyolite lava from the 2011-12 eruption. Two types of enclaves are

identified and their origin and impact on the system are discussed in detail based on textural and geochemical evidence. This study highlights methods for efficient melt-crystal separation in shallow mush systems that generates one of the largest compositional gaps on record between the mafic enclaves and their rhyolite host lava at 17 wt% SiO_2. Compositional gaps provide important insight toward how oceanic and continental crusts differentiate but are less common in continental arcs such as the Andes (Dufek & Bachmann, 2010). As a result, this chapter highlights the efficiency and impact of crystal fractionation in continental crust. Geochemical data from the enclaves and rhyolite host provide evidence for a genetic relationship between the two lithologies. Major and trace element data suggest the rhyolite was formed directly from the basaltic mush through efficient fractionation, and as a result, short circuits the full range in magmatic differentiation in a single step. These findings highlight the importance of understanding the processes that lead to rhyolite formation.

Chapter 3 provides quantitative constraints on magma storage parameters for the crystal mush and investigates the thermal history and evolution of the system. This chapter utilizes a variety of thermobarometers and geospeedometry that take advantage of the highly crystalline nature of the enclaves (Faak et al., 2013;2014; Coogan et al., 2014; Neave & Putirka, 2017). The main focus of this chapter is using a thermometer that utilizes the temperature-dependent partitioning of Mg between plagioclase and clinopyroxene. This thermometer was developed using plutonic samples; however, I apply it to crystal-rich volcanic samples. This thermometer has great potential to be used many magmatic systems because plagioclase-clinopyroxene pairs are a common mineral assemblage across both plutonic and volcanic environments. They are also present across a range in compositions from mafic to intermediate magmas. This method proves to be a valuable and widely applicable tool if properly constrained. Results of this study

are consistent with the conceptual model of a shallow crystal mush connected to the overlying rhyolite posed in Chapter 2 and presents new insights toward the thermal history of the enclaves and the timescales associated with their incorporation into the rhyolite.

Chapter 4 investigates the origin of chemical zonation in olivine to better constrain timescales of magmatic processes calculated from diffusion chronometry. Robust timescale estimates are used to determine the temporal evolution of the mush and timescales associated with mush assembly in the crust. I analyze stable isotopes (Fe and Mg) to discern between crystal growth or diffusion-driven chemical zonation and then use numerical modeling to assess the timescales associated with the diffusive processes (Oeser et al., 2015). These techniques have yet to be conducted on mafic enclaves. Isotopic profiles reveal two distinct phases of diffusion, within the core and the core-rim boundary, that distill first ever estimates for the longevity of the crystal mush and reveal timescales associated with late-stage differentiation and diffusion. This chapter highlights that even in a quasi-closed and simplistic magmatic system, growth signatures are still difficult to preserve and diffusion overprints growth conditions.

Chapter 5 is a conclusion of all chapters that summarizes the determined petrologic constraints and how they contribute to a conceptual model. Additionally, it summarizes the three different timescale estimates that inform varying processes and provide a temporal evolution of the crystal mush. Overall, this work highlights the unique opportunity of using crystal-rich enclaves to inform pre-eruptive magmatic conditions and addresses the nuanced interpretations of enclave sourcing.

References

Bachmann, O., & Bergantz, G. W. (2003). Rejuvenation of the Fish Canyon magma body: A window into the evolution of large-volume silicic magma systems. *Geology*, *31*(9), 789–792. https://doi.org/10.1130/G19764.1

Cashman, K. V., Sparks, R. S. J., & Blundy, J. D. (2017). Vertically extensive and unstable magmatic systems: A unified view of igneous processes. *Science*, *355*(6331), eaag3055. https://doi.org/10.1126/science.aag3055

Coogan, L. A., Saunders, A. D., & Wilson, R. N. (2014). Aluminum-in-olivine thermometry of primitive basalts: Evidence of an anomalously hot mantle source for large igneous provinces. *Chemical Geology*, *368*, 1–10. https://doi.org/10.1016/j.chemgeo.2014.01.004

Delgado, F. (2021). Rhyolitic volcano dynamics in the Southern Andes: Contributions from 17 years of InSAR observations at Cordón Caulle volcano from 2003 to 2020. *Journal of South American Earth Sciences*, *106*, 102841. https://doi.org/10.1016/j.jsames.2020.102841

Delgado, F., Pritchard, M. E., Basualto, D., Lazo, J., Córdova, L., & Lara, L. E. (2016). Rapid reinflation following the 2011–2012 rhyodacite eruption at Cordón Caulle volcano (Southern Andes) imaged by InSAR: Evidence for magma reservoir refill. *Geophysical Research Letters*, *43*(18), 9552–9562. https://doi.org/10.1002/2016GL070066

Dufek, J., & Bachmann, O. (2010). Quantum magmatism: Magmatic compositional gaps generated by melt-crystal dynamics. *Geology*, *38*(8), 687–690. https://doi.org/10.1130/G30831.1

Faak, K., Chakraborty, S., & Coogan, L. A. (2013). Mg in plagioclase: Experimental calibration of a new geothermometer and diffusion coefficients. *Geochimica et Cosmochimica Acta*, *123*, 195–217. https://doi.org/10.1016/j.gca.2013.05.009

Faak, K., Coogan, L. A., & Chakraborty, S. (2014). A new Mg-in-plagioclase geospeedometer for the determination of cooling rates of mafic rocks. *Geochimica et Cosmochimica Acta*, *140*, 691–707. https://doi.org/10.1016/j.gca.2014.06.005

Hildreth, W. (2004). Volcanological perspectives on Long Valley, Mammoth Mountain, and Mono Craters: Several contiguous but discrete systems. *Journal of Volcanology and Geothermal Research*, *136*(3), 169–198. https://doi.org/10.1016/j.jvolgeores.2004.05.019

Holness, M. B., Stock, M. J., & Geist, D. (2019). Magma chambers versus mush zones: Constraining the architecture of sub-volcanic plumbing systems from microstructural analysis of crystalline enclaves. *Philosophical Transactions of the Royal Society A: Mathematical, Physical and Engineering Sciences*, *377*(2139), 20180006. https://doi.org/10.1098/rsta.2018.0006

Lissenberg, C. J., MacLeod, C. J., & Bennett, E. N. (2019). Consequences of a crystal mush-dominated magma plumbing system: A mid-ocean ridge perspective. *Philosophical Transactions of the Royal Society A: Mathematical, Physical and Engineering Sciences*, *377*(2139), 20180014. https://doi.org/10.1098/rsta.2018.0014

Nakamura, M. (1995). Continuous mixing of crystal mush and replenished magma in the ongoing Unzen eruption. *Geology*, *23*(9), 807–810. https://doi.org/10.1130/0091-7613(1995)023<0807:CMOCMA>2.3.CO;2

Neave, D. A., & Putirka, K. D. (2017). A new clinopyroxene-liquid barometer, and implications for magma storage pressures under Icelandic rift zones. *American Mineralogist*, *102*(4), 777–794. https://doi.org/10.2138/am-2017-5968

Oeser, M., Dohmen, R., Horn, I., Schuth, S., & Weyer, S. (2015). Processes and time scales of magmatic evolution as revealed by Fe–Mg chemical and isotopic zoning in natural olivines. *Geochimica et Cosmochimica Acta*, *154*, 130–150. https://doi.org/10.1016/j.gca.2015.01.025

Sinton, J. M., & Detrick, R. S. (1992). Mid-ocean ridge magma chambers. *Journal of Geophysical Research: Solid Earth*, *97*(B1), 197–216. https://doi.org/10.1029/91JB02508

Wanke, M., Karakas, O., & Bachmann, O. (2019). The genesis of arc dacites: The case of Mount St. Helens, WA. *Contributions to Mineralogy and Petrology*, *174*(1), 7. https://doi.org/10.1007/s00410-018-1542-6

Chapter 2

Insights for crystal mush storage utilizing mafic enclaves from the 2011-12 Cordón Caulle eruption

Heather Winslow*[1], Philipp Ruprecht[1], Helge M. Gonnermann[2], Patrick R. Phelps[2], Carolina Muñoz-Saez[1], Francisco Delgado[3], Matthew Pritchard[4], Alvaro Amigo[5]

[1]University of Nevada, Reno, [2]Rice University; [3]University of Chile; [4]Cornell University; [5]Servicio Nacional de Geología y Minería (SERNAGEOMIN)

This chapter has already been published and is included as part of this dissertation.

Winslow, H., Ruprecht, P., Gonnermann, H. M., Phelps, P. R., Muñoz-Saez, C., Delgado, F., Pritchard, M., & Amigo, A. (2022). Insights for crystal mush storage utilizing mafic enclaves from the 2011–12 Cordón Caulle eruption. Scientific Reports, 12(1), 9734. https://doi.org/10.1038/s41598-022-13305-y

ABSTRACT

Two distinct types of rare crystal-rich mafic enclaves have been identified in the rhyolite lava flow from the 2011-12 Cordón Caulle eruption (Southern Andean Volcanic Zone, SVZ). The majority of mafic enclaves are coarsely crystalline with interlocking olivine-clinopyroxene-plagioclase textures and irregular shaped vesicles filling the crystal framework. These enclaves are interpreted as pieces of crystal-rich magma mush underlying a crystal-poor rhyolitic magma body that has fed recent silicic eruptions at Cordón Caulle. A second type of porphyritic enclaves, with restricted mineral chemistry and spherical vesicles, represents small-volume injections into the rhyolite magma. Both types of enclaves are basaltic end-members (up to 9.3 wt% MgO and 50-53 wt% SiO_2) in comparison to enclaves erupted globally. The Cordón Caulle enclaves also have one of the largest compositional gaps on record between the basaltic enclaves and the rhyolite host at 17 wt% SiO_2. Interstitial melt in the coarsely-crystalline enclaves is compositionally identical to their rhyolitic host, suggesting that the crystal-poor rhyolite magma was derived directly from the underlying basaltic magma mush through efficient melt extraction. We suggest the 2011-12 rhyolitic eruption was generated from a primitive basaltic crystal-rich mush that short-circuited the typical full range of magmatic differentiation in a single step.

INTRODUCTION

We have identified crystal-rich basaltic enclaves hosted in the rhyolite lava from the 2011-12 Cordón Caulle eruption located in the SVZ of Chile (Fig. 2.1). Here we report on the mafic enclave's occurrence, their textural and geochemical characteristics, and we develop a conceptual model for their formation. Mafic enclaves are inclusions of chemically distinct, and typically crystal-rich, magma within a host magma that tends to be compositionally more evolved than the inclusion[1]. Mafic enclaves can form by a spectrum of processes that result in a

more or less direct genetic and spatial link between the enclave-forming mafic magma and the more evolved host magma. Mafic enclaves are most commonly associated with magma recharge into an already established or unrelated magmatic system[1,2,3,4]. In contrast, based on textural and geochemical characteristics, the 2011-12 Cordón Caulle enclaves likely represent pieces of a crystal-rich magma mush that were incorporated into the crystal-poor rhyolite magma erupted at Cordón Caulle. In the case of a crystal mush origin, the mafic enclaves may also provide direct insight toward silicic magma production.

Crystal mushes are defined as large, crystal-dominated (~45-65%) storage reservoirs that contain evolved interstitial melt[5-7]. Previous studies have highlighted that crystal-rich magma mush storage reservoirs can produce voluminous and explosive eruptions of silicic magma, sometimes up to >5000 km^3 such as that of Fish Canyon Tuff[5-8]. They are associated with large caldera-forming eruptions, such as the Bishop Tuff at Long Valley Caldera, as well as volumetrically smaller systems such as Mount St. Helens and Mt. Mazama[3,6,9]. A crystal mush is more mafic in bulk composition than the evolved interstitial melt, and if the interstitial melt is extracted, it can form an overlying crystal-poor silicic melt lens cap[5,6,10,11]. Fractional crystallization is considered to be the dominant process to generate such crystal-poor silicic magma in crystal mushes[12,13]. This is likely associated with the high crystallinity of crystal mushes that allows for increased residual melt evolution[6,12,13]. While most crystal-rich magma mushes are intermediate in composition, thus making a step-wise change from intermediate to felsic magmas when producing the melt lens cap[5-7], Cordón Caulle may contain a basaltic mush based on the basaltic mafic enclaves. This means Cordón Caulle may experience highly efficient fractional crystallization to produce rhyolite directly from basalt. Additionally, if the mafic enclaves are representative of a crystal mush, they represent evidence of an active crystal mush

and will provide new opportunities to study mush dynamics at an active volcanic system. Whether a crystal mush architecture can efficiently generate large volumes of eruptible silicic magma directly from a basaltic crystal-rich mush has not yet been demonstrated in volcanic arcs. This study highlights how mafic enclaves can reveal processes in active magmatic systems other than mafic recharge. Here we argue that the Cordón Caulle mafic enclaves are evidence for an underlying crystal mush as opposed to representing magma recharge, and that the enclaves may constrain the efficiency and limits to fractional crystallization and rhyolite formation as well as provide global insight for crystal mush dynamics in volcanic arcs.

BACKGROUND

Cordón Caulle is a fissure system amidst a NW-elongated graben that is part of the larger Puyehue-Cordón Caulle volcanic complex (PCC; 40.31°S, 72.10°W), which is located in the Chilean SVZ[14,15]. PCC is a laterally extensive volcanic complex comprised of the stratocone Puyehue, the 15 km-long Cordón Caulle fissure system, and the Cordillera Nevada Caldera, a collapsed shield volcano[16]. Cordón Caulle has been the site of three eruptions during the last 100 years (1921-22, 1960, 2011-12)[14,15,17-19]. Multiple eruptive vents for the 1921-22 and 1960 eruptions are distributed along faults, while the 2011-12 eruption was restricted to a singular eruptive vent. All three eruptions produced dacitic to rhyolitic lava flows of approximately 1 km^3 and distributed ash regionally[15,17-19]. Published geothermobarometry data suggests that shallow magma storage is associated with all three of the historic eruptions (50-100 MPa and 870–920 °C[17]; 5-7 km, 100-140 MPa, and 895°C[18]; 3-7 km[20].

Satellite- and ground-based monitoring have provided exceptional pre-, syn-, and post-eruptive deformation across the entire Cordón Caulle graben for the 2011-12 eruption[21-23]. Inflation of approximately 0.5 m preceded the eruption for several years, subsidence of

approximately 4.5 m was recorded during the eruption, and rapid re-inflation of approximately 1 m followed the eruption, which represents one of the largest uplift rates for silicic systems with ~ 0.45 cm/yr immediately after the eruption[21,22,24]. Additional localized inflation beneath the 2011-12 vent has been interpreted as rapid laccolith emplacement shortly after the onset of the eruption (Fig. 2.1)[23]. The laccolith is located ~ 20-250 m below the surface and the overlying volcanic deposits have extensive cracks and fumarolic activity in the vicinity of the vent area[23]. In recent years, inflation has been episodic and because the ground deformation extends over the entire Cordón Caulle graben, it suggests a spatially connected and laterally extensive magmatic body that accommodates magma redistribution, either in response to recharge or post-eruptive poro-elastic effects within a mush stored in the shallow crust[21,22,24]. A crystal-mush model has been proposed in previous studies due to the spatially distributed eruptive vents and deformation signals, but here we present direct evidence for a crystal-rich magma mush through petrologic and geochemical analysis of mafic enclaves[15,17-19].

RESULTS

Enclave Petrography

Two types of mafic enclaves are present in the 2011-12 rhyolite flow. The majority of enclaves are relatively coarsely-crystalline dominated by phenocrysts (~55-70 vol%) (Fig. 2.2), while a subordinate group of enclaves (2 of 33 samples) are distinctly porphyritic with <35 vol% phenocrysts (Fig. 2.3; Table 2.1; ESM 2.2). Both types are vesiculated, yet the coarsely-crystalline enclaves contain a slightly greater abundance of vesicles (>15 vol%) compared to the porphyritic enclaves (<15 vol%) (Fig. 2.3, Table 2.1). While technically the dominant enclave population is fine- to medium-grained, we will refer to them as “coarsely-crystalline” as a relative comparison to the porphyritic population. Mafic enclaves range in size from ~ 5-20 cm

in diameter, but occasionally reach up to ~ 40 cm (Fig. 2.2a, b). Mafic enclaves are sub-rounded to sub-angular and are commonly found in devitrified rhyolite. We observe occasional pressure shadows surrounding the enclaves that suggests they were mostly solid during the lava emplacement[25-27].

Coarsely-crystalline Enclaves

The coarsely-crystalline enclaves are characterized by interlocking textures with average phenocryst sizes ranging from 300-600 μm but frequently reach >1000 μm (Fig. 2.2, 2.3). Phenocryst phases are listed in order of abundance: plagioclase (~40-45 vol%), clinopyroxene and olivine (~5-15 vol% with varying proportions), and Fe-Ti oxides (~ <1 vol%) with accessory apatite (Table 2.1). Plagioclase microlites dominate the groundmass (~10 vol%), and small amounts of melt pockets, now solidified glass, (~1-5 vol%) are present at the edges of phenocryst phases (Fig. 2.3a, d; Table 2.1; ESM 2.3, 2.4). The pervasive intergrowth and poikilitic textures between plagioclase, olivine, and clinopyroxene suggest coeval growth (Fig. 2.2, 2.3). Microlitic plagioclase also experiences impingement and intergrowth into phenocryst phases. The varying degrees of interlocking phases between microlites, microphenocrysts, and large phenocrysts (Fig. 2.2, 2.3; ESM 2.3, 2.4) may indicate bursts of nucleation at varying nucleation and growth rates[28]. Phenocrysts and microlites do not present lineation or foliation fabrics and therefore do not exhibit settling or compaction features. Low aspect ratios of phenocrysts (i.e. equant crystal shapes) is suggestive of slow cooling as opposed to rapid cooling typical for small dikes that may form more elongate crystal shapes due to greater undercooling[28,29]. While phenocrysts of plagioclase and clinopyroxene are subhedral and display planar surfaces on edges exposed to the groundmass, they are dominantly intergrown with other well faceted phenocrysts at random orientations (Fig. 2.3). Melt pockets surrounding

phenocrysts are irregular in shape and do not display parallel sides (Fig. 2.3; ESM 2.3, 2.4). Vesicles display irregular void-filling shapes amidst the crystal intergrowth (Fig. 2.3a, d). Generally, quench textures and chilled margins are absent in the coarsely-crystalline enclaves and crystal size and glassiness of the matrix do not vary systematically from interior to exterior. However, some groundmass heterogeneities near the enclave-host interface exist with distinct heterogenous strands of groundmass and small changes in microlite size and vesiculation in the rhyolite (ESM 2.5, e.g., PCC-18-15C). Enclave margins display a moving boundary with crystal clusters and glomerocrysts seemingly breaking off from the enclave into the rhyolite or being individually plucked into the rhyolite.

Plagioclase phenocrysts and microlites are normally zoned, the former sometimes exhibiting varying degrees of sieve textures within their cores (Fig. 2.2, 2.3; ESM 2.3). Plagioclase phenocrysts display stepwise zonation in anorthite (An) content. The calcic cores are homogeneous (~An_{80-90}) with only small normal and reverse internal zonation ($\Delta An < 5$), followed by a distinct step in An content (An_{55-65}, ~30 μm width). The outermost plagioclase has even lower An contents (<10 μm width) (ESM 2.3). We refer to these distinct zones as the core, mantle, and rim (Fig. 2.3a, d; ESM 2.3). Microlites exhibit both elongate and equant habit, and their zonation displays core-rim normal zonation without a significant mantle. Olivine phenocrysts have flat cores[30] with weak normal zonation limited to about the outermost 100 μm. Olivine in contact with other minerals can be unzoned. Anhedral olivine can be found as chadacrysts amidst plagioclase oikocrysts (ESM 2.3, 2.4). Clinopyroxene phenocrysts exhibit simple zonation with distinct compositional steps near their rims. In a few enclaves, clinopyroxene phenocrysts are the largest phenocryst phase with bimodal size distributions. As an example, PCC-18-15A contains populations of larger and smaller clinopyroxene with sizes of

>1000 μm and <500 μm, respectively (Fig. 2.3a), the latter being more frequent. Cores of larger clinopyroxene phenocrysts commonly contain plagioclase inclusions (ESM 2.3a, d). Olivine and clinopyroxene display frequent orthopyroxene reaction rims when in contact with the melt and not bounded by other phenocrysts (notated in ESM 2.4c, d, g, j, k). Peritectic orthopyroxene reaction rims are a late-stage process that are likely the result of interacting with the more evolved rhyolitic liquid[31]. Fe-Ti oxides exhibit frequent skeletal and dendritic growth.

Glomerocrysts occur throughout the rhyolite and near the enclave-rhyolite interface. Two populations of glomerocrysts have been identified. The first population resembles the same mineralogy, composition, and zonation patterns of the coarsely-crystalline enclaves. They are present at the enclave-host boundary. In this population, plagioclase has core-mantle-rim zones similar to plagioclase in coarsely-crystalline enclaves. These glomerocrysts seemingly represent broken off enclave fragments. The second glomerocryst population is not associated with the enclaves and only occurs in the rhyolite. It consists of plagioclase, clinopyroxene, olivine, and frequent Fe-Ti oxides as inclusions in clinopyroxene and olivine. These glomerocrysts have distinct composition and zonation patterns with plagioclase phenocrysts being uniformly evolved and minimally zoned in the interior. Rims have similar An contents to plagioclase rims in the enclaves (ESM 2.5). Fe-Ti oxides range from tens of microns up to ~150 μm and exhibit blocky habit (ESM 2.5). Additionally, exsolution lamellae can be identified in clinopyroxene glomerocrysts. The distinct textures of the second population of glomerocrysts suggest direct entrainment into the rhyolite independent of enclave formation.

Porphyritic Enclaves

The second less common enclave population displays porphyritic textures with a very distinct groundmass (Fig. 2.3g-i). Phenocrystic plagioclase (~30%) dominates the mineral

assemblage. Olivine (~2%), clinopyroxene (<1%), and oxides are subordinate (Table 2.1). The porphyritic enclaves have characteristic large spherical vesicles (Fig. 2.3g) as opposed to the coarsely-crystalline enclaves, whose vesicles are void filling and their irregular shapes are controlled by the crystal network. Plagioclase phenocrysts are dominantly large (>1000 μm) and display both elongate and equant crystal shapes with infrequent sieve textures. A subordinate plagioclase population has smaller crystal sizes (~250-500 μm). Regardless of size, plagioclase is commonly arranged in glomerocrysts. Plagioclase grain boundaries that are in contact with groundmass exhibit swallowtail textures (Fig. 2.3i; ESM 2.2e, f). Plagioclase core compositions are uniform with weak normal zonation at the outermost rim that is significantly less developed compared to coarsely-crystalline enclaves. Both size populations of plagioclase display similar compositional and zonation patterns. Olivine phenocrysts (~1000 μm) display both anhedral and skeletal crystal shapes (ESM 2.2c, d) with flat core compositions and orthopyroxene overgrowth[30]. Groundmass (~55%) consists of plagioclase microlites (70-100 μm) and interstitial mafic phases.

Geochemistry

Whole-rock data

The 2011-12 mafic enclaves from Cordón Caulle represent the primitive end-member for the entire eruptive history at PCC and are among the most primitive magmas for the entire SVZ (Fig. 2.4)[15]. With their range from 50-53 wt% SiO_2, 5.29-9.3 wt% MgO, $Mg\#_{\sim 53-66}$ (calculated on a molar basis with (Mg/(Mg+Fe)*100), 22-113 ppm Ni, and 94-248 ppm Cr (Fig. 2.4), the most primitive enclaves have major element compositions comparable to other primitive and near-primitive magmas globally[32]. Whole-rock trace element data displays typical subduction zone signatures for the mafic enclaves (Fig. 2.5a). Additionally, the enclaves lack a Eu anomaly

suggesting minimal plagioclase fractionation or accumulation (Fig. 2.5a). Subtle subgroupings of the enclaves can be identified based on major and trace element data but are not the focus of this study. To first order, Fe-enriched and Fe-depleted trends correlate with TiO_2, Al_2O_3, and CaO trends (Fig. 2.4, ESM 2.6). TiO_2 and Al_2O_3 display two distinct trends of enrichment and depletion, while CaO exhibits two clusters at ~12 wt% and ~10 wt% CaO (ESM 2.6).

The 2011-12 mafic enclaves are substantially more primitive in comparison to other well studied volcanic systems globally that have mafic enclaves with a range of enclave textures and eruptive environments. The 2011-12 mafic enclaves stand alone with uniquely elevated MgO, Mg#, Ni, and Cr contents (Fig. 2.4). Most other mafic enclaves are andesitic to dacitic. The closest analog to the 2011-12 enclaves are the most mafic enclaves from Medicine Lake, CA[33,34]. Both magmatic systems also share highly silicic host magmas (>70 wt% SiO_2) as well as an extensional tectonic environment. However, while Medicine Lake enclaves display a full range of enclave compositions from felsic to mafic, the 2011-12 mafic enclaves are exclusively mafic.

Mineral Compositions

Plagioclase

Core analyses for plagioclase phenocrysts in the coarsely crystalline enclaves are dominantly anorthitic ($An_{80-92.3}$), and only in rare cases do core compositions drop to ~An_{76} (ESM 2.1, 2.7). Plagioclase mantle compositions cluster around An_{55-65} but fully range from $An_{41.4-72.6}$. Detailed rim analyses were not performed, but the thin (<10 μm) rims have an approximate composition of An_{40-45}. Those rim compositions correlate with the plagioclase compositions in the rhyolite[17]. The porphyritic enclave population has plagioclase phenocrysts

with a more restricted calcic compositional range ($An_{85.8-92.5}$) and rims range from An_{39-41}. Microlite cores, excluding the porphyritic population, cluster from An_{80-88} with a full range from $An_{71.5-88.5}$. The more sodic rims cluster from An_{55-65} but have a full range from $An_{36.4-68.9}$. The microlite cores from the porphyritic population are more restricted with a compositional range from $An_{89.4-91.62}$ and rims from $An_{60.9-70.6}$.

Olivine and Clinopyroxene

Olivine core compositions from coarsely-crystalline enclaves range from $Fo_{\sim 70-85.7}$ with rims at $Fo_{\sim 58-63.9}$ (ESM 2.1, 2.7). Olivine from porphyritic enclaves is on average more magnesian ($Fo_{79.2-86.4}$) with extensive flat cores. We did not resolve core-rim compositional changes in the thin olivine rims. Clinopyroxene phenocrysts from the coarsely-crystalline and the porphyritic enclaves cluster at $Mg\#_{75-85}$ (full range $Mg\#_{55.6-83.6}$.) and $Mg\#_{64.5-69}$, respectively (ESM 2.1, 7).

DISCUSSION

Mafic Injection vs Crystal Mush

Mafic enclaves are commonly interpreted as products of mafic magma injection into a more silicic magma, but that is not the only explanation for their origin. Alternatively, mafic enclaves can represent fragments of cumulates or crystal mushes. In the case for magma injection origin, porphyritic textures and microstructural evidence supports formation in a dynamic liquid-rich environment[1,25,28]. The thermal contrasts between the injected magma and the silicic host magma result in large cooling rates and produce quench textures, especially along the enclave margins, associated with diffusion-limited crystal growth[28]. Alternatively, mafic enclaves that form from cumulates or crystal mushes will be dominated by interlocking textures

of larger grains growing under interface-controlled conditions during slow continuous cooling in a rigid crystal network[28,35].

Coarsely-crystalline Enclaves

Multiple lines of evidence support a crystal mush origin for the coarsely-crystalline enclaves. They are highly crystalline (55-70%), display interlocking cumulate grain textures, show dominantly simple mineral zonation patterns with a range in An and Fo content, contain angular void filling vesicles, and are chemically distinct compared to the global compilation of other mafic enclaves (Fig. 2.4; ESM 2.6). The large phenocryst sizes (300-600 μm), planar faces, and interlocking textures suggest prolonged and stable crystal growth that is possible in a mush environment[28,36,37]. Equant crystal shapes with planar faces, especially prevalent in plagioclase, are indicative of slow cooling rates (as opposed to elongate grains that result from rapid undercooling)[29]. However, a lack of grain orientations or textural lineation amongst any of the enclaves implies accumulation or compaction from crystal settling is not prevalent[28]. Liquid-rich magma chambers, especially low viscosity mafic magmas, are ideal environments for crystal settling and accumulation that produce undeformed, euhedral grains that are aligned in shape-preferred orientations[28]. The coarsely-crystalline enclaves, however, display randomly oriented and intergrown phenocrysts and microlites. Such textures are characteristic of crystal-rich environments like that of a crystal-rich mush[28]. Melt pockets are irregularly shaped around the edges of phenocrysts faces which suggests their shape is controlled by the highly crystalline network, and their lack of parallel sides further argues for the lack of influence from compaction. Additionally, angular-shaped void filling vesicles suggest that gas exsolution occurred in the presence of a rigid crystal mush framework and formed where space was available (Fig. 2.2, 2.3; ESM 2.3-5)[38,39]. Simple zonation patterns in phenocrysts, especially plagioclase, provide

evidence for storage in a thermally and compositionally buffered system that was not disturbed by recharge events of differing composition. Injection-sourced enclaves typically exhibit disequilibrium textures and chemical zoning representative of mixing and homogenization which we do not observe. Mafic recharge commonly produces a large thermal contrast between the injection and host magma resulting in oscillatory zoning and quench textures[25]. Minor evidence of reactive processes exists in the form of heterogeneous strands of groundmass within the rhyolite surrounding the enclave-rhyolite interface indicative of minimal interaction (ESM 2.5). The angularity of the coarsely-crystalline enclaves, pressure shadows in the host rhyolite, and lack of significant chilled margins preclude melt- or liquid-dominated incorporation mechanisms such as magma injection. Instead, these characteristics suggest that the enclaves were already largely crystallized with a more or less rigid crystalline matrix when they were entrained within the rhyolite.

Assuming the coarsely-crystalline enclaves represent a crystal mush, we propose their incorporation occurred during eruptive withdrawal of the overlying crystal-poor magma that entrained fragments of the underlying crystal mush (Fig. 2.6). If that was the case, the rigid nature of the crystalline matrix and the spatial proximity of the mush to the overlying rhyolite ensured that textures and compositions were only weakly overprinted during entrainment and transport. Thermal differences are likely small if the crystal-poor rhyolite directly overlies the mush. Given the rigid, crystal-rich mush, entrainment is likely inhibited, resulting in a relatively small abundance of entrained mush, and hence minimal abundance of enclaves within the erupting magma. The 1921-22 and 1960 eruptions produced nearly identical rhyolite lavas to the 2011-12 rhyolite, and thus all eruptions are suggested to be sourced from the same reservoir[17,18,22]. However, mafic enclaves are only identified in the 2011-12 eruption. We

envision these three eruptions are progressively tapping the rhyolitic melt lens cap without fully depleting the reservoir, and therefore, the most recent eruption (2011-12) is able to reach the interface between the rhyolite melt lens cap and the basaltic crystal mush (Fig. 2.6). We place the melt lens above the crystal-rich mush without significant overlying crystal-rich regions due to the absence of mafic enclaves in the prior two eruptions (1921-22, 1960). Eruption of the crystal-poor rhyolite from a melt lens within a crystal-rich mush should result in prevalent enclave incorporation within all three eruptions as erupting magmas would have to transit the mush.

To further corroborate the presence of a crystal mush, the coarsely-crystalline enclaves must show a genetic relationship to the rhyolite that overlies the mush. We attribute the formation of the rhyolite to fractional crystallization of the crystal-rich mush. Major elements such as MgO, FeO, Al_2O_3, K_2O, TiO_2, P_2O_5 support this notion with non-linear, fractionation trends between the enclaves, interstitial glass, and rhyolite compositions as opposed to linear mixing trends (Fig. 2.4; ESM 2.6). Incompatible trace elements within the rhyolite are uniformly elevated relative to the enclaves, consistent with in-situ fractionation, thus suggesting a genetic relationship between the enclaves and host rhyolite (Fig. 2.5a). Furthermore, incompatible trace elements of the enclave interstitial glass, collected via LA-ICP-MS, have similar compositions and compositional trends as the whole-rock rhyolite (Fig. 2.5a). Lastly, glass data from the interstitial melt of the enclaves and glass from the rhyolite have nearly identical compositions (Fig. 2.5b), aside from Ti and Mn. Variations in Ti are large for both enclave and rhyolite lithologies and are likely affected by small variations in oxide abundances. Reasons for the deviations in Mn are not known. The overlapping glass data between the enclaves and rhyolite suggest a genetic relationship between the two lithologies, where interstitial melt from the crystal-rich mush is extracted to form the overlying melt lens cap. Thus, we interpret the

rhyolitic interstitial melt of the mafic enclaves to represent the interstitial melt of a basaltic crystal mush that feeds a rhyolitic melt lens that was tapped in the 2011-12 eruption. We propose that at Cordón Caulle, rhyolite formation is short-circuited via highly efficient fractionation directly from a basaltic mush (Fig. 2.5, 2.6). This contrasts the typical, protracted differentiation paths that require smaller and progressive jumps in composition where rhyolite is produced from an intermediate crystal-rich mush[5,6,7]. This will be discussed in more detail in the "Compositional Gap" discussion section.

Porphyritic Enclaves

The low crystallinity, porphyritic texture, disequilibrium textures (swallowtails) on plagioclase, abundant microlites, and a narrow range in mineral chemistry of the 2011-12 porphyritic enclaves is consistent with an injection-sourced enclave model that is envisioned for numerous other enclave-bearing magmatic systems[1,4,25,33,34,40-47]. Similar to the porphyritic enclaves at Cordón Caulle, those systems have enclaves with crystallinities of ~10-30%, porphyritic textures, evidence of rapid cooling in the form of quenched or glassy margins, and a range in crystal sizes with abundant microlites near enclave margins. A major difference for Cordón Caulle enclaves, is their rare abundance (<1 vol%) compared to a much greater enclave abundance in other systems (>1-10 vol%)[1,3,25]. Thus, while these enclaves may be part of the eruption-triggering mechanism, e.g. tipping a system already in a near-critical state, they are unlikely to be the singular driver, especially as the dominant coarsely-crystalline enclaves are crystal mush related and not attributed to injection.

Instead, the porphyritic enclaves provide more information about magma assembly and the sub-surface architecture. The presence of isolated phenocryst clusters within the groundmass are indicative of varying crystal nucleation and growth rates. The swallowtail disequilibrium

textures on plagioclase phenocrysts that are bordered by groundmass suggest a change in crystal growth environment from interface-controlled slow growth to diffusion-limited rapid growth, likely due to increased undercooling (Fig. 2.3i, ESM 2.2e, f)[29,48]. Injection of a magma containing phenocryst clusters into a cooler host rhyolite led to rapid quenching and a shift in crystal growth dynamics, resulting in the observed swallowtail disequilibrium textures. Additionally, the large spherical vesicles (~700-1000 μm) that are unbound by phenocryst phases (Fig. 2.3g) suggest there was not a pre-existing crystal network and bubble growth was able to occur in a liquid-dominated system[38,39]. Groundmass crystallization appears to have been subsequent to bubble formation.

Although we link the porphyritic enclaves texturally to magma injection, the enclaves lack chemical evidence for mixing or hybridization during interaction with the crystal-rich magma mush or rhyolite lens. Such interactions are common in enclave-bearing systems[45,49] and predicted when recharge and mush compositions are similar[50]. Mixing leads to diverse crystal populations that are distinct in composition, size, and internal zonation[51,52]. In contrast, olivine and plagioclase compositions from the porphyritic enclaves are tightly bound (~Fo_{84} and ~$An_{85.8\text{-}92.5}$ (ESM 2.1, 2.7), when compared to phenocrysts in the coarsely-crystalline enclaves. This suggests that in rare occasions mafic injections bypass the mush chemically unobstructed and become entrained in the rhyolite upon eruption. Their low abundance suggests that such pathways are either rare or that the individual volume of mafic injections is small compared to the shallow crystal mush reservoir. We speculate that the crystal-rich mush beneath the rhyolite lens is spatially and thermally heterogeneous creating areas of higher and lower melt content, where inactive portions of the mush have a lower melt content and higher crystallinities that lead to a more rigid behavior amenable to fracturing. This would allow for some of the mafic

injections to travel through the mush without mixing or hybridization, producing the tightly bound primitive compositions in olivine within the porphyritic enclaves. Ultimately these injections reach the rhyolite chemically unobstructed, thus entraining primitive porphyritic enclaves in the eruption alongside the coarsely-crystalline enclaves (Fig. 2.6).

The Importance of Melt Extraction and Mush Heterogeneity

We defer to a crystal mush origin for the coarsely crystalline enclaves as opposed to cumulate origin due to their textures and chemistry. While crystal mush systems can foster accumulation signatures due to crystal settling and melt extraction[53,54], this would lead to preferred crystal orientations, foliation around large grains, frequent glomerocrysts, and minimal microlites typical for cumulates[28]. Moreover, those processes produce bulk chemistry changes in response to the preferential accumulation or removal of mineral phases such as olivine and plagioclase. This causes, for example, elevated MgO and Ni concentrations and Eu anomalies, respectively. The mafic enclaves in the 2011-12 eruption have neither typical cumulate textures nor do they show chemical evidence for accumulation of olivine or plagioclase (Fig. 2.5a). Instead, their composition lacks an Eu anomaly and they are more akin to primitive magmas (5-9 wt% MgO)[32]. Thus, we interpret the Cordón Caulle enclaves to be representative of a crystal mush that has not undergone large degrees of crystal settling nor preserves signatures of significant melt extraction. To produce large volumes of silicic magma by fractionation from a crystal mush without significantly altering the mush composition, requires a sufficiently large mush. In case of a several kilometer thick mush, the upper parts of the mush could be in a compositional steady state with silicic magma removal upward and replenishment of mafic magma from below retaining its basaltic nature and overprinting signatures of significant melt removal. Such a conceptual model would also imply that the mush is spatially contiguous with

the overlying rhyolite. The crystal mush could become progressively more cumulate-like with depth, but the coarsely-crystalline enclaves only represent the top layers of the crystal mush (Fig. 2.6).

While the coarsely-crystalline enclaves are considered a cohesive population, they do encompass a range of compositions in major and trace elements (MgO, Mg#, Ni, Cr, Al_2O_3, CaO), which is also reflected in their range in mineral chemistry. The dispersed range in olivine Fo content ($Fo_{\sim 70\text{-}85.7}$) and plagioclase An content ($An_{\sim 80\text{-}92}$) in the coarsely-crystalline enclaves indicate a composite nature of the enclaves that likely reflects subordinate compositional heterogeneity within the mush. We interpret that lower Fo olivines represent the long-lived mush, whereas the higher Fo olivines provide evidence for mafic additions that sustain the mush thermally and by mass. In other words, the mush may be episodically recharged by mafic injections that compositionally resemble the porphyritic enclaves. Mush heterogeneity is sustained through compositionally variable mafic recharge and evolve locally to small varying degrees depending on the injection history and thermal state (Fig. 2.6). We envision episodic mafic injections into the base of the mush that permeate the system or primitive melts that get injected into the mush at various depth levels. These injections keep the crystal mush basaltic, thermally buffered to prevent complete solidification, and sustain the overlying rhyolitic system at shallow levels[17,18,20].

Compositional Gaps

The 2011-12 Cordón Caulle eruption produced an extreme compositional gap, and thus may inform us about the full spectrum of differentiation processes common to compositional gaps[12,13]. A meaningful comparison of compositional gaps needs to be addressed at the level of individual eruptions, therefore, we compiled global data sets of mafic enclaves hosted in silicic

lavas from individual eruptions at a range of tectonic and volcanic settings (Fig. 2.7). The full range of compositional gaps in our compilation is <1 wt% SiO_2 up to18 wt% SiO_2, but rarely exceeding 16 wt% SiO_2. The 2011-12 eruption produced one of the largest compositional gaps at 17 wt% SiO_2. For stratocones and other arc systems the global range is restricted to <1-14 wt% SiO_2 making Cordón Caulle's gap an extreme end-member for on-arc magmatic systems. Moreover, the 2011-12 enclaves are the most mafic of all mafic end-members associated with compositional gaps, thus raising the question why mush dynamics (i.e. crystal-melt separation) are so effective in magma differentiation (evidenced through fractional crystallization from basalt to rhyolite) at Cordón Caulle compared to other systems with smaller compositional gaps and less mafic end-members[5-8,28,55-57].

Cordón Caulle demonstrates that crystal mush arc systems can produce rhyolite directly from basalt as the chemistry between rhyolite and the interstitial enclave glass are identical and fractionation trends characterize the overall major and trace element compositions of the 2011-12 eruption (Fig. 2.4, 5; ESM 2.6). Multiphase-fluid dynamic modeling suggests that crystal-melt separation becomes highly efficient at ~50-70% crystallinity in response to rheologic lock up which is observed at Cordón Caulle[13]. However, compaction, a commonly invoked mechanism[5], alone cannot produce the volume of melt via crystal-melt segregation observed at Cordón Caulle within the 40-year recurrence interval[17,18,22]. Based on the compaction equations (Eq. 5-9) from Bachmann & Bergantz 2004, we used a range of reasonable values for the height of mush layer (20-440 m), porosity (0.4), solid phase density (2844 kg/m^3), liquid phase density (2350 kg/m^3), dynamic melt viscosity (3.47x10^4 Pa·s), grain size (0.005 m radius), permeability (1.904x$10^{-8}$$m^2$), bulk and shear viscosity of the matrix (1x10^{-14}Pa˙s), and compaction length (1.13x10^{-13} m), and a crystal mush always requires a minimum of ~265 years to produce enough

melt for the 2011-12 eruption[5], not even addressing the need to produce rhyolite for three similarly sized eruptions in less than 100 years. Alternatively, the abundant presence of vesicles in the enclaves may point toward gas sparging as a mechanism to fractionate melt from the crystal framework[8,58]. Lastly, future poro-elastic modelling of ground deformation from the 2011-12 eruption could point toward magma reorganization implying pressure changes influenced melt separation from the crystal-rich mush[24]. Cordón Caulle provides an opportunity to further test whether an individual mechanism dominates melt extraction or whether a combination of mechanisms is needed to produce such large compositional gaps.

The compositional gap at Cordón Caulle most closely resembles the gap at Medicine Lake, CA, which has been explained by late-stage fractionation (57-61% solids removed) at shallow pressures (1-2 kbar) via a nearly flat cotectic during crystallization[33]. In their study, the solidus-liquidus line can flatten in a temperature-composition projection that allows for large amounts of crystallization to occur over a small temperature window resulting in a drastic compositional change in the residual liquid. Ultimately, Grove & Donnelly-Nolan (1986) [33] demonstrated that for calc-alkaline systems, increased crystallization may occur over a minimal temperature interval that allows for significant compositional gap formation. However, the Medicine Lake compositions involve amphibole that is absent in the 2011-12 enclaves, the latter being consistent with tholeiitic magmas typical for Puyehue-Cordón Caulle. Nonetheless, the interlocking textures of plagioclase, olivine, and clinopyroxene suggest coeval crystallization followed by late-stage orthopyroxene reaction rims in the coarsely-crystalline enclaves and may point towards similar processes effective at Medicine Lake explaining the formation of a such a large compositional gap. The primitive nature of microphenocrysts in the coarsely-crystalline enclaves suggests late-stage melt evolution and is consistent with late-stage fractionation to

produce the rhyolite melt during shallow storage (3-7 km depth)[17,18,20]. The 2011-12 Cordón Caulle eruption may represent an alternative to the common protracted model of silicic magma production along a transcrustal evolutionary path with continual differentiation as magmas migrate upward in the crust[7]. Instead, Cordón Caulle provides evidence for differentiation within the shallow crust that short-circuits multi-stage processing.

CONCLUSION

While the rhyolitic eruptions from Cordón Caulle have been studied in great detail, our study reports previously undescribed basaltic enclaves that provide a more complete picture of the magmatic system. We interpret the coarsely-crystalline mafic enclaves hosted in rhyolite lava as evidence for a compositionally zoned magmatic system comprised of a crystal-rich basaltic, but internally-heterogeneous, magma mush overlain by a crystal-poor rhyolite melt lens cap. The porphyritic enclaves are interpreted to represent open-system behavior that generates rare mafic magma injection directly into the rhyolitic melt lens cap. Enclave chemistry supports the notion that the crystal-poor rhyolite is genetically related to the mafic enclaves through highly efficient fractionation via melt extraction from the crystal-rich mush. The efficient extraction of interstitial melt from the mush has produced one of the largest compositional gaps globally at 17 wt% SiO_2, with near-primitive to primitive compositions directly producing rhyolite at shallow depths without any involvement of intermediate compositions. The implications of the mafic enclaves and their connection to the erupted rhyolite challenge the multi-stage, transcrustal evolutionary path for silicic magma generation that typically produces a range of compositions. Cordón Caulle's spatially dispersed eruptive vents and distributed ground deformation throughout the graben are consistent with our interpretation of a laterally extensive crystal mush storage reservoir, and our work on the mafic enclaves provides direct evidence for the presence

of a crystal mush at an active system. Additionally, our identification and analysis of the enclaves determined the direct source of the silicic magma generation for the 2011-12 eruption. In short, we provide geochemical and textural evidence that the erupted rhyolite was sourced from the interstitial melt of the basaltic crystal mush and was extracted to form an eruptible melt lens cap. Findings from these enclaves will also inform past and future interpretations of geophysical and geodetic observations at Cordón Caulle.

METHODS

Sampling and Enclave Characterization

A total of 33 mafic enclaves were collected along most of the periphery of the 2011-12 flow field as well as in the interior of the flow near the crater vent (Fig. 2.1). While rare (~ <1 vol%), the enclaves are almost ubiquitously dispersed, and in a few areas we find them in clusters of up to ~10 enclaves within a few meters of each other. A systematic assessment of their size, abundance, and distribution, and whether smaller enclaves (<1 cm) are more abundant, cannot be assessed due to the overall scarcity of enclaves. Brief reconnaissance work of the 1921-22 and 1960 lavas has not revealed enclaves in these earlier flows confirming previous work that did not report enclaves in these lavas.

Crystallinity, phase percentages, and vesicularity estimates are based on image analysis using JMicroVision. Randomized point-counting (n = 500) was conducted with uncertainties of ~5% based on counting statistics. Crystallinity estimates are based on phenocrysts which we define as crystals >100 μm. Microlites in the groundmass are defined as <100 μm. Additionally, this study refers to melt and groundmass where melt refers to crystal-free (including microlite-

free) liquid, while groundmass includes microlites. The terms melt and glass are used interchangeably.

Whole-rock and mineral chemistry

Bulk rock major and trace elements were determined for 19 mafic enclaves via x-ray fluorescence and inductively-coupled plasma mass spectrometry at the GeoAnalytical Lab at Washington State University following the analytical procedure of Johnson et al. (1999)[59] (ESM 2.1A). A duplicate bead was made to assess the analytical reproducibility. Major element data reports $R^2 = 1.0$ and trace element data reports $R^2 = 0.99$.

Major and trace element concentrations in plagioclase, olivine, clinopyroxene, oxides, and glass were determined on eight samples via a JEOL JXA-8200 electron microprobe equipped with five wavelength dispersive spectrometers and a silicon-drift energy dispersive spectrometer at Washington University in St. Louis. A mean atomic number background method was used[60]. Complete run conditions, elements analyzed, and reference materials are all reported in ESM 2.1B-G. 2-point core-rim analyses were performed on plagioclase, olivine, and clinopyroxene and single spot analysis were used for oxides and glass pockets. Plagioclase and glass measurements were performed with a defocused beam of 20 μm and Na was measured first to avoid Na loss.

Trace element concentrations of enclave interstitial melt were collected via laser ablation inductively coupled mass spectrometry (LA-ICP-MS) at the University of Nevada, Reno following the procedure of Woodhead et al. (2007)[61]. Data was reduced using Iolite software[62]. LA-ICP-MS was conducted on the coarsely-crystalline enclaves. A total of 38 singular points were collected at 33 μm diameter: 11 points in the enclave core interstitial melt, 10 points in the

enclave-host transition interstitial melt, 3 points in the enclave-host transition groundmass, and 14 points in rhyolite groundmass. Reference material, elements analyzed, uncertainty, and analytical conditions are reported in ESM 2.1H-I.

Acknowledgements

We would like to thank SERNAGEOMIN geologists Virginia Toloza and Nico Mendoza for their assistance in field work at Cordón Caulle. Great thanks go to Dr. Marian Holness for contributing detailed discussions about mafic enclave textures and interpretations. We also want to acknowledge Paul Carpenter (WUSTL) for electron microprobe assistance and advice.

Author Contributions

H.W. led research project, conducted field work and collected enclave samples, collected and compiled all data and analyses, prepared all figures, conducted and led all writing and editing stages; P.R. led research project, participated in field work, significantly contributed to conceptual model, dominantly involved in writing and editing stages; H. M. G. participated in fieldwork, contributed to the conceptual model, and was involved in all writing and editing stages; P.P. contributed to the conceptual model, participated in editing stages; C.M-S. participated in fieldwork, contributed to the conceptual model, participated in editing stages; F.D. contributed insight toward geodesy discussion and conceptual model, participated in editing stages; M.P. contributed to the conceptual model; A.A. contributed to the geologic context and aided in fieldwork.

Additional Information

Supplementary information accompanies this paper.

Competing Interest Statement: This research was funded by the National Science Foundation (NSF EAR 1823122) and the Nevada NASA Space Grant Graduate Research Opportunity Fellowship.

Table 2.1. Crystallinity of mineral phases, microlites, melt, and vesicles for both enclave populations. All values represent percentages (%).

	Coarsely Crystalline Enclaves					Porphyritic Enclaves	
Sample	**PCC-18-15A**	**PCC-18-15C**	**PCC-18-16-1**	**PCC-18-17A-1**	**PCC-18-17D-1**	**PCC-18-13B**	**PCC-16-03B**
Phenocryst Crystallinity	66	67	62	70	55	35	32
Plagioclase	*37*	*40*	*40*	*45*	*45*	*32*	*28*
Olivine	*13*	*16*	*6*	*9*	*6*	*2*	*4*
Clinopyroxene	*16*	*11*	*16*	*16*	*4*	*1*	*0*
Microlites	10	11	10	10	27	54	54
Melt	6	4	2	5	1	-	-
Vesicles	18	18	26	15	17	11	14
TOTAL	100	100	100	100	100	100	100

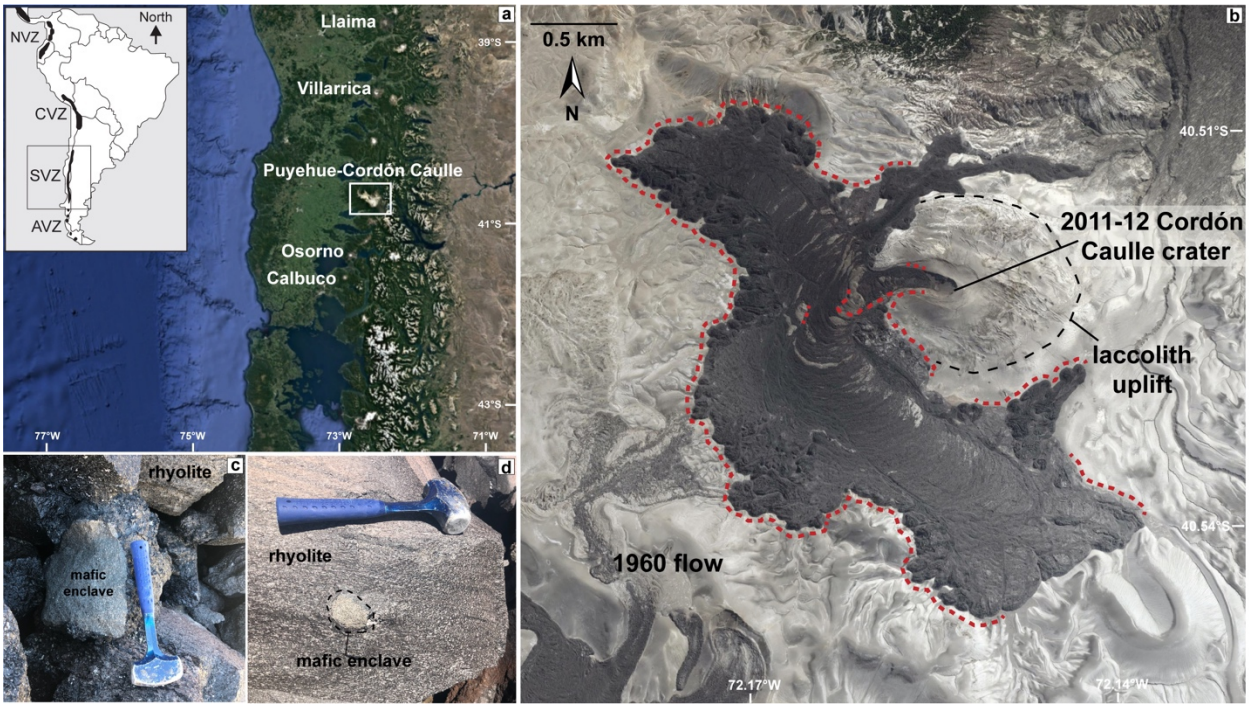

Figure 2.1. (a) Overview map of the SVZ of the Andes with inset of South America15. Overview map generated from Google Earth (Jan 2022; Image Landsat / Copernicus). White box identifies Puyehue-Cordón Caulle field area. (b) 2011-12 Cordón Caulle rhyolite lava flow. Image generated from Google Earth (Jan 2022; Image @ 2022 CNES / Airbus). Red dash: location of mafic enclave sampling for this study. Black dash: uplift area from laccolith23. (c-d) Field images of mafic enclaves hosted in rhyolite lava. Hammer for scale.

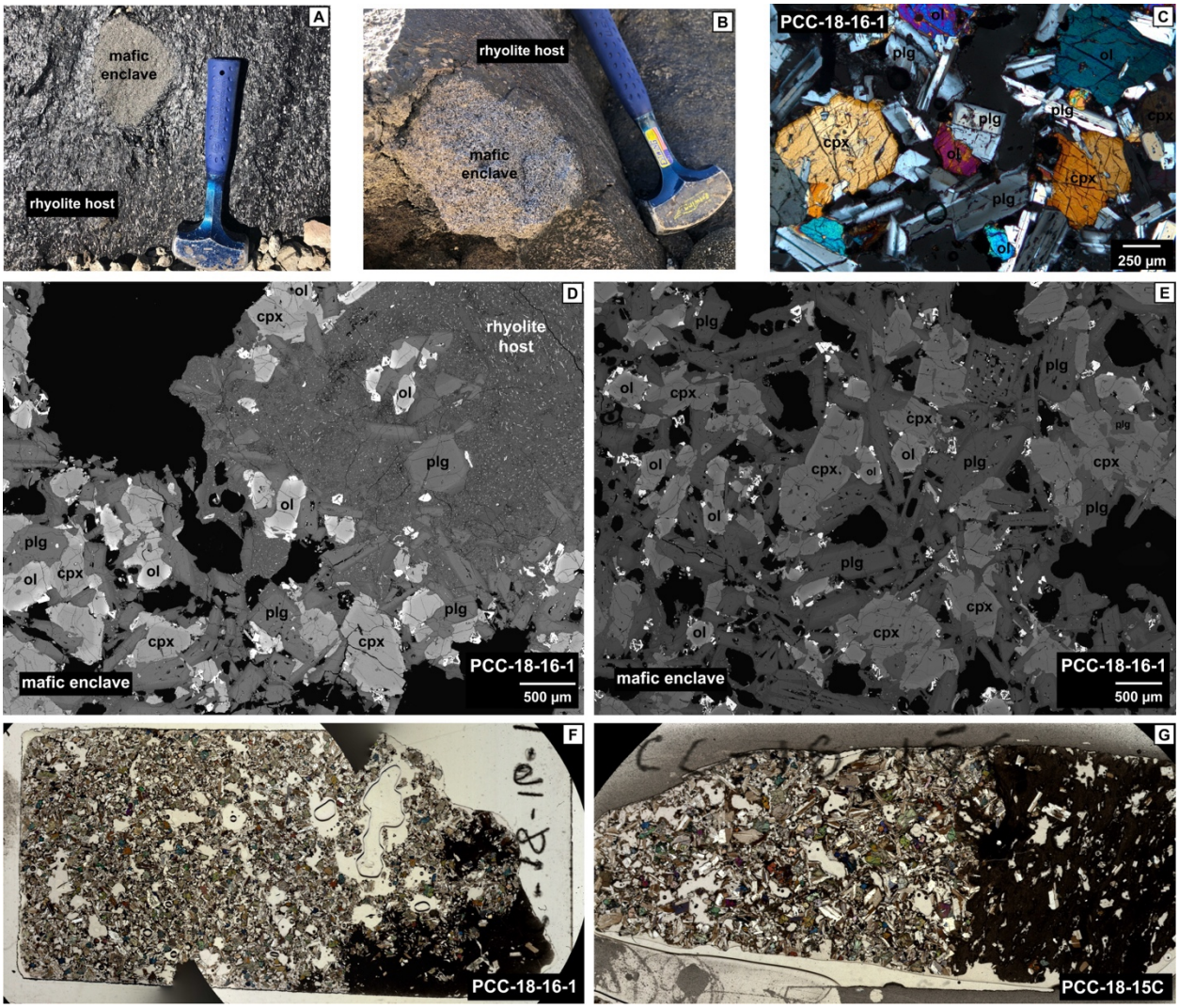

Figure 2.2. Textural images of the coarsely crystalline enclave population. (a-b) Field photos of mafic enclaves in rhyolite host with hammer for scale. (c) Micrograph highlighting enclave mineralogy, crystallinity, and interlocking grain texture. (d) Backscattered electron (BSE) map of mafic enclave-rhyolite host boundary. (e) BSE map of enclave core. (f-g) Thin section scans of coarsely crystalline enclaves highlighting crystallinity, mineralogy, and enclave-host boundary.

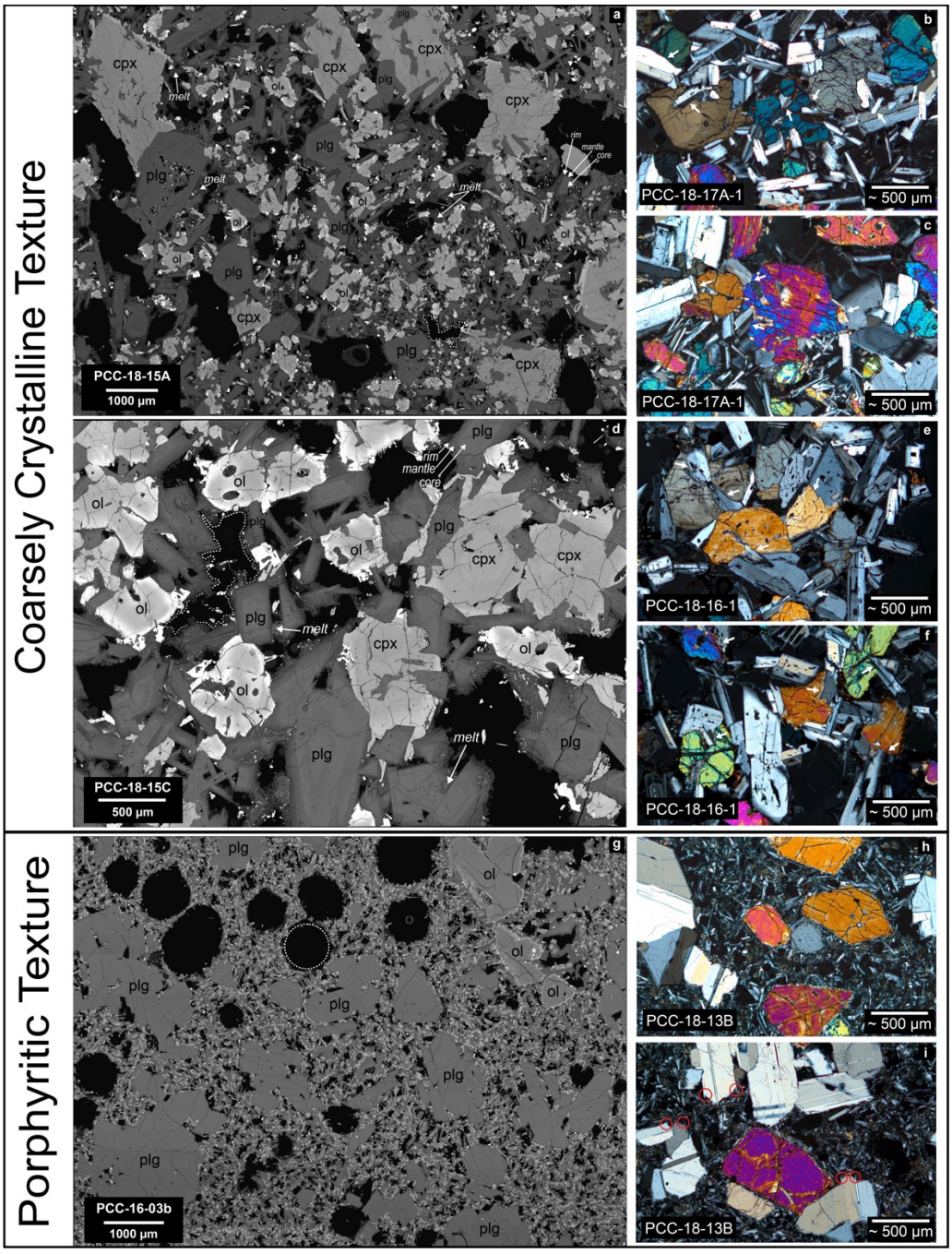

Figure 2.3. (a-i) Textural comparison of the coarsely crystalline and porphyritic enclave populations using BSE maps and micrographs. Images highlight variations in crystallinity and vesicle shape differences with spherical vesicles in porphyritic enclaves and angular void-filling vesicles in the coarsely crystalline population. Dotted white lines: highlight vesicle shapes in both enclave populations (a, d, g). (b, c, e, f) Micrographs display interlocking grain textures that are highlighted by white arrows. (i) Micrograph of porphyritic enclave with plagioclase clusters. Red circles highlight swallowtail disequilibrium textures of plagioclase.

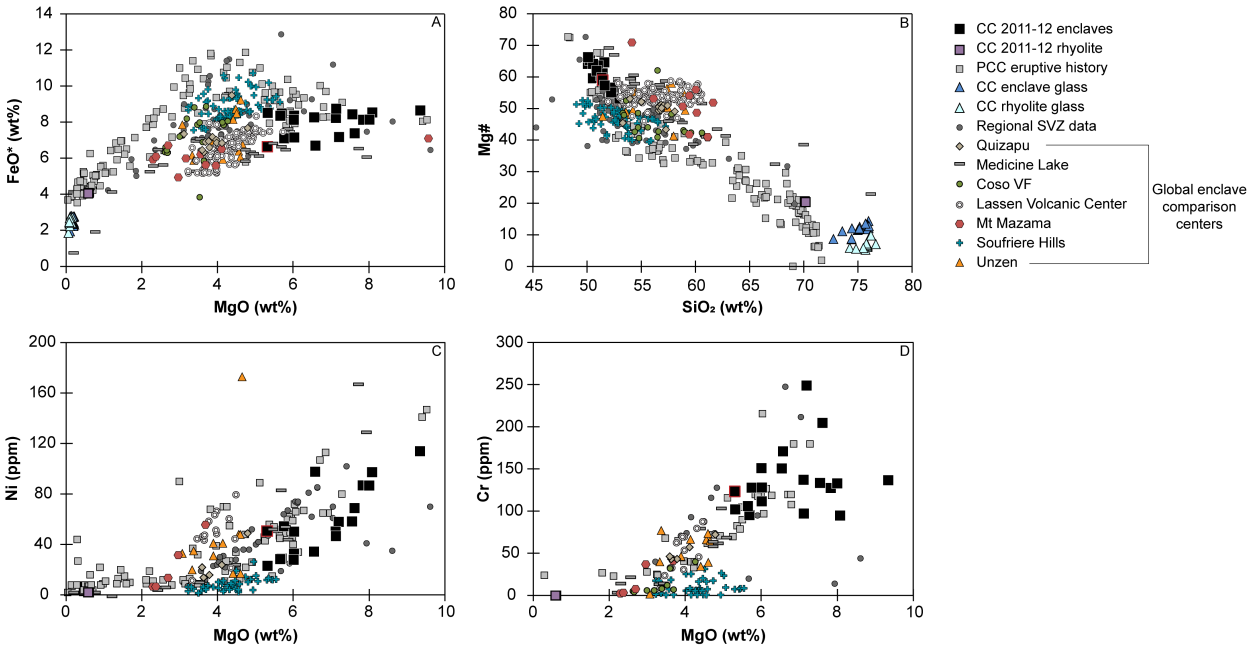

Figure 2.4. Global geochemical compilation of mafic enclaves (XRF data). 2011-12 CC enclaves are at primitive extent. CC: Cordón Caulle. Black square: 2011-12 CC mafic enclaves. Black square with red outline: indicates porphyritic enclave population among CC enclaves. Purple square: 2011-12 CC rhyolite. Grey square: PCC eruptive history (EarthChem). Triangles: 2011-12 CC enclave and rhyolite glass (EMP data). Dk Grey circle: Regional SVZ data (EarthChem). Global enclave comparison centers: Quizapu, Medicine Lake, Coso VF, Lassen Volcanic Center, Mt Mazama, Soufriere Hills, Unzen. References for global centers in ESM 2.1.

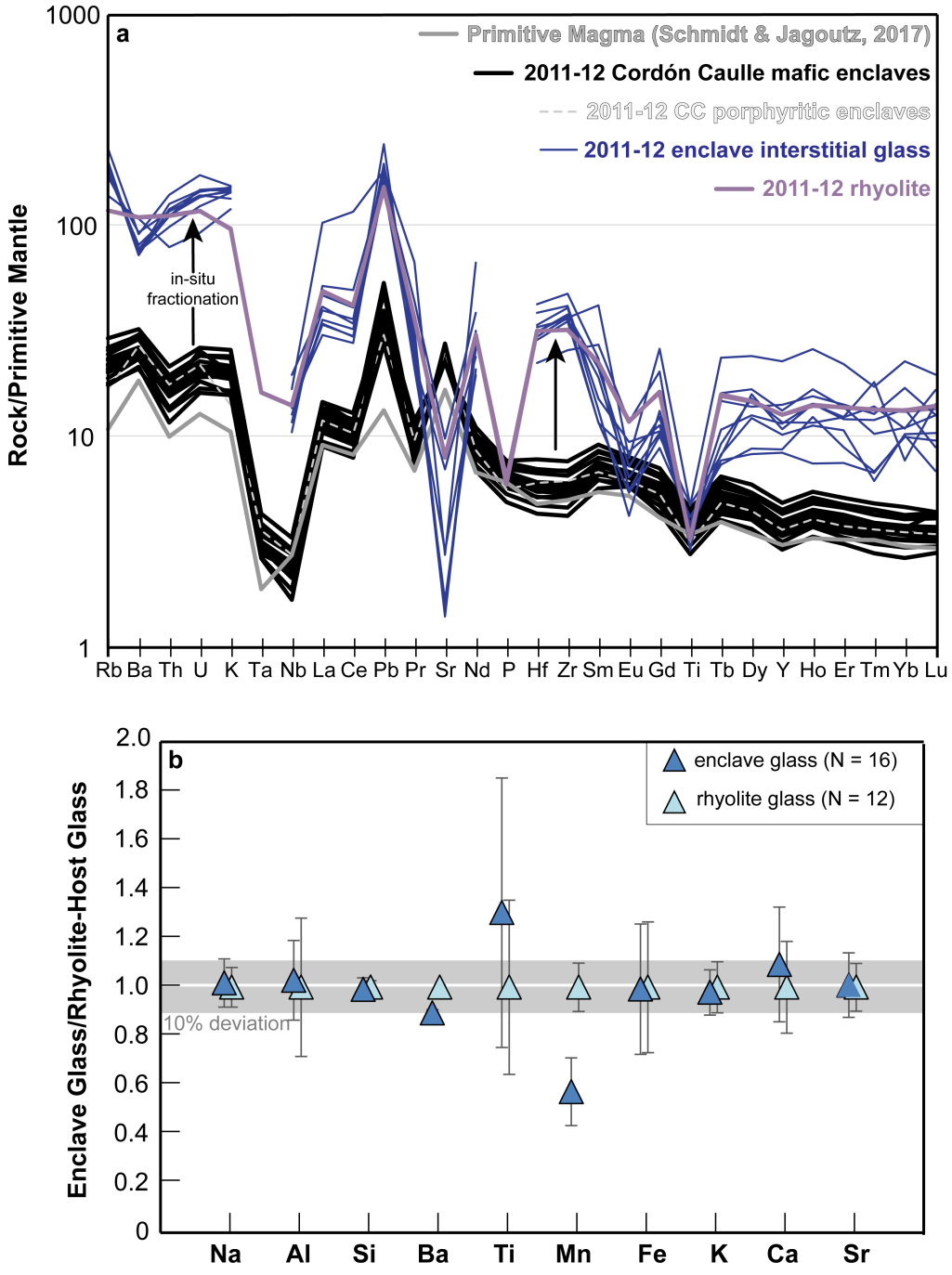

Figure 2.5. (a) Incompatible trace element spider diagram (XRF+ICP-MS data) normalized to primitive mantle[63]. Grey line: representative primitive magma[32]. Black line: 2011-12 CC mafic enclaves. Dashed light grey line: 2011-12 CC porphyritic enclaves. Thin dark purple line: 2011-12 mafic enclave interstitial glass data (LA-ICP-MS). Light Purple: 2011-12 host rhyolite (XRF+ICP-MS). Arrows indicate symmetrical elevation of rhyolite data from mafic enclaves suggestive of in-situ fractionation. (b) 2011-12 CC mafic enclave interstitial glass normalized to host rhyolite glass and display overlapping compositions. Symbols are the same as Fig. 2.4.

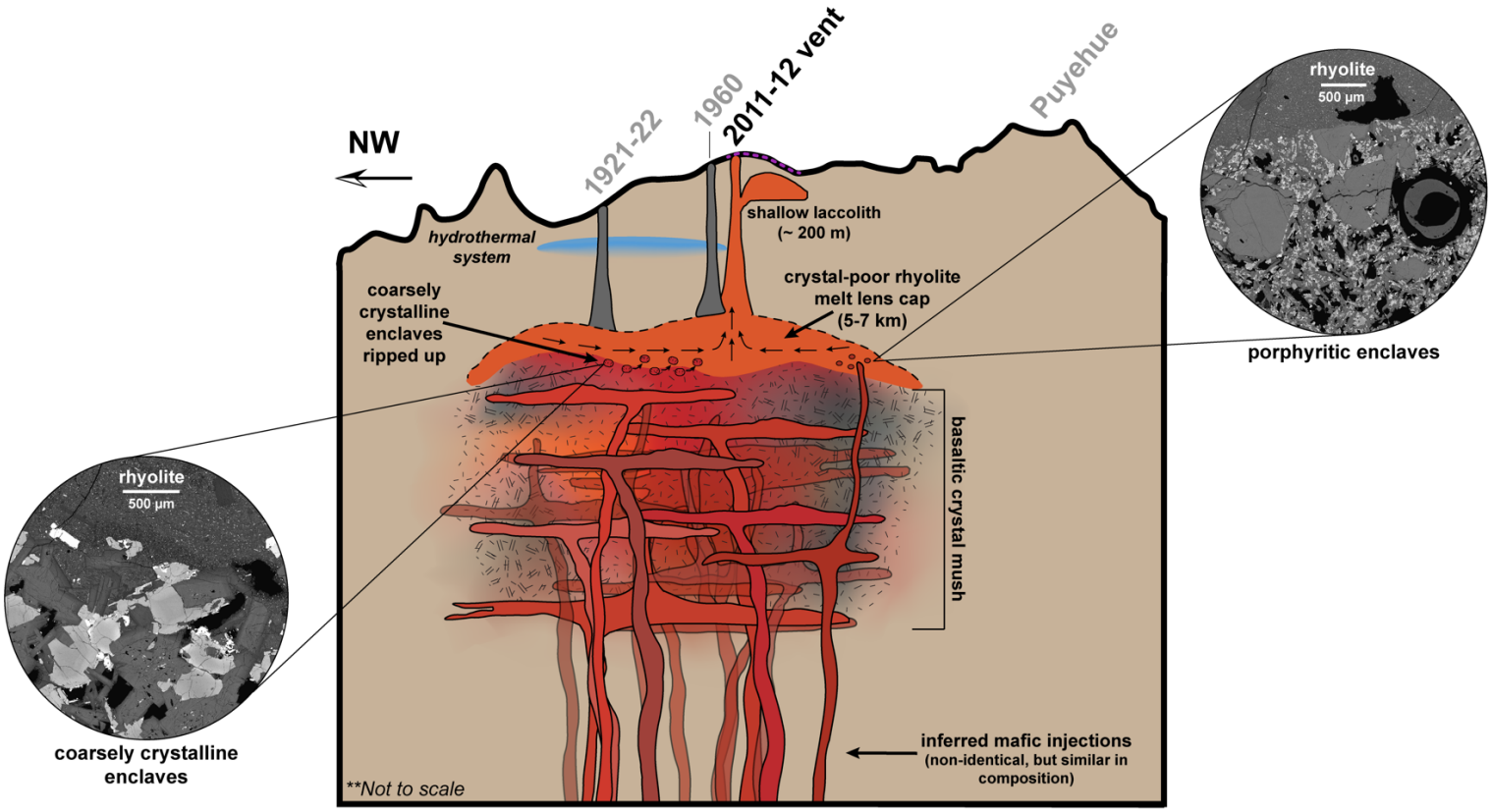

Figure 2.6. Schematic diagram for Cordón Caulle plumbing system (not to vertical scale). Inferred mafic injections[22] fuel overlying crystal mush. Shades of orange-red in mafic injections and crystal mush represent compositional heterogeneity observed in chemistry. Stippled texture in crystal mush represents different levels of crystallinity. Black portions of crystal mush represent low-melt content or inactive heterogeneities within the mush. Crystal mush is overlain by crystal-poor rhyolite (orange). Coarsely crystalline fragments are entrained into rhyolite prior to or upon eruption preserving remnants of the mush in the form of mafic enclaves. Some injections bypass the mush chemically unobstructed and interact directly with rhyolite to form porphyritic enclave population. Arrows in rhyolite melt cap represent June 4-7, 2011 magma flux[22]. Dashed purple line: surficial uplift from laccolith emplacement. Circular outsets are BSE images of enclave-host boundary for both enclave populations. Schematic does not infer magmatic architecture underlying Puyehue volcano.

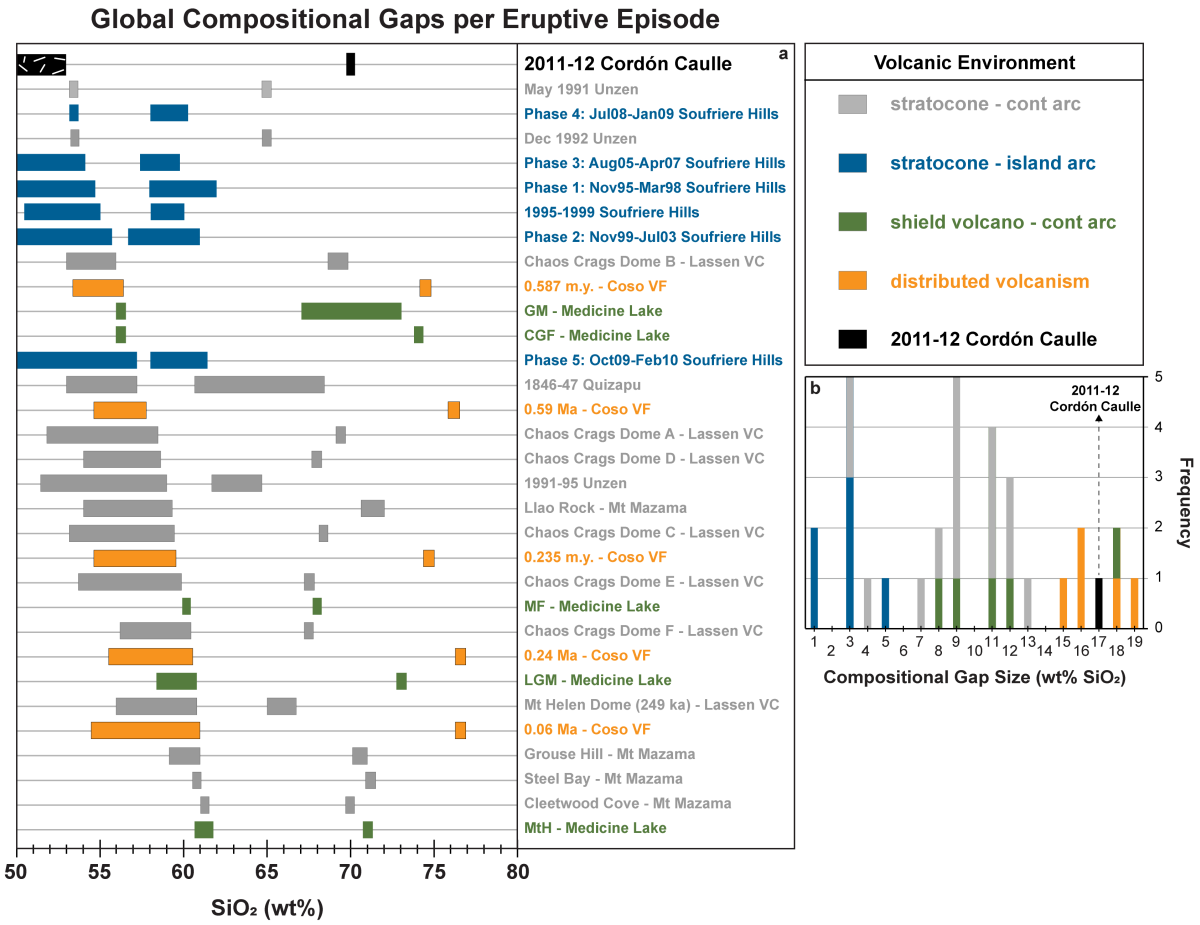

Figure 2.7. (a) Compositional gap data for 2011-12 Cordón Caulle eruption compared to global eruptions with compositional gaps between enclaves and host lavas. (b) Frequency diagram of compositional gap magnitude. 2011-12 CC eruption produced 17 wt% SiO2 compositional gap. For typical on-arc systems, compositional gaps range from<1-14 wt% SiO2 making CC an end-member. Figure is color coordinated to volcanic environment. Black: 2011-12 Cordón Caulle eruption (continental on-arc system). Grey: stratocones/continental on-arc systems. Blue: stratocones/island arc systems. Green: shield volcano/continental arc system. Orange: distributed volcanism. References for compiled eruptions located in ESM 2.1.

Supplementary Materials

ESM 2.1. Excel file with all analytical conditions and raw data collected for this study as well as list of references for global enclave compilation and compositional gap per eruption. To access data, see link for “Supplementary Information 1”:
https://www.nature.com/articles/s41598-022-13305-y

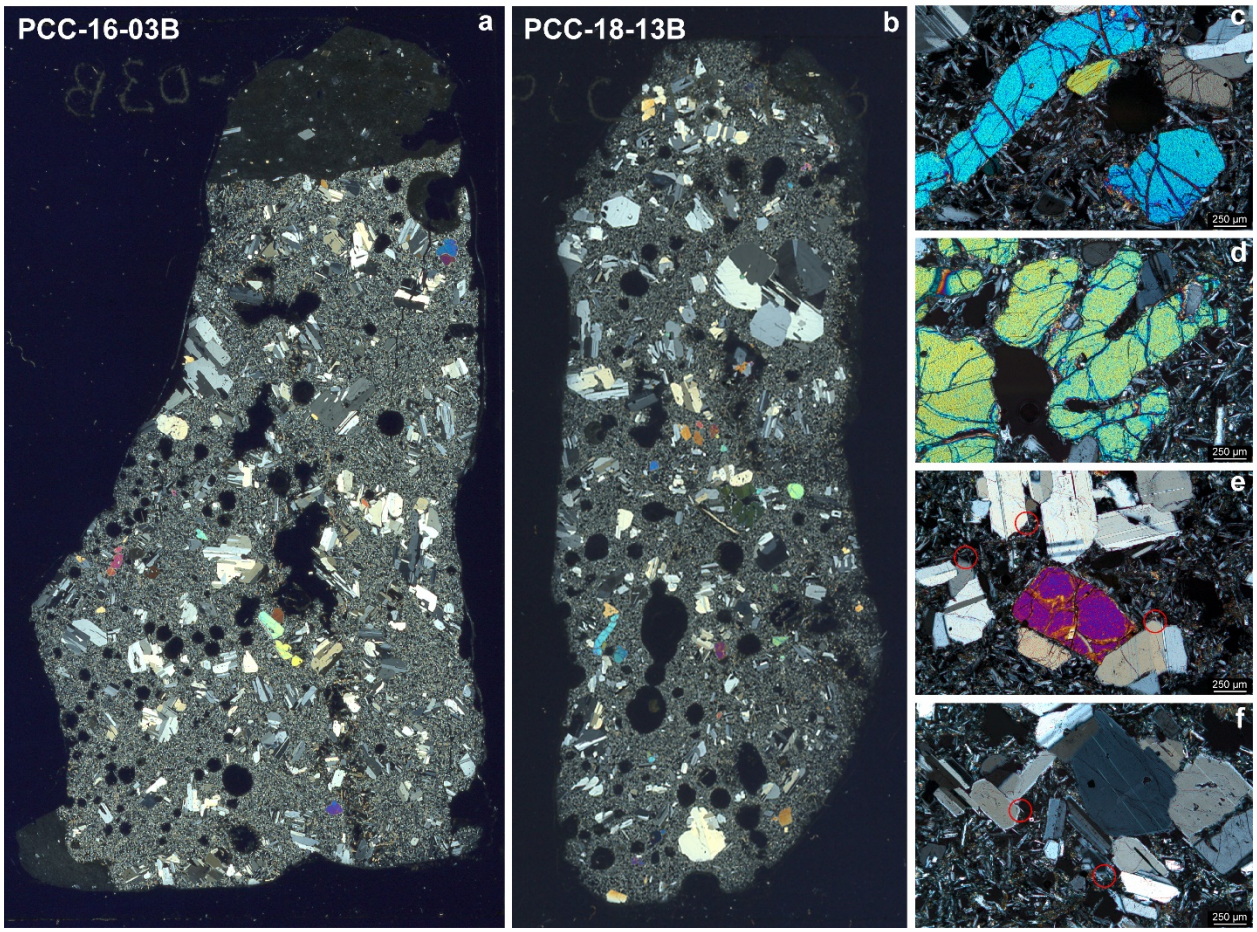

ESM 2.2. Textural images of the porphyritic enclave population. (a-b) Thin section scans of porphyritic enclaves highlighting crystallinity, glomerocrysts, mineralogy, and vesicle shape. (c-d) Micrographs of skeletal olivine texture. (e-f) Micrographs of plagioclase glomerocrysts. Red circles highlight swallowtail disequilibrium texture.

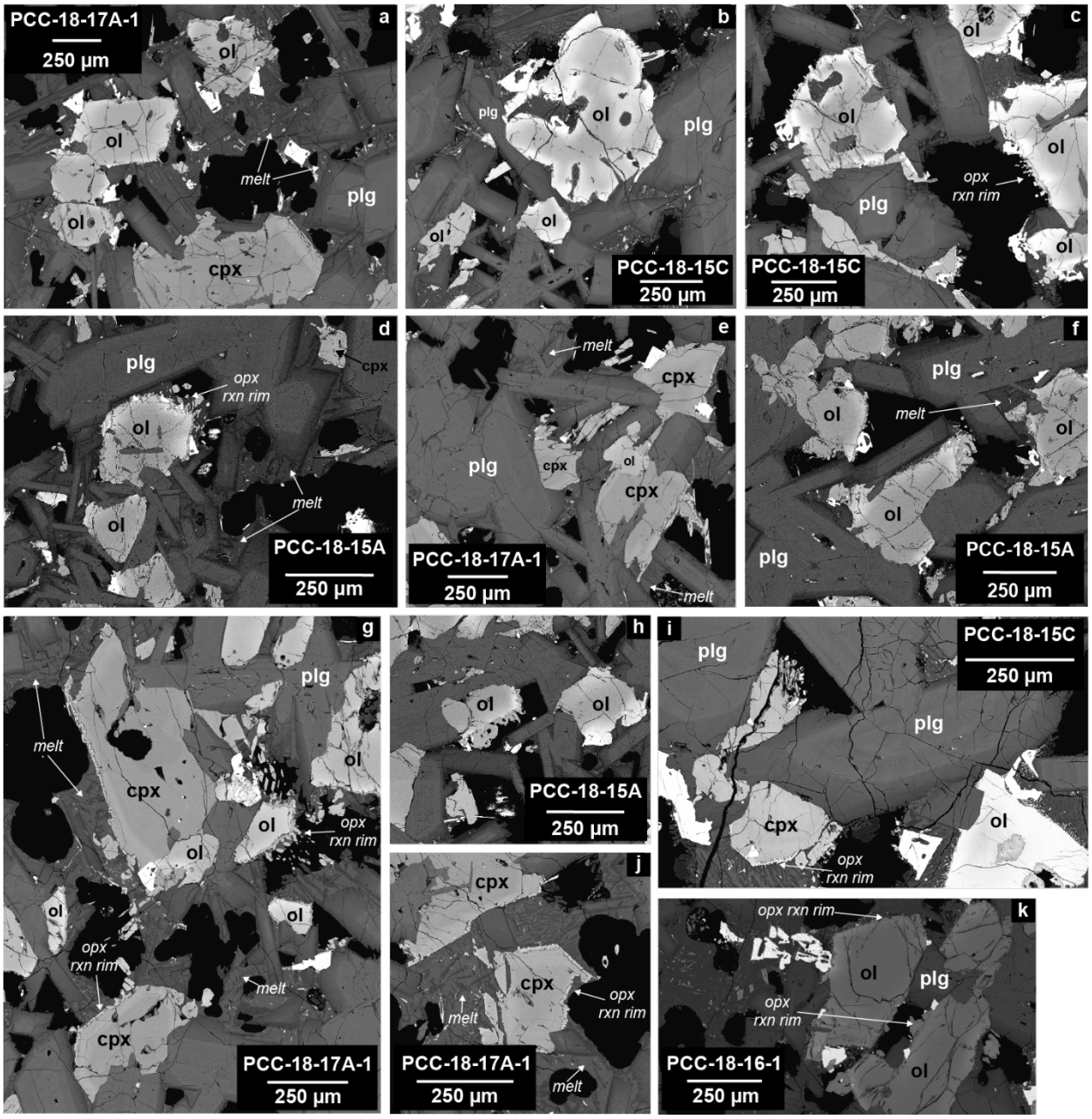

ESM 2.3. BSE images of coarsely crystalline enclaves. Panels highlight intergrown textures, plagioclase zonation, and plagioclase resorption/sieve textures. Plagioclase zonation "core-mantle-rim" notated in panel (b, g, i).

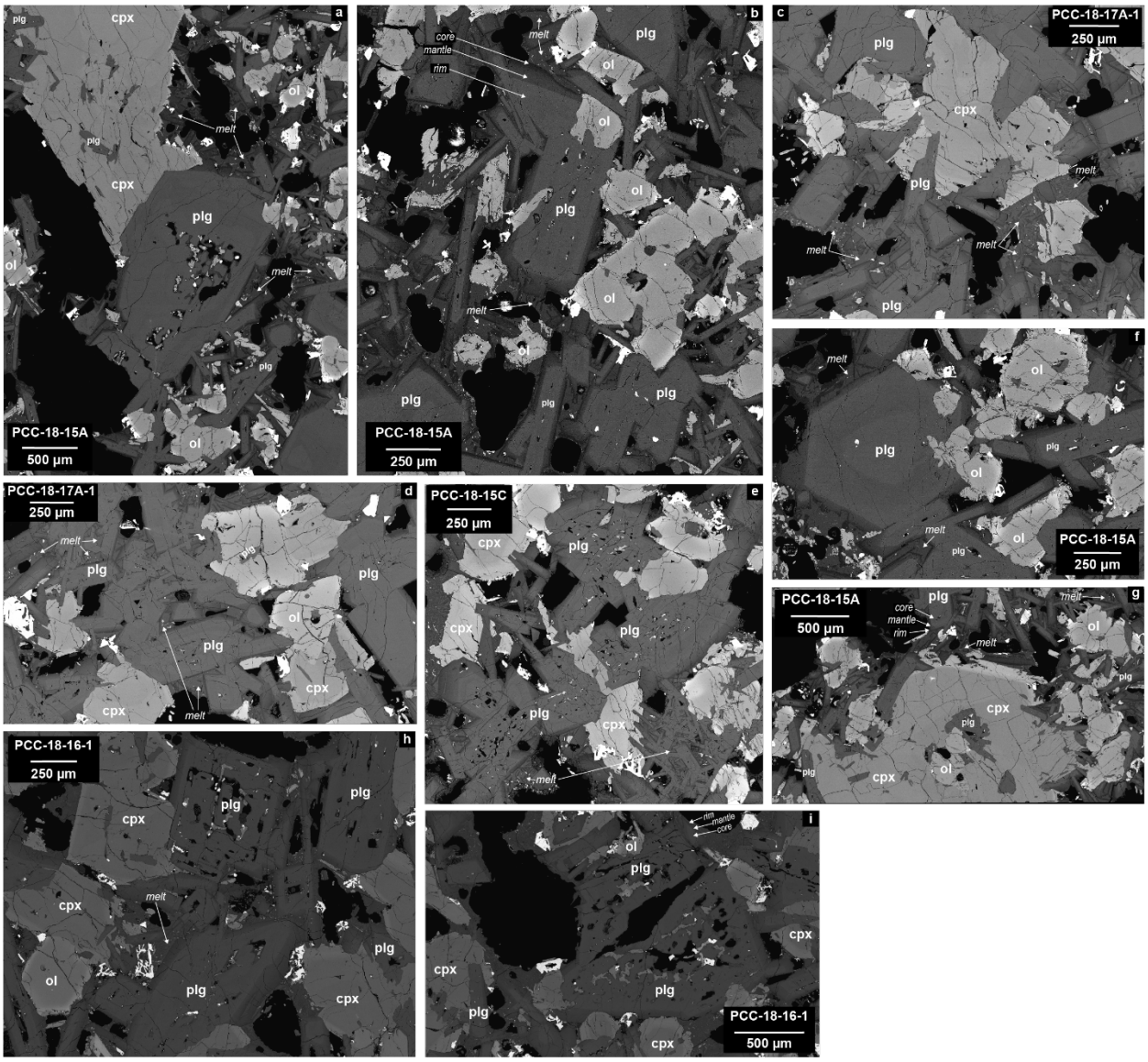

ESM 2.4. BSE images of coarsely crystalline enclaves. Panels highlight orthopyroxene reaction rims on olivine and clinopyroxene. “Opx rxn rim” notated on panels (c, d, g, j, k).

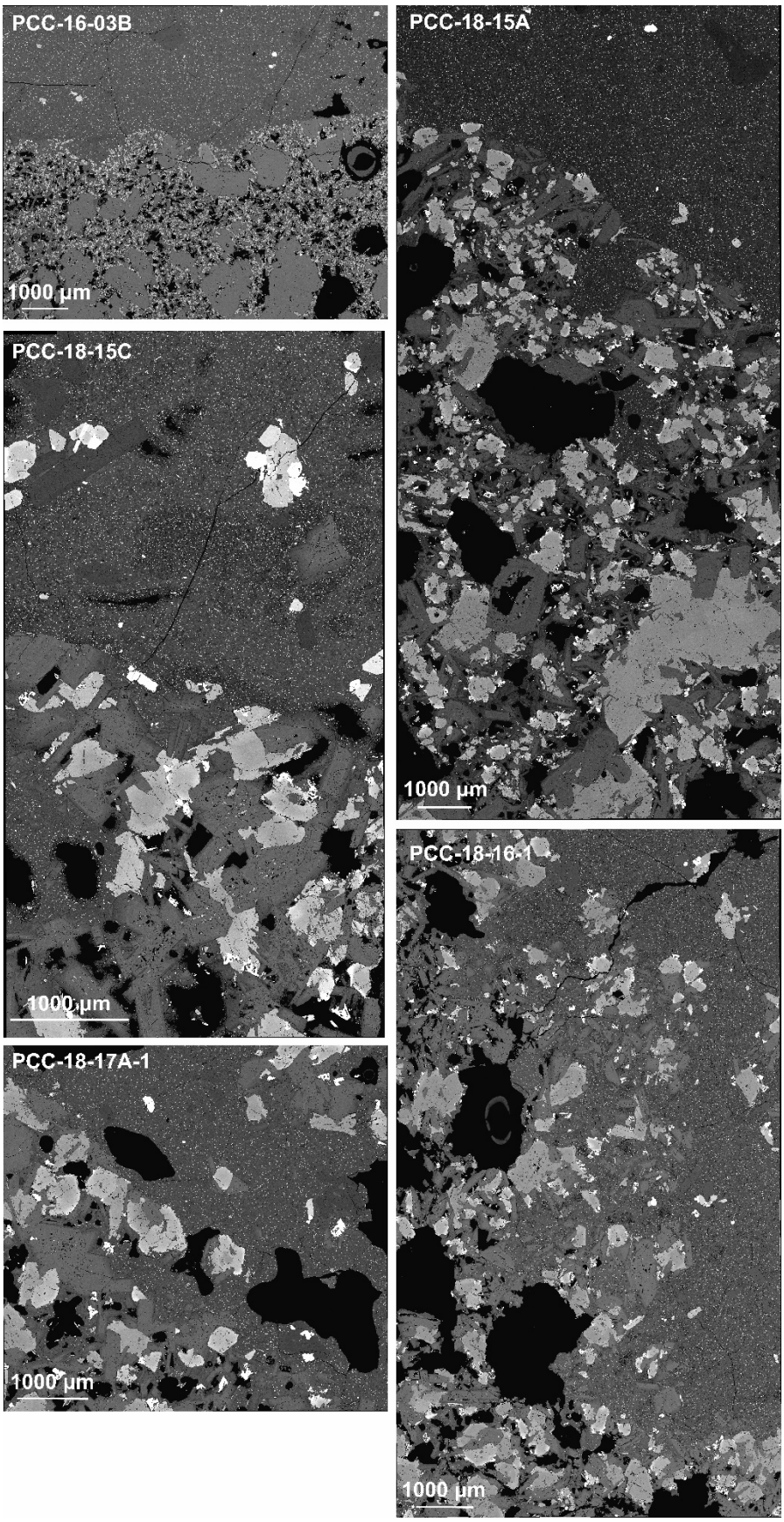

ESM 2.5. BSE maps of enclave-host boundary. Sample PCC-16-03B is the porphyritic population and the rest are of the coarsely crystalline population. PCC-18-15C displays heterogeneous strands in groundmass at boundary (dark grey vs light grey).

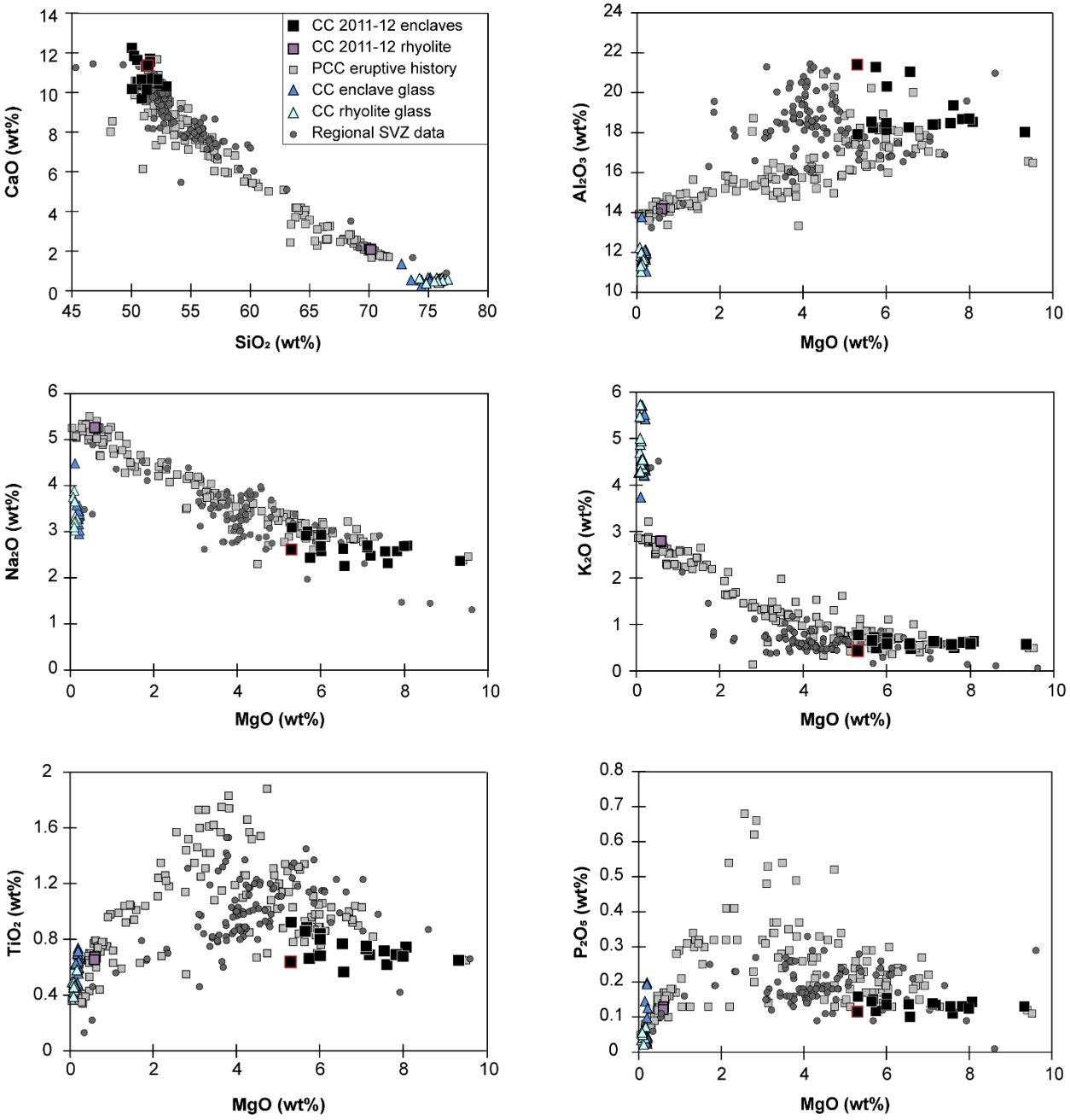

ESM 2.6. Geochemical Harker diagrams. Symbols are the same as Fig. 2.4.

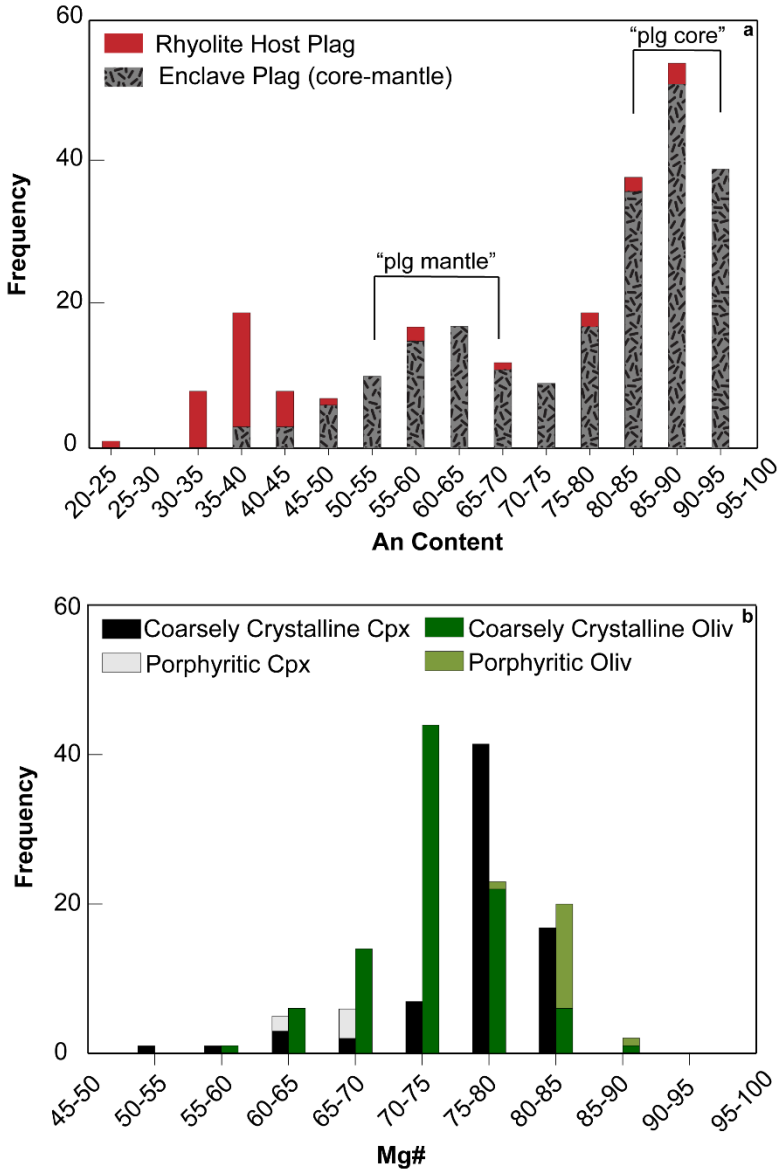

ESM 2.7. Mineral geochemistry for plagioclase, olivine, and clinopyroxene. (a) An content for plagioclase in both enclave populations. Frequency bins are 5 mol%. Plagioclase core-mantle zonation labeled for coarsely crystalline enclaves. (b) Mg# frequency bins for olivine and clinopyroxene. Dk green: Olivine in coarsely crystalline population. Lt green: Olivine in porphyritic population. Black: Cpx coarsely crystalline population. Lt grey: Cpx porphyritic population. Porphyritic olivine displays tightly bound range at higher Mg# compared to coarsely crystalline olivine.

References

1. Bacon, C. R., & Metz, J. (1984). Magmatic inclusions in rhyolites, contaminated basalts, and compositional zonation beneath the Coso volcanic field, California. *Contributions to Mineralogy and Petrology*, 85(4), 346–365. https://doi.org/10.1007/BF01150292

2. Eichelberger, J. C. (1980). Vesiculation of mafic magma during replenishment of silicic magma reservoirs. *Nature*, 288(5790), 446–450. https://doi.org/10.1038/288446a0

3. Bacon, C. R., & Druitt, T. H. (1988). Compositional evolution of the zoned calcalkaline magma chamber of Mount Mazama, Crater Lake, Oregon. *Contributions to Mineralogy and Petrology*, 98(2), 224–256. https://doi.org/10.1007/BF00402114

4. Scruggs, M. A., & Putirka, K. D. (2018). Eruption triggering by partial crystallization of mafic enclaves at Chaos Crags, Lassen Volcanic Center, California. *American Mineralogist*, 103(10), 1575–1590. https://doi.org/10.2138/am-2018-6058

5. Bachmann, O., & Bergantz, G. W. (2004). On the Origin of Crystal-poor Rhyolites: Extracted from Batholithic Crystal Mushes. *Journal of Petrology*, 45(8), 1565–1582. https://doi.org/10.1093/petrology/egh019

6. Hildreth, W. (2004). Volcanological perspectives on Long Valley, Mammoth Mountain, and Mono Craters: Several contiguous but discrete systems. *Journal of Volcanology and Geothermal Research*, 136(3–4), 169–198. https://doi.org/10.1016/j.jvolgeores.2004.05.019

7. Cashman, K. V., Sparks, R. S. J., & Blundy, J. D. (2017). Vertically extensive and unstable magmatic systems: A unified view of igneous processes. *Science*, 355(6331), eaag3055. https://doi.org/10.1126/science.aag3055

8. Bachmann, O., & Bergantz, G. W. (2003). Rejuvenation of the Fish Canyon magma body: A window into the evolution of large-volume silicic magma systems. *Geology*, 31(9), 789. https://doi.org/10.1130/G19764.1

9. Pallister, J. S., Hoblitt, R. P., Crandell, D. R., & Mullineaux, D. R. (1992). Mount St. Helens a decade after the 1980 eruptions: Magmatic models, chemical cycles, and a revised hazards assessment. *Bulletin of Volcanology*, 54(2), 126–146. https://doi.org/10.1007/BF00278003

10. Eichelberger, J. C., Chertkoff, D. G., Dreher, S. T., & Nye, C. J. (2000). Magmas in collision: Rethinking chemical zonation in silicic magmas. *Geology*, 28(7), 603–606. https://doi.org/10.1130/0091-7613(2000)28<603:MICRCZ>2.0.CO;2

11. Miller, C. F., & Wark, D. A. (2008). SUPERVOLCANOES AND THEIR EXPLOSIVE SUPERERUPTIONS. *Elements*, 4(1), 11–15. https://doi.org/10.2113/GSELEMENTS.4.1.11

12. Brophy, J. G. (1991). Composition gaps, critical crystallinity, and fractional crystallization in orogenic (calc-alkaline) magmatic systems. *Contributions to Mineralogy and Petrology*, 109(2), 173–182. https://doi.org/10.1007/BF00306477

13. Dufek, J., & Bachmann, O. (2010). Quantum magmatism: Magmatic compositional gaps generated by melt-crystal dynamics. *Geology*, 38(8), 687–690. https://doi.org/10.1130/G30831.1

14. Lara, L. E., Naranjo, J. A., & Moreno, H. (2004). Rhyodacitic fissure eruption in Southern Andes (Cordón Caulle; 40.5°S) after the 1960 (Mw:9.5) Chilean earthquake: A structural interpretation. *Journal of Volcanology and Geothermal Research*, 138(1–2), 127–138. https://doi.org/10.1016/j.jvolgeores.2004.06.009

15. Singer, B. S., Jicha, B. R., Harper, M. A., Naranjo, J. A., Lara, L. E., & Moreno-Roa, H. (2008). Eruptive history, geochronology, and magmatic evolution of the Puyehue-Cordón Caulle volcanic complex, Chile. *Geological Society of America Bulletin*, 120(5–6), 599–618. https://doi.org/10.1130/B26276.1

16. Lara, L. E., Moreno, H., Naranjo, J. A., Matthews, S., & Pérez de Arce, C. (2006). Magmatic evolution of the Puyehue–Cordón Caulle Volcanic Complex (40° S), Southern Andean Volcanic Zone: From shield to unusual rhyolitic fissure volcanism. *Journal of Volcanology and Geothermal Research*, 157(4), 343–366. https://doi.org/10.1016/j.jvolgeores.2006.04.010

17. Castro, J. M., Schipper, C. I., Mueller, S. P., Militzer, A. S., Amigo, A., Parejas, C. S., & Jacob, D. (2013). Storage and eruption of near-liquidus rhyolite magma at Cordón Caulle, Chile. *Bulletin of Volcanology*, 75(4), 702. https://doi.org/10.1007/s00445-013-0702-9

18. Jay, J., Costa, F., Pritchard, M., Lara, L., Singer, B., & Herrin, J. (2014). Locating magma reservoirs using InSAR and petrology before and during the 2011–2012 Cordón Caulle silicic eruption. *Earth and Planetary Science Letters*, 395, 254–266. https://doi.org/10.1016/j.epsl.2014.03.046

19. Alloway, B. V., Pearce, N. J. G., Villarosa, G., Outes, V., & Moreno, P. I. (2015). Multiple melt bodies fed the AD 2011 eruption of Puyehue-Cordón Caulle, Chile. *Scientific Reports*, 5(1), 17589. https://doi.org/10.1038/srep17589

20. Seropian, G., Schipper, C. I., Harmon, L. J., Smithies, S. L., Kennedy, B. M., Castro, J. M., Alloway, B. V., & Forte, P. (2021). A century of ongoing silicic volcanism at Cordón Caulle, Chile: New constraints on the magmatic system involved in the 1921–1922, 1960 and 2011–2012 eruptions. *Journal of Volcanology and Geothermal Research*, 420, 107406. https://doi.org/10.1016/j.jvolgeores.2021.107406

21. Delgado, F., Pritchard, M. E., Basualto, D., Lazo, J., Córdova, L., & Lara, L. E. (2016). Rapid reinflation following the 2011-2012 rhyodacite eruption at Cordón Caulle volcano (Southern Andes) imaged by InSAR: Evidence for magma reservoir refill: Inflation After

a Silicic Eruption. *Geophysical Research Letters*, 43(18), 9552–9562. https://doi.org/10.1002/2016GL070066

22. Delgado, F., Pritchard, M., Samsonov, S., & Córdova, L. (2018). Renewed Posteruptive Uplift Following the 2011-2012 Rhyolitic Eruption of Cordón Caulle (Southern Andes, Chile): Evidence for Transient Episodes of Magma Reservoir Recharge During 2012-2018. *Journal of Geophysical Research: Solid Earth*, 123(11), 9407–9429. https://doi.org/10.1029/2018JB016240

23. Castro, J. M., Cordónnier, B., Schipper, C. I., Tuffen, H., Baumann, T. S., & Feisel, Y. (2016). Rapid laccolith intrusion driven by explosive volcanic eruption. *Nature Communications*, 7(1), 13585. https://doi.org/10.1038/ncomms13585

24. Delgado, F. (2021). Rhyolitic volcano dynamics in the Southern Andes: Contributions from 17 years of InSAR observations at Cordón Caulle volcano from 2003 to 2020. *Journal of South American Earth Sciences*, 106, 102841. https://doi.org/10.1016/j.jsames.2020.102841

25. Bacon, C. R. (1986). Magmatic inclusions in silicic and intermediate volcanic rocks. *Journal of Geophysical Research*, 91(B6), 6091. https://doi.org/10.1029/JB091iB06p06091

26. Silva, S. L. de. (1989). The origin and significance of crystal rich inclusions in pumices from two Chilean ignimbrites. *Geological Magazine*, 126(2), 159–175. https://doi.org/10.1017/S0016756800006300

27. Ruprecht, P., Simon, A. C., & Fiege, A. (2020). The Survival of Mafic Magmatic Enclaves and the Timing of Magma Recharge. *Geophysical Research Letters*, 47(14). https://doi.org/10.1029/2020GL087186

28. Holness, M. B., Stock, M. J., & Geist, D. (2019). Magma chambers versus mush zones: Constraining the architecture of sub-volcanic plumbing systems from microstructural analysis of crystalline enclaves. Philosophical Transactions of the Royal Society A: Mathematical, Physical and Engineering Sciences, 377(2139), 20180006. https://doi.org/10.1098/rsta.2018.0006

29. Holness, M. B. (2014). The effect of crystallization time on plagioclase grain shape in dolerites. Contributions to Mineralogy and Petrology, 168(5), 1076. https://doi.org/10.1007/s00410-014-1076-5

30. Winslow, H., Ruprecht, P., Stelten, M., & Amigo, A. (2020). Evidence for primitive magma storage and eruption following prolonged equilibration in thickened crust. Bulletin of Volcanology, 82(11), 69. https://doi.org/10.1007/s00445-020-01406-3

31. Tsuchiyama, A. (1986). Experimental study of olivine-melt reaction and its petrological implications. Journal of Volcanology and Geothermal Research, 29(1), 245–264. https://doi.org/10.1016/0377-0273(86)90047-8

32. Schmidt, M. W., & Jagoutz, O. (2017). The global systematics of primitive arc melts. Geochemistry, Geophysics, Geosystems, 18(8), 2817–2854. https://doi.org/10.1002/2016GC006699

33. Grove, T. L., & Donnelly-Nolan, J. M. (1986). The evolution of young silicic lavas at Medicine Lake Volcano, California: Implications for the origin of compositional gaps in calc-alkaline series lavas. Contributions to Mineralogy and Petrology, 92(3), 281–302. https://doi.org/10.1007/BF00572157

34. Grove, T. L., Donnelly-Nolan, J. M., & Housh, T. (1997). Magmatic processes that generated the rhyolite of Glass Mountain, Medicine Lake volcano, N. California. Contributions to Mineralogy and Petrology, 127(3), 205–223. https://doi.org/10.1007/s004100050276

35. Stock, M. J., Taylor, R. N., & Gernon, T. M. (2012). Triggering of major eruptions recorded by actively forming cumulates. Scientific Reports, 2(1), 731. https://doi.org/10.1038/srep00731

36. Hammer, J. E. (2008). Experimental Studies of the Kinetics and Energetics of Magma Crystallization. Reviews in Mineralogy and Geochemistry, 69(1), 9–59. https://doi.org/10.2138/rmg.2008.69.2

37. Fagents, S. A., Gregg, T. K. P., & Lopes, R. M. C. (2013). Modeling Volcanic Processes: The Physics and Mathematics of Volcanism. Cambridge University Press.

38. Boudreau, B. P. (2012). The physics of bubbles in surficial, soft, cohesive sediments. Marine and Petroleum Geology, 38(1), 1–18. https://doi.org/10.1016/j.marpetgeo.2012.07.002

39. Boudreau, A. (2016). Bubble migration in a compacting crystal-liquid mush. Contributions to Mineralogy and Petrology, 171(4), 32. https://doi.org/10.1007/s00410-016-1237-9

40. Druitt, T. H., & Bacon, C. R. (1989). Petrology of the zoned calcalkaline magma chamber of Mount Mazama, Crater Lake, Oregon. Contributions to Mineralogy and Petrology, 101(2), 245–259. https://doi.org/10.1007/BF00375310

41. Murphy, M. D., Sparks, R. S. J., Barclay, J., Carroll, M. R., & Brewer, T. S. (2000). Remobilization of Andesite Magma by Intrusion of Mafic Magma at the Soufriere Hills Volcano, Montserrat, West Indies. Journal of Petrology, 41(1), 21–42. https://doi.org/10.1093/petrology/41.1.21

42. Botcharnikov, R. E., Holtz, F., Almeev, R. R., Sato, H., & Behrens, H. (2008). Storage conditions and evolution of andesitic magma prior to the 1991–95 eruption of Unzen volcano: Constraints from natural samples and phase equilibria experiments. Journal of Volcanology and Geothermal Research, 175(1), 168–180. https://doi.org/10.1016/j.jvolgeores.2008.03.026

43. Feeley, T. C., Wilson, L. F., & Underwood, S. J. (2008). Distribution and compositions of magmatic inclusions in the Mount Helen dome, Lassen Volcanic Center, California: Insights into magma chamber processes. Lithos, 106(1–2), 173–189. https://doi.org/10.1016/j.lithos.2008.07.010

44. Chen, C.-H., Nakada, S., Shieh, Y.-N., & DePaolo, D. J. (1999). The Sr, Nd and O isotopic studies of the 1991–1995 eruption at Unzen, Japan. Journal of Volcanology and Geothermal Research, 89(1–4), 243–253. https://doi.org/10.1016/S0377-0273(99)00002-5

45. Ruprecht, P., Bergantz, G. W., Cooper, K. M., & Hildreth, W. (2012). The Crustal Magma Storage System of Volcán Quizapu, Chile, and the Effects of Magma Mixing on Magma Diversity. Journal of Petrology, 53(4), 801–840. https://doi.org/10.1093/petrology/egs002

46. Plail, M., Barclay, J., Humphreys, M. C. S., Edmonds, M., Herd, R. A., & Christopher, T. E. (2014). Chapter 18 Characterization of mafic enclaves in the erupted products of Soufrière Hills Volcano, Montserrat, 2009 to 2010. Geological Society, London, Memoirs, 39(1), 343–360. https://doi.org/10.1144/M39.18

47. Plail, M., Edmonds, M., Woods, A. W., Barclay, J., Humphreys, M. C. S., Herd, R. A., & Christopher, T. (2018). Mafic enclaves record syn-eruptive basalt intrusion and mixing. Earth and Planetary Science Letters, 484, 30–40. https://doi.org/10.1016/j.epsl.2017.11.033

48. Lofgren, G. (1974). An experimental study of plagioclase crystal morphology; isothermal crystallization. American Journal of Science, 274(3), 243–273. https://doi.org/10.2475/ajs.274.3.243

49. Clynne, M. A. (1999). A Complex Magma Mixing Origin for Rocks Erupted in 1915, Lassen Peak, California. Journal of Petrology, 40(1), 105–132. https://doi.org/10.1093/petroj/40.1.105

50. Schleicher, J. M., Bergantz, G. W., Breidenthal, R. E., & Burgisser, A. (2016). Time scales of crystal mixing in magma mushes. Geophysical Research Letters, 43(4), 1543–1550. https://doi.org/10.1002/2015GL067372

51. Barbarin, B., & Didier, J. (1992). Genesis and evolution of mafic microgranular enclaves through various types of interaction between coexisting felsic and mafic magmas. Earth and Environmental Science Transactions of The Royal Society of Edinburgh, 83(1–2), 145–153. https://doi.org/10.1017/S0263593300007835

52. Hodge, K. F., & Jellinek, A. M. (2020). The Influence of Magma Mixing on the Composition of Andesite Magmas and Silicic Eruption Style. Geophysical Research Letters, 47(13), e2020GL087439. https://doi.org/10.1029/2020GL087439

53. Gelman, S. E., Deering, C. D., Bachmann, O., Huber, C., & Gutiérrez, F. J. (2014). Identifying the crystal graveyards remaining after large silicic eruptions. Earth and Planetary Science Letters, 403, 299–306. https://doi.org/10.1016/j.epsl.2014.07.005

54. Fiedrich, A. M., Bachmann, O., Ulmer, P., Deering, C. D., Kunze, K., & Leuthold, J. (2017). Mineralogical, geochemical, and textural indicators of crystal accumulation in the Adamello Batholith (Northern Italy). American Mineralogist, 102(12), 2467–2483. https://doi.org/10.2138/am-2017-6026

55. Bachmann, O., & Bergantz, G. (2008). The magma reservoirs that feed supereruptions. Elements, 4(1), 17-21.

56. Holness, M. B., & Bunbury, J. M. (2006). Insights into continental rift-related magma chambers: Cognate nodules from the Kula Volcanic Province, Western Turkey. Journal of Volcanology and Geothermal Research, 153(3), 241–261. https://doi.org/10.1016/j.jvolgeores.2005.12.004

57. Christopher, T. E., Blundy, J., Cashman, K., Cole, P., Edmonds, M., Smith, P. J., Sparks, R. S. J., & Stinton, A. (2015). Crustal-scale degassing due to magma system destabilization and magma-gas decoupling at Soufrière Hills Volcano, Montserrat. Geochemistry, Geophysics, Geosystems, 16(9), 2797–2811. https://doi.org/10.1002/2015GC005791

58. Sisson, T. W., & Bacon, C. R. (1999). Gas-driven filter pressing in magmas. Geology, 27(7), 613. https://doi.org/10.1130/0091-7613(1999)027<0613:GDFPIM>2.3.CO;2

59. Johnson, D., Hooper, P., & Conrey, R. (1999). XRF method XRF analysis of rocks and minerals for major and trace elements on a single low dilution Li-tetraborate fused bead. Advances in X-ray Analysis, 41, 843-867.

60. Donovan, J. J., Singer, J. W., & Armstrong, J. T. (2016). A new EPMA method for fast trace element analysis in simple matrices. American Mineralogist, 101(8), 1839–1853. https://doi.org/10.2138/am-2016-5628

61. Woodhead, J. D., Hellstrom, J., Hergt, J. M., Greig, A., & Maas, R. (2007). Isotopic and Elemental Imaging of Geological Materials by Laser Ablation Inductively Coupled Plasma-Mass Spectrometry. Geostandards and Geoanalytical Research, 31(4), 331–343. https://doi.org/10.1111/j.1751-908X.2007.00104.x

62. Paton, C., Hellstrom, J., Paul, B., Woodhead, J., & Hergt, J. (2011). Iolite: Freeware for the visualisation and processing of mass spectrometric data. Journal of Analytical Atomic Spectrometry, 26(12), 2508–2518. https://doi.org/10.1039/C1JA10172B

63. McDonough, W. F., & Sun, S. -s. (1995). The composition of the Earth. Chemical *Geology*, 120(3), 223–253. https://doi.org/10.1016/0009-2541(94)00140-4

Chapter 3

Revealing the thermal history of an active basaltic crystal mush

Heather Winslow[1], Philipp Ruprecht[1]

[1]*University of Nevada, Reno*

Abstract

The thermal history of an active crystal mush was constrained using Mg-in-plagioclase thermometry and geospeedometry in basalt. While this method was developed using gabbroic rocks at oceanic spreading centers, we expanded its application to crystal-rich volcanic rocks to infer the thermal evolution of a magma mush at Cordón Caulle, Chile. Instantaneous cooling paths were found to be the best fit model with magma storage lasting from hundreds to thousands of years prior to eruption. These estimates provide insight for the mechanism of enclave incorporation and the lifetime of a crystal mush at an active volcanic complex. Other quantitative estimates were conducted to constrain details of the magmatic architecture using aluminum partitioning in olivine-spinel thermometry and clinopyroxene-liquid barometry. Results support the conceptual model of a shallow and spatially contiguous crystal-rich basaltic mush directly producing an overlying rhyolitic melt cap.

Introduction

Crystal-rich magma mushes have become an increasingly common conceptual model to envision magmatic storage architectures for volcanic systems globally (Nakamura, 1995; Bachmann & Bergantz, 2004; Hildreth, 2004; Cooper et al., 2016; Cashman et al., 2017). Their interconnected storage results in the ability to produce numerous eruptions that are many times explosive and hazardous in nature (Cashman et al., 2017). The thermal conditions and evolution of crystal mushes are not well understood even though they are important factors to better understand the frequency, duration, and intensity of eruptions (Lubbers et al., 2022). Recently Faak et al. (2013) calibrated a Mg-exchange thermometer between plagioclase and clinopyroxene and presented new Mg diffusivity coefficients for plagioclase. Using these experimental results, they explored thermal conditions and cooling rates of gabbro in oceanic

spreading ridges (Faak et al., 2014; 2015; Faak & Gillis, 2016). Here we apply the Mg-in-plagioclase thermometer and geospeedometer on basaltic mafic enclaves from the 2011-12 Cordón Caulle eruption in southern Chile previously interpreted as pieces of an active crystal mush (Winslow et al., 2022). We use highly crystalline basalt with touching plagioclase and clinopyroxene pairs, assumed to be in equilibrium in the assemblage, to recover the thermal conditions of crystal mush storage. We then estimate the timescales and cooling rates of the mafic enclaves during their incorporation into the erupted host rhyolite. We apply these techniques to the Cordón Caulle system to test the conceptual model presented in Winslow et al. (2022) that argued the basaltic enclaves, that represent the crystal mush, directly underlie and feed the shallow crystal-poor rhyolite (~3-7 km, ~50-140 MPa, 870-920°C; Castro et al., 2013; Jay et al., 2014, Seropian et al. 2021) that erupted in the 2011-12. Furthermore, they argue that the enclaves represent a mush that has differentiated into rhyolite within a single step at shallow levels. This interpretation is based on interstitial melt chemistry from the rhyolite and enclaves, whole-rock and mineral chemistry from the enclaves, and interlocking grain textures with non-spherical vesicles within the mafic enclaves.

Here we test the vertically connected and shallow basaltic mush model by quantitatively determining the mush storage parameters and crystallization history of the basalt. We present clinopyroxene-liquid barometry (Neave & Putirka, 2017) and Al-in-olivine thermometry (Wan et al., 2008; Coogan et al., 2014) from mush samples to constrain the depth and thermal conditions of different crystallization stages of the basalt and relate them to previously published storage conditions for the rhyolite (Castro et al., 2013; Jay et al., 2014; Seropian et al., 2021) to reconstruct the crustal magma storage conditions underneath Cordón Caulle. The Al-in-olivine thermometer, which uses Al partitioning between spinel inclusions and their olivine hosts (Wan

et al., 2008; Coogan et al., 2014), determines near-liquidus crystallization temperatures for the olivine and spinel pairs to estimate extraction temperatures of the basalt from the mantle. Applying the clinopyroxene-liquid (cpx-liq) barometer of Neave & Putirka (2017) allows us to test the conceptual model of a shallow and spatially contiguous crystal mush. We calculate two different equilibrium pressures, one using the clinopyroxene rim compositions paired with interstitial glass, and the other using clinopyroxene core compositions paired with bulk rock compositions as the complementary liquid. The pressure derived from clinopyroxene rims and cores potentially constrains syn-eruptive processes and mush storage conditions, respectively. Lastly, we assess the interactions between the mafic crystal mush and overlying rhyolite by determining cooling rates of the mafic enclaves using Mg-in-plagioclase geospeedometry (Faak et al., 2014, 2015).

Analytical Methods

Mineral chemistry for thermobarometry and geospeedometry was collected via an electron microprobe (JEOL JXA-8200; JEOL JXA-iHP200F). Detailed methodology for each method is summarized in the supplemental material. For the Mg-in-plagioclase thermometry, we used equation 26 in Faak et al. (2013) and only analyze interlocking pairs of plagioclase and clinopyroxene that imply growth during conditions of high crystallinity (Winslow et al. 2022; Fig. 2.2, 2.3, ESM 2.3). Clinopyroxene acts as an infinite reservoir for Mg to diffuse in and out of plagioclase, and partitioning is only a function of temperature and anorthite (An) content (Faak et al, 2013). We focused on samples that contained plagioclase cores with constant anorthite content touching cores of clinopyroxene to resolve storage temperatures. Plagioclase zoning displays high An cores (~An80) overgrown by intermediate An mantles (~An60) and thin low An rims (~An40) (Fig. 3.1; Winslow et al., 2022, Fig. 2.3d). Low An rims are only present

where plagioclase edges are in contact with surrounding groundmass or melt as opposed to when bordered by phenocryst phases such as clinopyroxene or olivine. When in contact with intergrown phenocrysts, zonation only progresses to core or mantle compositions and does not evolve to lower rim An contents (Fig. 3.1; 2.3). This zoning is characteristic throughout the coarsely-crystalline enclaves from the 2011-12 eruption (Winslow et al., 2022, Fig. 2.3d). We focus on the mafic enclave, PCC-18-15A, due to its abundant exposures of plagioclase cores intergrown with clinopyroxene cores (Fig. 3.1). For the Al-in-olivine thermometry, we use equation 6-7 from Coogan et al. (2014). Prior to trace element analysis, we produced qualitative maps of the olivine to test for elemental zoning surrounding the spinel inclusions (ESM 3.3; Wong et al., 2022). Both thermometers resolve temperatures within ±20°C.

For barometry, we use the cpx-liq barometer from Neave & Putirka (2017) which accounts for the pressure-sensitive exchange of jadeite into clinopyroxene and produces pressure estimates within ±1.4 kbar. This barometer was calibrated using rift zone tholeiites and is suitable for hydrous and anhydrous samples, ultramafic to intermediate compositions, and is ideal for temperatures above 1100°C but can be used at lower temperatures with caution (Neave & Putirka, 2017). Cordón Caulle is consistent with these parameters as a tholeiitic, dry, and highly crystalline volcanic complex (Singer et al., 2008; Castro et al., 2013; Jay et al., 2014; Winslow et al., 2022). A more recent study has addressed additional uncertainties associated with all cpx-liq barometers suggesting errors can be as large as ±3 kbar due to analytical conditions (Wieser et al., 2023). This is specifically in relation to collecting low X-ray counts on lower concentration elements that are essential in barometry calculations, such as Na in clinopyroxene barometers (i.e. cpx-liq barometer from Neave & Putirka (2017); (Wieser et al., 2023). Low Na count times contribute to low analytical precision and propagate error (Wieser et al., 2023). While varying

cpx-only and cpx-liq barometers require careful comparison and usage, we note that our Na count times are at the higher extent with 60 second count times (described in supplemental material). Two scenarios were used to account for differentiation within the samples. The first scenario utilized clinopyroxene rim compositions as the mineral phase and glass data from the interstitial melt as the liquid phase. In this scenario, the evolved rims of the clinopyroxene are in equilibrium with the liquid melt phase and thus report late-stage pressure estimates. The second scenario utilizes clinopyroxene core compositions for the mineral phase and bulk whole rock chemistry as the liquid phase. The mafic enclaves experience negligible fractionation as shown in major and trace element chemistry (Winslow et al., 2022), thus, bulk chemistry can be used as an analog for initial liquid compositions.

Mg-exchange plagioclase-clinopyroxene thermometry

We observe constant concentrations of Mg across the uniform high An plagioclase cores (~500 ppm, <20 ppm Mg internal variation; Fig. 3.1A). At the plagioclase-clinopyroxene interface Mg decreases gradually with interface concentrations being about 200 ppm lower, down to ~300 ppm (Fig. 3.1). We assume plagioclase core interior compositions of Mg may retain mush storage conditions, while plagioclase-clinopyroxene interface Mg compositions reflect magmatic cooling processes that re-equilibrate as the magma differentiates and lowers the Mg contents. Temperature estimates from six plagioclase core interiors using Faak et al. (2013) results in temperatures ranging from ~918-965ºC (±20ºC) (Fig. 3.1B). All profiles record last-equilibration temperatures at the plagioclase-clinopyroxene interface with temperatures of ~795-853ºC (±20ºC) (Fig. 3.1C).

We complement the late-stage thermal history recorded in plagioclase with Al-in-olivine thermometry and cpx-liq barometry to constrain mantle extraction temperatures and depth of

crystallization, respectively. For the Al-in-olivine thermometer, Al concentrations in olivine range from 76-170 ppm. The spinel inclusions range from 3.6-6.4 wt% Al, and range in $Cr\#_{16-57}$ but cluster around $Cr\#_{44-57}$ (calculated on a molar basis, Cr# =(100*Cr/(Cr+Al)); ESM 3.3, 3.4). The Al-in-olivine thermometer records initial crystallization temperatures ranging from 1227-1401ºC (± 20ºC) for olivine hosted spinel pairs (Fig. 3.2). Temperatures dominantly cluster around ~1240-1320ºC and are distinctly hotter compared to the temperatures derived from Mg partitioning between plagioclase and clinopyroxene (Fig. 3.2). For barometry, clinopyroxene rim compositions paired with liquid compositions produce a range of shallow pressures with two clusters of data. The first group produces nominal negative to <30 MPa outputs (Fig. 3.3). These shallow pressure estimates are associated with distinct chemical rim zonation that is thin (<50 μm rim within >1000 μm diameter grains) and represent the final crystallization stage (Fig. 3.3A). The second group within the rim-glass pairs produces pressures ranging from ~10-80 MPa and are associated with thick diffusely zoned rims (~100-150 μm thickness) (Fig. 3.3B). The clinopyroxene core compositions paired with the bulk rock composition as proxy for the liquid produced pressures ranging from ~100-350 MPa (Fig. 3.3). The range of pressures for both scenarios is calculated over a distribution of temperatures from 900-980ºC that reflects storage temperature estimates calculated for basalt using the Mg-in-plagioclase thermometer from this study and rhyolite storage temperatures from previous studies (Fig. 3.1; Castro et al., 2013).

Storage Constraints Discussion: Implications of Temperature and Pressure Estimates

Thermometry and barometry from this study, and prior petrologic results from Winslow et al. (2022), display evidence for a thermally and compositionally zoned magma chamber (melt lens + crystal mush) at Cordón Caulle and provide support for a vertically contiguous mush beneath the crystal-poor rhyolite. We use the clinopyroxene core-bulk rock composition

barometry (~100-350 MPa; Fig. 3.3) and the Mg-in-plagioclase internal core thermometry (918-965ºC; Fig. 3.2) from the crystal-rich mafic enclaves to constrain mush storage conditions, where the barometry constitutes a maximum pressure estimate given that the cores may have formed deeper than mush formation. Because previous studies report rhyolite storage constraints at 870-920ºC and 50-140 MPa (Castro et al., 2013; Jay et al., 2014; Seropian et al., 2021), our new pressure and temperature estimates for the crystal mush suggest a connected storage region of slightly hotter basaltic mush directly underlying the colder crystal-poor rhyolite (Fig. 3.1; 3.3). The nominally negative pressure outputs (<30 MPa) that are calculated from thin evolved rims likely represent final ascent-driven crystallization at shallow conduit levels.

Al-in-olivine thermometry reports significantly hotter temperatures compared to the Mg-in-plagioclase method and may represent extraction temperatures from the mantle (Fig. 3.2). Spinel inclusions are common for primitive magmatic systems and are some of the first phases to crystallize with olivine (Clynne & Borg, 1997; Wan et al., 2008). It is plausible that the hotter temperatures from the Al-in-olivine method retain early crystallization temperatures prior to being incorporated into a shallow mush and thus record a deeper and hotter crystallization stage. Due to the aluminum's trivalent nature and substitution into the tetrahedral site in olivine, Al diffusion is relatively slow and less susceptible to re-equilibration, thus retaining initial crystallization temperatures that are unaltered from storage in the mush (Coogan et al., 2014; Zhukova et al., 2017).

Diffusion Model for Mg-in-plagioclase

The systematically decreasing Mg concentrations observed in the plagioclase Mg zonation near the clinopyroxene interface represents diffusion associated with post-mush cooling histories (Faak et al., 2013). The length scale and shape of the Mg diffusion profile in plagioclase

are a function of the type and rate of cooling once the plagioclase was removed from the long-term storage in the mush and incorporated into cooler conditions in the rhyolite. Here we determine the rate of cooling in this process and under what mechanisms cooling occurred.

Model Setup and Conditions

Cooling rates are calculated using the Mg-in-plagioclase geospeedometer from Faak et al. (2014) which uses the temperature-dependent partitioning and diffusive exchange of Mg between plagioclase and clinopyroxene. Magmatic cooling creates a compositional gradient of Mg within the plagioclase driving Mg diffusion as partitioning between plagioclase and clinopyroxene changes. Underlying our approach are two assumptions. First, equilibrium is maintained at the interface of the two phases during cooling prior to eruption, which we assume because plagioclase and clinopyroxene are in direct contact and are of similar grain sizes (Faak et al. 2014). Second, clinopyroxene acts as an infinite reservoir of Mg. Mg concentrations in clinopyroxene (~8-9 wt%) are several orders of magnitude greater than Mg concentration in plagioclase (~200-500 ppm). A range of Mg diffusion coefficients in plagioclase (D_{Mg}^{Pl}) have been published (Costa et al., 2003; Faak et al., 2013; Van Orman et al., 2014), and there are varying arguments for how to address the relationship of Mg partitioning with changing An contents (see summary in supplemental material; Bindeman, 1998; Faak et al., 2013; Dohmen & Blundy, 2014; Mutch et al., 2022). For this study we primarily default to D_{Mg}^{Pl} experimentally determined by Faak et al. (2013) as it was part of the overall development of this geospeedometer and because our system is tholeiitic and basaltic, which is compositionally similar to the gabbro used in the original study. The primary difference is the amount of water in these magmas, which has yet to be shown to control diffusion in plagioclase. Given that D_{Mg}^{Pl} reported by Faak et al. (2013) is more than one log unit smaller than other published diffusivities,

we also calculate diffusion timescales using D_{Mg}^{Pl} from Costa et al. (2003). Our goal is to present order of magnitude timescales given the uncertainties in the model assumptions, and therefore, we fitted the profiles visually. Silica activity (a_{SiO2}) impacts these equations and is calculated from Eqn. 9 in Faak et al. (2014) where a_{SiO2} is estimated by the olivine-orthopyroxene phase assemblage. Our samples exhibit orthopyroxene overgrowth on olivine phases and as a result, we use Eqn. 9 to estimate a_{SiO2} for our enclaves (Faak et al., 2014; Winslow et al., 2022). We assume isotropic diffusion when modeling Mg within plagioclase. Previous experimental work has discussed negligible anisotropy between b- and c-axes, and that it is acceptable to treat Mg diffusion as isotropic within plagioclase (LaTourette & Wasserburg, 1998; Zellmer et al., 1999; Van Orman et al., 2014). The plagioclase core storage temperature from the Mg-in-plagioclase method is used as the initial temperature, T_{start}, for each individual grain. As cooling affects the plg-cpx interface Mg concentration, we calculate the changing boundary condition as we vary temperature during cooling with the final temperature, T_c, associated with the measured interface Mg concentrations. To find the best fit, we calculate Mg diffusion profiles via a finite difference model for a range of cooling paths. We modeled two different cooling histories: (1) prolonged diffusive equilibration at constant T_c following an instantaneous stepwise cooling from T_{start} to T_c, and (2) diffusive equilibration during linear continuous cooling from T_{start} to T_c.

Cooling Rates and Implications

Instantaneous Cooling Paths

Cooling rates were obtained from five separate plagioclase-clinopyroxene pairs. The instantaneous cooling path produces the best fit shape to match the measured data across all grains and diffusivities (Fig. 3.4). Measured Mg profiles display relatively flat profiles within the core with a steep decrease in Mg near the rim which represents the progression of the diffusion

front (Fig. 3.4). Modeled continuous cooling paths are shown as grey dashed lines in Fig. 3.4 and dispaly more gradual diffusion fronts because higher temperatures are sustained longer, and as a result diffusion advances further into the crystal (Fig. 3.4). The instantaneous cooling models provide a better fit to the shape of the Mg profile than the continuous cooling paths. Using the Faak et al. (2013) diffusivity (D_{Faak}), timescales of storage after instantaneous cooling from T_{start} to T_c range between ~250-4000 yr with the majority at ~1000 yr (Fig. 3.4; Transect 1: ~250 yr, Transect 2: ~1000-1250 yr, Transect 3: ~750-1000 yr, Transect 4: ~4000 yr, Transect 6: ~500-700 yr). If we use the faster diffusivity from Costa et al. (2003) (D_{Costa}), the results shift to ~25-100 yr (Fig. 3.4; Transect 1: ~25 yr, Transect 2: ~75 yr, Transect 3: ~50-100 yr, Transect 4: ~200-300 yr, Transect 6: ~25-50 yr). The magnitude variation in estimates needs to be resolved via continued experimental work on Mg partitioning in plagioclase. This is beyond the scope of this paper.

Using Mg partitioning between plagioclase and clinopyroxene for volcanic mafic rocks is widely applicable for many magmatic systems and volcanic environments, and this study proves that it is a very useful tool if properly constrained. We acknowledge that comparable diffusion coefficients from Costa et al. (2003) and Van Orman et al. (2014) are quicker, and as a result, the Faak-derived estimates are considered a maximum estimate. We primarily follow D_{Faak} because the focus of this work was to use the established and consistent framework of Mg-in-plagioclase thermometry and geospeedometry developed in gabbroic systems (Faak et al., 2013; 2014; 2015), and expand it into crystal-rich basaltic systems that have coexisting plagioclase-clinopyroxene pairs. D_{Faak} was specifically designed for plg-cpx pairs whereas other models address plg-melt (Costa et al., 2003). Additionally, methods developed by Faak et al. (2013; 2014) were applied to similar chemistry and conditions to Cordón Caulle (dry conditions,

gabbroic oceanic ridges). Cordón Caulle is a dryer volcanic complex (~2-4 wt% H_2O; Castro et al., 2013; Jay et al., 2014), is of tholeiitic composition (Singer et al., 2008), and lacks hydrous phases (amphibole); thus, D_{Faak} may be adequate for this system.

The best fit instantaneous cooling path, regardless of diffusivity used, can be explained through rapid incorporation of the mafic enclaves into the cooler overlying rhyolite that subsequently experience prolonged storage prior to eruption based on the calculated timescales. The D_{Faak} timescales suggest enclave incorporation occurred on the order of hundreds to thousands of years prior to the eruption compared to D_{Costa} which suggests enclave incorporation and storage occurred on the order of decades to a century.

While the competing diffusion coefficients produce a level of magnitude difference in timescale estimates, using this data we can infer magmatic processes and further understanding about the longevity and lifetime of the crystal mush at Cordón Caulle. Both cooling rate estimates reveal that mafic enclave incorporation occurred at a minimum of decades prior to the eruption. This suggests the enclaves were not ripped up or incorporated syn-eruptively with the force of the eruption, but that they were already stored within the rhyolite for tens to thousands of years depending on which diffusion coefficient used, assuming our storage temperature estimates are correct (918-965°C). While these temperature estimates are relatively colder compared to typical basalts (1000-1100°C; Dohmen & Chakraborty, 2007), the high levels of crystallinity (up to 70 vol%) support lower temperatures, and the estimates are similar yet still hotter than the overlying rhyolite.

Using D_{Costa} with timescales of decades to a century, we can infer enclave incorporation may have been impacted by the historic Cordón Caulle eruptions which occurred in ~40-yr recurrences intervals at 1921-22, 1960, and 2011-12 (Singer et al. 2008; Castro et al. 2013;

Winslow et al. 2022). Phelps et al. (2023) presents a numerical model of magma chamber dynamics at Cordón Caulle that supports the interpretation that enclave incorporation is impacted by previous eruptions. This model suggests that upon eruption and removal of the crystal-poor rhyolite melt cap, the magma chamber experiences a downward progression of depressurization resulting in the upward extraction of interstitial melt from the crystal-rich mush. This upward extraction partially replenishes the melt lens cap causing post-eruptive inflation observed at the surface. During this process of efficient melt segregation, fragments of the crystal-rich mush may have also been entrained and rapidly incorporated into the newly replenished melt cap. Once incorporated, the enclaves would be stored until a future eruption. The 40-yr recurrence interval in eruptions, and as a result a 40-yr recurrence interval of this replenishment process, is aligned with instantaneous cooling paths and the D_{Costa} cooling rates that propose decades to a century of storage in the rhyolite host magma prior to eruption.

Alternatively, using D_{Faak}, enclave incorporation likely occurred on the timescales of hundreds to thousands of years ago, and the method of enclave entrainment is less well known. One explanation is that their incorporation occurred from the same processes of mush recharge through melt extraction (Phelps et al. 2023), but from prehistoric eruptions of rhyolitic lavas flows and domes that occurred within the last ~6000 years (Singer et al. 2008). Such enclave addition would suggest that they were quasi-instantaneously entrained during a melt cap replenishing event following a Holocene eruption, and then stored and retained for several thousand years. The probability of enclave survival for thousands of years is consistent with a chemical and physical disaggregation model using an advective-diffusive disaggregation process of enclaves in compositionally distinct magmas (Ruprecht et al. 2020). This disaggregation model suggests that enclaves with radii of 5-10 cm, like that observed in the 2011-12 Cordón

Caulle samples, can survive on the order of 1000 years. Furthermore, cooler storage temperatures of the rhyolite (~ 900°C) would only further delay disaggregation and homogenization of enclaves supporting the likelihood of long-term enclave survival.

Continuous Cooling Paths

We examine the continuous cooling path as the least suitable fit for measured data. The continuous cooling paths produce gradual diffusion fronts that progress farther into the grain (Fig. 3.4). This progression results in curved profiles and a decrease in Mg farther into the plagioclase that does not match the flat Mg core data observed in the Cordón Caulle plagioclase. Consequently, a continuous cooling path is less likely for mafic enclaves from the 2011-12 eruption. A continuous cooling path, conceptually, would represent the enclaves experiencing constant cooling for hundreds to thousands of years prior to eruption. Such cooling would exclude incorporation into the cooler rhyolite and that the enclaves experienced minimal thermal contrasts. This model suggests the enclaves remain part of the main crystal mush for its lifetime. It does not explain their incorporation into the erupted and colder rhyolite. An alternative explanation would be if the enclaves represent disaggregated portions of larger enclave fragments hosted within the rhyolite that were thermally buffered in their cores and allowed to continuously cool unperturbed. Using the length-scale diffusion equation, ($x = \sqrt{(Dt)}$), we can estimate the required time to cool the interior of hypothetical larger clusters of enclaves (Kretz, 1994). In this equation, x is the length or radius of the enclave in meters, D is the thermal diffusivity in m^2/s, and t is time in seconds. Cordón Caulle enclaves range in size from ~5-20 cm and occasionally reach ~40 cm in diameter (Winslow et al., 2022). Here we test larger enclave clusters that range from 1-2 m in diameter (0.5-1 m in radius, x) that represent a magnitude increase in size compared to the smaller collected enclaves, and we use the average value for

thermal diffusivity (D) of Earth (~10^{-6} m^2/s; Fagents et al., 2013). Under these parameters, a 1-meter diameter enclave would require ~3 days to fully cool, and a 2-meter diameter enclave requires ~11.5 days to entirely cool. These are relatively instantaneous timescales compared to the previously calculated cooling paths of 75-500 years. It is unlikely that large blocks of enclaves (1-2 m diameter) would thermally sustain the enclave interiors with continuous cooling on the order of 75 years (D_{Costa}) or 500 years (D_{Faak}) as calculated in the cooling paths. Consequently, it is not feasible that the smaller enclaves represent disaggregated fragments of larger enclaves that were thermally buffered in the rhyolite. Large enclave clusters would need to be on the order of hundreds of meters in diameter to produce the modeled cooling paths which is unrealistic in nature. This explanation is also unlikely as we do not observe any evidence for larger clusters or aggregates of enclaves within the lava flows.

Conclusion

The thermal history and evolution of an active crystal mush has been constrained using the temperature-dependent Mg partitioning between plagioclase and clinopyroxene. We apply this method for both thermometry and geospeedometry to highly crystalline volcanic rocks, demonstrating a new use of this technique that may constrain the dynamics of enclave formation and residence in evolved host magmas. This technique proves to be a useful addition for understanding thermal histories especially in systems that exhibit mafic enclaves with high crystallinities as opposed to typical mafic injection-sourced enclaves (Winslow et al., 2022). Additional quantitative constraints were collected to further constrain the magmatic architecture of the crystal-rich mush using thermobarometry. Results of these methods revealed the basaltic enclaves which represent a crystal-rich mush are stored at slightly hotter temperatures than their rhyolite host and slightly deeper pressures than the rhyolite (~ 918-965°C, ~ 100-350 MPa

versus ~870-920C, 50-140 MPa, respectively). Such estimates support the conceptual model of a spatially contiguous crystal mush that is directly underlying a rhyolite melt lens cap. Geospeedometry estimates revealed that mafic enclave incorporation into the rhyolite occurred on the scale of hundreds to thousands of years prior to eruption. This suggests fragments of the crystal mush are not entrained syn-eruptively but stored in the rhyolite for protracted periods. The timescale estimates are a maximum based on the diffusion coefficient from Faak et al. (2013), and if other diffusion coefficients are used (Costa et al. 2003), timescales become a magnitude quicker at decades to a hundred-year range. This study highlights the necessity for further advancement in experimental work on Mg diffusion on plagioclase. It is a significantly useful and widely applicable tool if properly constrained and can be used to better understand many magmatic environments.

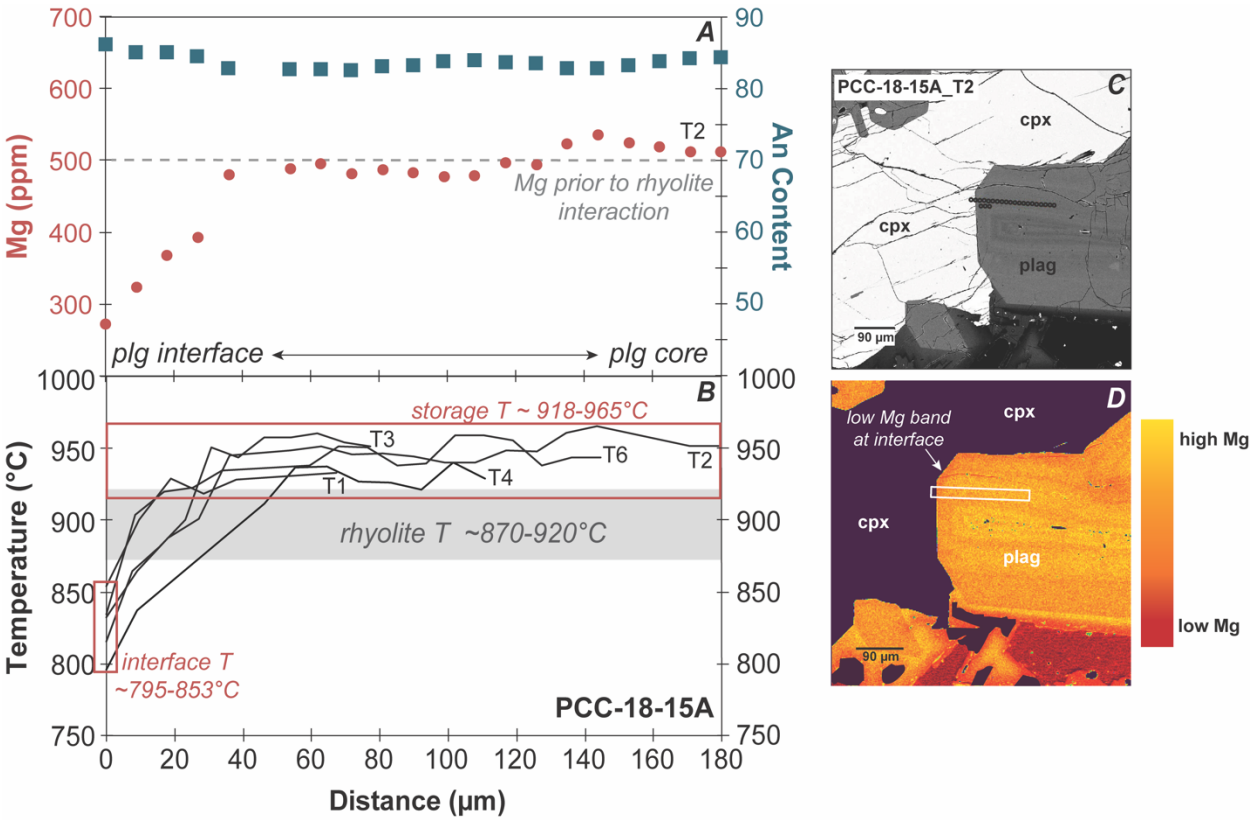

Figure 3.1. (A) Single transect across plagioclase from PCC-18-15A (Transect 2) displaying Mg and An profiles. Mg profile displays gradual decrease in concentration toward plagioclase-clinopyroxene interface. Anorthite profile displays flat concentrations across grain. (B) Compiled temperature transects from samples PCC-18-15A using Faak et al. (2013) thermometer. Transect 2 is visible to directly compare with panel A values. (C) Backscattered electron (BSE) image of plag-cpx pair and location of Transect 2. (D) Relative Mg concentration map for Transect 2 displays visual decrease of Mg from plagioclase core to plagioclase interface.

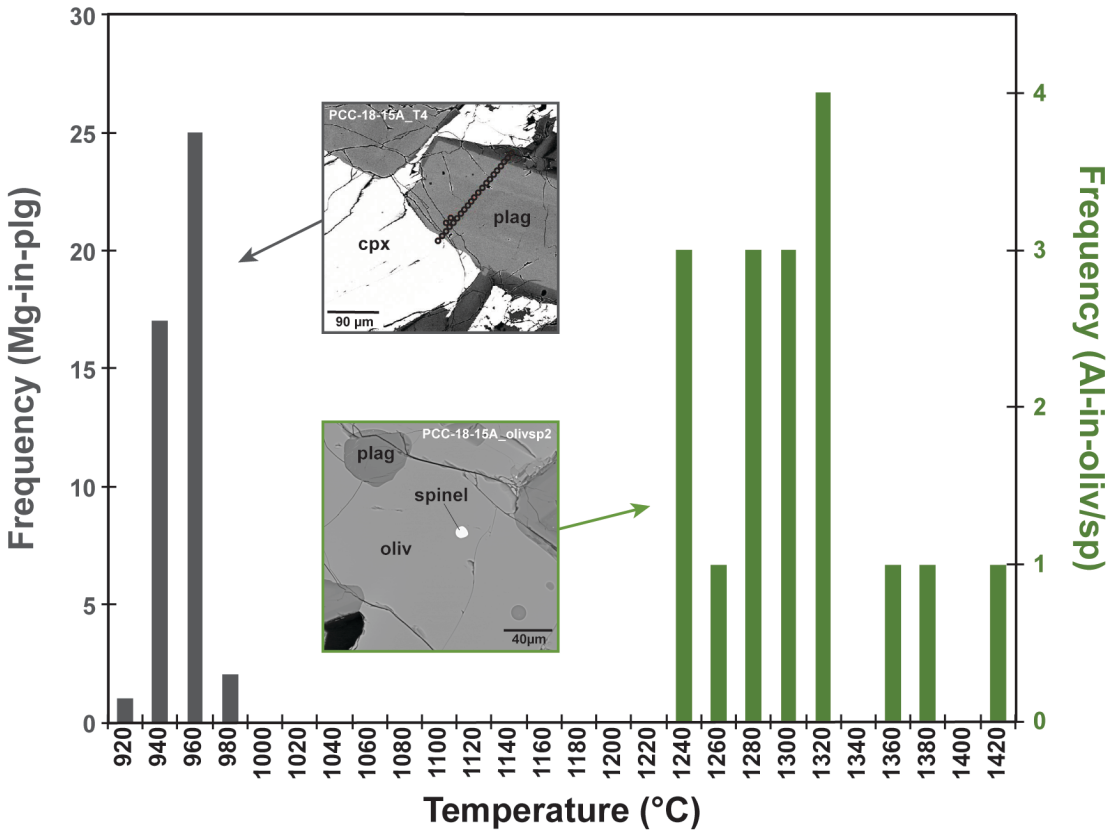

Figure 3.2. Comparison of thermometry estimates. Grey displays Mg-in-plagioclase temperatures and frequency. Green displays Al-in-olivine thermometry and frequency with a hotter temperature range (~1240-1420°C). Insets show BSE images of respective methods.

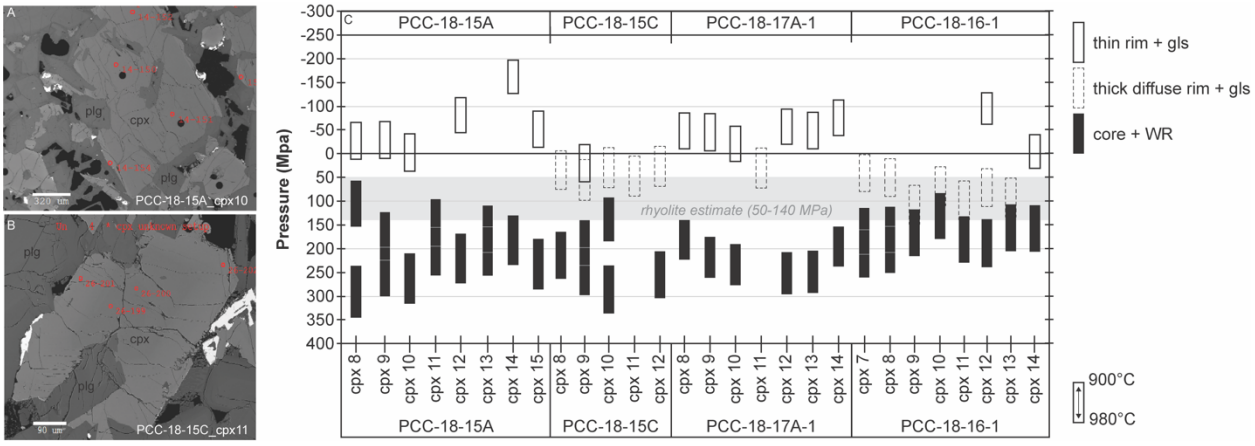

Figure 3.3. (A) BSE image of clinopyroxene from PCC-18-15A (cpx10). Image shows example of thin rim zonation and analytical point at "14-154" with other core analyses within the interior of the grain. (B) BSE image of clinopyroxene from PCC-18-15C (cpx11). Image shows example of thick diffuse rim with analytical point "26-20" with other core analyses within the interior. (C) Cpx-liq barometry across four samples. Individual boxes display range pressures for specific grains across the temperature range, 900-980°C, collected from Mg-in-plg thermometer. Cpx core analyses produce pressures ranging from ~100-350 MPa and overlap with the base of previously determined rhyolite pressures (50-140 MPa). Cpx rim to liquid pairs produce two categories of pressures based on their textures. Thin cpx rims produce nominally shallow pressures <30 MPa, while thick diffuse cpx rims produce shallow pressures of ~10-80 MPa.

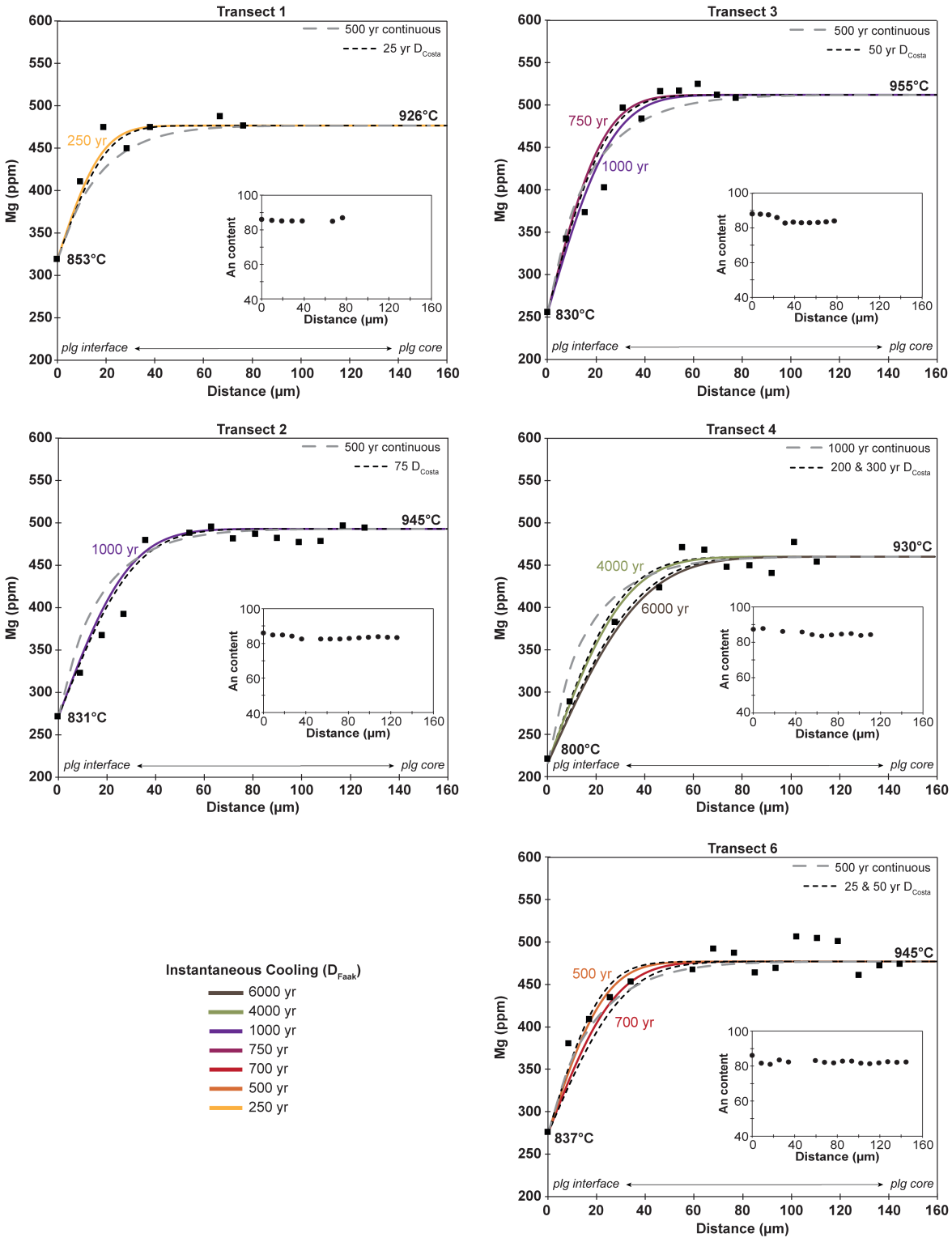

Figure 3.4. Modeled cooling rates for 5 plagioclase-clinopyroxene transects. Colored profiles represent instantaneous cooling paths using D_{Faak}. Light grey dashed line are continuous cooling paths. Black dashed lines are instantaneous cooling paths using the Costa et al. (2003) diffusion coefficient. Black squares are measured Mg concentration data. Inset figures display respective anorthite contents across the modeled transect.

Supplemental Material

Analytical Methods

Mg partitioning between plagioclase and clinopyroxene thermometry

Trace element concentrations of Mg in plagioclase were collected via a JEOL JXA-8200 electron probe microanalyzer equipped with five wavelength dispersive spectrometers and a silicon-drift energy dispersive spectrometer as Washington State University in St. Louis. A mean atomic number background method was used (Donovan et al., 2016), and conditions were run at 15 kV, 100 nA current, and 5 μm beam size. Elements analyzed are as follows: Si (30 s), Ti (180 s), Al (30 s), Cr (30 s), Fe (300 s), Mn (30 s), Mg (315 s), Ca (30 s), Sr (300 s), Ba (180 s), Na (30 s), K (30 s). Five transects were analyzed that ranged in length from ~ 100-180 μm with evenly spaced points at a 5 μm spot size. Transect locations were selected on touching pairs of plagioclase and clinopyroxene with an emphasis on selecting exposures of plagioclase cores of constant anorthite touching clinopyroxene cores to recover storage temperatures. We use Eq. 26 from Faak et al. (2013) to calculate temperatures.

Aluminum partitioning between olivine and spinel thermometry

Analyses were conducted in two sessions at the University of Nevada, Reno using a JEOL JXA-iHP200F electron probe microanalyzer equipped with five wavelength dispersive spectrometers. The first session was dedicated to producing qualitative elemental maps from four samples that contain olivine with spinel inclusions. The maps were used to assess elemental zoning surrounding the spinel inclusion. Qualitative maps were analyzed at 200 nA, 20 kV, and 5 μm step size at 0.5 seconds of dwell time following the methods of Wong et al. (2022). The following elements were mapped in olivine with spinel inclusions: Al, Mg, P, Ni, and Ca.

The second session consisted of quantitative spot analyses on olivine and spinel across the four mapped samples. A mean atomic number background method was used for standardizations (Donovan et al., 2016), and conditions were run at 100 nA, 15 kV, and 1 μm spot size. The following elements were analyzed: Na (40 s), Al (60 s), Si (20 s), Mg (20 s), P (30 s), Ca (60 s), Fe (20 s), Mn (40 s), Ni (50 s), Ti (30 s), Cr (30 s). Olivine spot analyses were taken at a minimum of 10 μm distance from spinel inclusions to account for secondary X-ray fluorescence from the spinel inclusions (Jennings et al., 2019; Wong et al., 2022), and the qualitative maps were used to identify ideal spot locations on the olivine. 23 olivine-spinel pairs were analyzed with single point analyses in the spinel inclusions and three spot analyses in the olivine to create and averaged composition near the inclusion. We calculated temperatures using Eq. 6-7 from Coogan et al. (2014). This thermometer utilizes the temperature-sensitive exchange of Al between spinel inclusions and their olivine host. Al-in-olivine thermometry reports crystallization temperatures of the spinel and olivine phases.

Clinopyroxene – liquid barometry

Major and trace element concentrations of clinopyroxene were collected on four samples also using the JEOL JXA-iHP200F electron probe microanalyzer equipped with five wavelength dispersive spectrometers at the University of Nevada, Reno. A mean atomic number background method was used for standardizations (Donovan et al., 2016), and conditions were run at 50 nA, 15 kV, and 1 μm spot size. The following elements were analyzed: Na (60 s), Al (40 s), Si (30 s), Mg (40 s), Ca (40 s), Fe (40 s), Mn (50 s), Ni (50 s), Cr (60 s), Ti (60 s). Single point core-rim analyses were performed on the clinopyroxene. In addition to newly collected data, previously reported XRF+ICPMS and LA-ICP-MS glass data from Winslow et al. (2022) was utilized for

the barometer. For barometry we used the clinopyroxene-liquid barometer from Neave & Putirka (2017). This barometer uses the pressure-sensitive exchange of jadeite into clinopyroxene and reproduces pressure estimates within ± 1.4 kbars for samples that are ultramafic to mafic in composition. Two scenarios were employed when using the cpx-liq barometer to account for differentiation within the samples and are described in the main text.

Mg Partitioning in Plagioclase

Mg partitioning is major element (anorthite) dependent in plagioclase and many studies have addressed this dependence with inconsistent conclusions (Bindeman, 1998; Faak et al., 2013; Dohmen & Blundy, 2014). Bindeman (1998) reports a negative relationship between the partitioning of Mg (K_D^{Mg}) and An content where the K_D^{Mg} decreases with increasing An content, while Faak et al. (2013) and Dohmen and Blundy (2014) display positive relationships where K_D^{Mg} increases with increasing An content. Mutch et al. (2022) addresses these discrepancies and found that there is a dichotomous nature of Mg partitioning in plagioclase that is significantly impacted by the structural state of the plagioclase (C1 to I1 transition, where albite has C1 symmetry and anorthite has I1 symmetry) and recognized that there is a shift in the K_D^{Mg} behavior (from positive to negative) that occurs at An_{60} (Nemeth et al., 2007; Mutch et al., 2022). While we follow the framework laid out by Faak et al. (2013), our Mg profiles display negative relationships between K_D^{Mg} and An content in conflict with the relationship observed in Faak et al. (2013), yet consistent with results from Bindeman (1998) and parts of Mutch et al. (2022). Although, the high temperature and high An content of Cordón Caulle samples may fall in a transitional stage that aligns with the negative relationship outlined in Mutch et al. (2022), but also correlates to Faak et al. (2013) trends at high temperatures. Regardless, for our study, we

selected profiles across relatively homogenous An cores to alleviate some of this complexity. However, in some cases, individual points of higher or lower An contents were collected in an otherwise homogenous transect and to avoid this complexity, as it is not fully resolved in our field and out of the scope of this paper, we have omitted individual points of differing An contents within a transect and only calculate temperature estimates across the homogeneous An portions of the profile.

ESM 3.1. WUSTL EPMA analyses of plagioclase-clinopyroxene transects for PCC-18-15A.

SAMPLE	Na2O	MgO	Al2O3	SiO2	Cr2O3	MnO	FeO	SrO	K2O	CaO	BaO	TiO2	O	TOTAL
PCC-18-15AT1 10um	1.55	0.07	17.87	21.57	b.d.l.	b.d.l.	0.41	0.09	0.03	11.88	b.d.l.	0.01	45.94	99.41
PCC-18-15AT1 10um	1.30	0.06	18.19	21.26	b.d.l.	b.d.l.	0.41	0.09	0.02	12.27	b.d.l.	0.01	45.93	99.54
PCC-18-15AT1 10um	1.32	0.06	18.16	21.31	b.d.l.	b.d.l.	0.39	0.09	0.03	12.29	b.d.l.	0.01	45.98	99.66
PCC-18-15AT1 10um	1.30	0.06	18.16	21.19	b.d.l.	b.d.l.	0.40	0.09	0.02	12.20	b.d.l.	0.01	45.80	99.24
PCC-18-15AT1 10um	1.31	0.06	18.23	21.18	b.d.l.	b.d.l.	0.41	0.09	0.02	12.28	b.d.l.	0.01	45.89	99.47
PCC-18-15AT1 10um	1.30	0.06	18.19	21.07	b.d.l.	b.d.l.	0.41	0.09	0.02	12.27	b.d.l.	0.01	45.73	99.17
PCC-18-15AT1 10um	1.30	0.06	18.28	21.16	b.d.l.	0.01	0.42	0.10	0.02	12.26	b.d.l.	0.01	45.91	99.51
PCC-18-15AT1 10um	1.30	0.06	18.22	21.17	b.d.l.	b.d.l.	0.43	0.09	0.02	12.25	b.d.l.	0.01	45.86	99.41
PCC-18-15AT1 10um	1.60	0.07	17.93	21.68	b.d.l.	b.d.l.	0.45	0.10	0.03	11.79	b.d.l.	0.01	46.12	99.79
PCC-18-15AT1 10um	1.24	0.06	18.34	21.27	b.d.l.	b.d.l.	0.44	0.09	0.02	12.35	b.d.l.	0.01	46.11	99.94
PCC-18-15AT1 10um	1.47	0.06	18.08	21.71	b.d.l.	b.d.l.	0.44	0.09	0.03	12.01	b.d.l.	0.01	46.31	100.20
PCC-18-15AT1 10um	1.55	0.06	17.96	21.86	b.d.l.	b.d.l.	0.45	0.09	0.03	11.86	b.d.l.	0.01	46.35	100.22
PCC-18-15AT1 10um	1.09	0.04	18.20	21.05	b.d.l.	b.d.l.	0.43	0.09	0.01	12.45	0.01	0.01	45.69	99.06
PCC-18-15AT1 10um	1.23	0.05	18.25	21.45	b.d.l.	b.d.l.	0.46	0.09	0.02	12.37	b.d.l.	0.01	46.23	100.15
PCC-18-15AT1 10um	1.04	0.04	18.46	21.12	b.d.l.	b.d.l.	0.47	0.09	0.02	12.69	b.d.l.	0.01	46.10	100.03
PCC-18-15AT1 10um	1.23	0.05	18.35	21.52	b.d.l.	b.d.l.	0.48	0.09	0.02	12.45	b.d.l.	0.01	46.43	100.62
PCC-18-15AT1 10um	1.22	0.04	18.36	21.67	b.d.l.	b.d.l.	0.50	0.09	0.02	12.43	b.d.l.	0.01	46.61	100.96
PCC-18-15AT1 10um	1.20	0.04	18.42	21.67	b.d.l.	b.d.l.	0.51	0.09	0.02	12.48	b.d.l.	0.01	46.67	101.11
PCC-18-15AT1 10um	1.15	0.03	18.52	21.61	b.d.l.	b.d.l.	0.55	0.10	0.02	12.50	b.d.l.	0.01	46.69	101.17
PCC-18-15AT2 10um	1.34	0.05	18.32	22.02	b.d.l.	0.01	0.48	0.09	0.02	12.19	b.d.l.	0.01	46.92	101.45
PCC-18-15AT2 10um	1.39	0.05	18.26	22.02	b.d.l.	0.01	0.49	0.09	0.03	12.13	b.d.l.	0.01	46.87	101.35
PCC-18-15AT2 10um	1.43	0.05	18.22	22.05	b.d.l.	b.d.l.	0.48	0.09	0.02	12.07	b.d.l.	0.01	46.85	101.28
PCC-18-15AT2 10um	1.44	0.05	18.27	21.87	b.d.l.	b.d.l.	0.49	0.09	0.02	12.10	0.01	0.02	46.70	101.04
PCC-18-15AT2 10um	1.37	0.05	18.27	21.91	b.d.l.	b.d.l.	0.48	0.09	0.02	12.19	0.01	0.01	46.76	101.17
PCC-18-15AT2 10um	1.37	0.05	18.28	21.81	b.d.l.	b.d.l.	0.48	0.09	0.02	12.26	b.d.l.	0.01	46.68	101.06
PCC-18-15AT2 10um	1.34	0.05	18.26	21.74	b.d.l.	b.d.l.	0.49	0.09	0.02	12.27	b.d.l.	0.01	46.58	100.84
PCC-18-15AT2 10um	1.35	0.05	18.31	21.86	b.d.l.	b.d.l.	0.48	0.09	0.02	12.21	0.01	0.01	46.74	101.13
PCC-18-15AT2 10um	1.40	0.05	18.18	21.85	b.d.l.	b.d.l.	0.48	0.09	0.02	12.18	b.d.l.	0.01	46.60	100.83
PCC-18-15AT2 10um	1.41	0.05	18.21	21.97	b.d.l.	b.d.l.	0.48	0.09	0.03	12.13	0.01	0.01	46.76	101.15
PCC-18-15AT2 10um	1.46	0.05	18.12	21.93	b.d.l.	b.d.l.	0.49	0.08	0.02	12.10	b.d.l.	0.01	46.63	100.89
PCC-18-15AT2 10um	1.45	0.05	18.10	22.01	b.d.l.	b.d.l.	0.50	0.09	0.03	12.10	b.d.l.	0.01	46.72	101.05
PCC-18-15AT2 10um	1.45	0.05	18.11	21.82	b.d.l.	b.d.l.	0.50	0.09	0.02	12.10	b.d.l.	0.01	46.51	100.66
PCC-18-15AT2 10um	1.44	0.05	18.05	21.62	b.d.l.	b.d.l.	0.51	0.09	0.02	12.11	b.d.l.	0.01	46.23	100.14
PCC-18-15AT2 10um	1.26	0.04	18.30	21.34	b.d.l.	b.d.l.	0.53	0.10	0.02	12.41	b.d.l.	0.01	46.19	100.21
PCC-18-15AT2 10um	1.16	0.03	18.44	21.09	b.d.l.	0.01	0.57	0.10	0.02	12.55	b.d.l.	0.01	46.05	100.01
PCC-18-15AT3 10um	1.01	0.04	18.60	20.81	b.d.l.	b.d.l.	0.47	0.09	0.02	12.78	b.d.l.	0.01	45.90	99.73
PCC-18-15AT3 10um	1.51	0.06	18.07	21.42	b.d.l.	b.d.l.	0.48	0.09	0.03	11.95	b.d.l.	0.01	45.98	99.59
PCC-18-15AT3 10um	1.77	0.06	17.80	21.92	b.d.l.	b.d.l.	0.48	0.10	0.04	11.55	b.d.l.	0.02	46.24	99.97
PCC-18-15AT3 10um	1.63	0.06	17.88	21.73	b.d.l.	b.d.l.	0.46	0.10	0.03	11.77	b.d.l.	0.01	46.14	99.82
PCC-18-15AT3 10um	1.48	0.06	18.04	21.49	b.d.l.	b.d.l.	0.46	0.10	0.03	12.07	b.d.l.	0.01	46.06	99.80
PCC-18-15AT3 10um	1.49	0.06	18.05	21.64	b.d.l.	b.d.l.	0.46	0.09	0.03	11.99	b.d.l.	0.01	46.22	100.03
PCC-18-15AT3 10um	1.47	0.06	18.08	21.67	b.d.l.	b.d.l.	0.45	0.10	0.02	12.06	b.d.l.	0.01	46.29	100.20
PCC-18-15AT3 10um	1.58	0.06	17.92	21.90	b.d.l.	b.d.l.	0.45	0.09	0.03	11.88	b.d.l.	0.01	46.38	100.30
PCC-18-15AT3 10um	1.67	0.06	17.74	22.21	b.d.l.	b.d.l.	0.46	0.10	0.03	11.66	b.d.l.	0.02	46.53	100.47
PCC-18-15AT3 10um	1.53	0.06	17.92	22.01	b.d.l.	b.d.l.	0.45	0.09	0.03	11.93	b.d.l.	0.01	46.51	100.55
PCC-18-15AT3 10um	1.33	0.05	18.15	21.69	b.d.l.	b.d.l.	0.45	0.09	0.02	12.24	0.01	0.01	46.39	100.42
PCC-18-15AT3 10um	1.37	0.05	18.13	21.65	b.d.l.	b.d.l.	0.45	0.09	0.02	12.22	b.d.l.	0.01	46.33	100.30
PCC-18-15AT3 10um	1.40	0.05	18.05	21.69	b.d.l.	b.d.l.	0.46	0.09	0.02	12.15	b.d.l.	0.01	46.31	100.25
PCC-18-15AT3 10um	1.41	0.05	18.13	21.60	b.d.l.	b.d.l.	0.46	0.09	0.02	12.16	0.01	0.01	46.27	100.21
PCC-18-15AT3 10um	1.42	0.05	18.06	21.56	b.d.l.	b.d.l.	0.47	0.09	0.03	12.12	b.d.l.	0.01	46.17	100.00
PCC-18-15AT3 10um	1.03	0.04	18.53	21.02	b.d.l.	b.d.l.	0.48	0.09	0.02	12.75	0.01	0.01	46.07	100.05
PCC-18-15AT3 10um	1.00	0.03	18.60	20.82	b.d.l.	b.d.l.	0.49	0.09	0.02	12.83	b.d.l.	0.01	45.92	99.82
PCC-18-15AT4 10um	3.78	0.04	15.41	24.52	b.d.l.	b.d.l.	0.60	0.12	0.18	8.05	0.01	0.03	46.46	99.22
PCC-18-15AT4 10um	1.94	0.04	17.49	21.96	b.d.l.	b.d.l.	0.54	0.11	0.06	11.18	0.01	0.02	45.95	99.31
PCC-18-15AT4 10um	1.04	0.03	18.55	20.70	b.d.l.	b.d.l.	0.51	0.10	0.01	12.71	b.d.l.	0.01	45.72	99.40
PCC-18-15AT4 10um	0.99	0.03	18.58	20.70	b.d.l.	b.d.l.	0.48	0.09	0.02	12.86	b.d.l.	0.01	45.78	99.56
PCC-18-15AT4 10um	1.05	0.04	18.52	20.77	b.d.l.	b.d.l.	0.49	0.09	0.02	12.72	b.d.l.	0.01	45.78	99.49
PCC-18-15AT4 10um	0.93	0.04	18.65	20.68	b.d.l.	b.d.l.	0.49	0.09	0.02	12.88	b.d.l.	0.01	45.80	99.58
PCC-18-15AT4 10um	0.91	0.04	18.63	20.72	b.d.l.	b.d.l.	0.50	0.09	0.02	12.94	b.d.l.	0.01	45.86	99.72
PCC-18-15AT4 10um	1.31	0.05	18.16	21.39	b.d.l.	b.d.l.	0.50	0.09	0.03	12.27	b.d.l.	0.01	46.08	99.88
PCC-18-15AT4 10um	1.34	0.05	18.08	21.40	b.d.l.	b.d.l.	0.50	0.09	0.03	12.18	b.d.l.	0.01	45.99	99.66
PCC-18-15AT4 10um	1.26	0.04	18.18	21.29	b.d.l.	b.d.l.	0.49	0.09	0.02	12.42	b.d.l.	0.01	46.02	99.83
PCC-18-15AT4 10um	1.28	0.04	18.17	21.38	b.d.l.	b.d.l.	0.49	0.10	0.02	12.30	b.d.l.	0.01	46.07	99.86
PCC-18-15AT4 10um	1.31	0.04	18.09	21.30	0.01	b.d.l.	0.49	0.09	0.02	12.21	b.d.l.	0.01	45.89	99.46
PCC-18-15AT4 10um	1.38	0.05	18.15	21.54	b.d.l.	b.d.l.	0.50	0.09	0.02	12.25	b.d.l.	0.01	46.25	100.23
PCC-18-15AT4 10um	1.31	0.05	18.22	21.49	b.d.l.	b.d.l.	0.52	0.09	0.02	12.27	b.d.l.	0.01	46.25	100.23
PCC-18-15AT4 10um	1.19	0.04	18.36	21.32	b.d.l.	0.01	0.52	0.09	0.02	12.49	b.d.l.	0.01	46.23	100.27
PCC-18-15AT4 10um	0.99	0.03	18.61	20.99	b.d.l.	b.d.l.	0.50	0.09	0.02	12.81	b.d.l.	0.01	46.11	100.15
PCC-18-15AT4 10um	1.01	0.03	18.60	20.86	b.d.l.	b.d.l.	0.51	0.09	0.02	12.81	b.d.l.	0.01	45.97	99.91
PCC-18-15AT6 10um	1.44	0.03	18.15	21.30	b.d.l.	0.01	0.51	0.09	0.03	12.06	b.d.l.	0.01	45.93	99.58
PCC-18-15AT6 10um	1.35	0.04	18.12	21.27	b.d.l.	0.01	0.52	0.10	0.03	12.16	b.d.l.	0.01	45.87	99.46
PCC-18-15AT6 10um	1.49	0.05	18.08	21.47	b.d.l.	b.d.l.	0.50	0.09	0.03	11.99	b.d.l.	0.01	46.05	99.76
PCC-18-15AT6 10um	1.46	0.05	18.10	21.38	b.d.l.	b.d.l.	0.48	0.09	0.03	11.99	b.d.l.	0.01	45.95	99.54
PCC-18-15AT6 10um	1.48	0.05	18.04	21.28	b.d.l.	b.d.l.	0.48	0.09	0.03	11.96	b.d.l.	0.01	45.78	99.21
PCC-18-15AT6 10um	1.46	0.05	18.07	21.28	b.d.l.	b.d.l.	0.48	0.09	0.02	12.06	b.d.l.	0.01	45.83	99.33
PCC-18-15AT6 10um	1.50	0.05	17.96	21.22	b.d.l.	b.d.l.	0.51	0.10	0.02	11.96	b.d.l.	0.02	45.65	98.96
PCC-18-15AT6 10um	1.55	0.05	17.94	21.23	b.d.l.	0.01	0.50	0.09	0.03	11.88	0.01	0.01	45.64	98.94
PCC-18-15AT6 10um	1.52	0.05	17.90	21.35	b.d.l.	b.d.l.	0.52	0.10	0.03	11.94	b.d.l.	0.01	45.76	99.18
PCC-18-15AT6 10um	1.41	0.05	18.08	21.28	b.d.l.	b.d.l.	0.52	0.10	0.03	12.08	b.d.l.	0.01	45.85	99.40
PCC-18-15AT6 10um	1.42	0.05	18.06	21.35	b.d.l.	b.d.l.	0.51	0.09	0.03	12.08	0.01	0.01	45.91	99.52
PCC-18-15AT6 10um	1.51	0.05	17.99	21.47	b.d.l.	b.d.l.	0.51	0.09	0.03	12.04	0.01	0.02	46.00	99.69
PCC-18-15AT6 10um	1.48	0.05	18.06	21.46	b.d.l.	b.d.l.	0.52	0.09	0.03	12.02	b.d.l.	0.01	46.04	99.76
PCC-18-15AT6 10um	1.39	0.05	18.11	21.37	b.d.l.	b.d.l.	0.51	0.09	0.02	12.13	b.d.l.	0.01	45.99	99.68
PCC-18-15AT6 10um	0.96	0.03	18.49	20.73	b.d.l.	b.d.l.	0.50	0.09	0.01	12.81	b.d.l.	0.01	45.69	99.32
PCC-18-15AT6 10um	1.47	0.05	17.97	21.36	b.d.l.	b.d.l.	0.52	0.10	0.03	12.08	b.d.l.	0.01	45.86	99.43
PCC-18-15AT6 10um	1.57	0.04	17.79	21.44	b.d.l.	b.d.l.	0.54	0.10	0.03	11.81	b.d.l.	0.01	45.73	99.06
PCC-18-15AT6 10um	1.15	0.03	18.33	20.85	b.d.l.	b.d.l.	0.58	0.10	0.02	12.59	b.d.l.	0.02	45.70	99.35

SAMPLE	Na2O	MgO	Al2O3	SiO2	Cr2O3	MnO	FeO	SrO	K2O	CaO	BaO	TiO2	O	TOTAL
PCC-18-15AT1 additional 6	1.15	0.06	18.50	21.08	b.d.l.	b.d.l.	0.41	0.09	0.02	12.54	b.d.l.	0.01	46.06	99.92
PCC-18-15AT1 additional 6	1.38	0.07	18.29	21.36	b.d.l.	b.d.l.	0.41	0.09	0.02	12.24	b.d.l.	0.01	46.15	100.02
PCC-18-15AT1 additional 6	1.47	0.07	18.17	21.47	b.d.l.	b.d.l.	0.45	0.09	0.03	12.01	b.d.l.	0.01	46.13	99.90
PCC-18-15AT1 additional 6	1.07	0.05	18.61	21.05	b.d.l.	b.d.l.	0.45	0.09	0.02	12.66	0.01	0.01	46.15	100.16
PCC-18-15AT1 additional 6	0.93	0.04	18.74	20.82	b.d.l.	b.d.l.	0.46	0.09	0.01	12.88	b.d.l.	0.01	46.04	100.01
PCC-18-15AT1 additional 6	1.23	0.05	18.40	21.26	b.d.l.	b.d.l.	0.48	0.09	0.02	12.44	0.01	0.01	46.18	100.18
PCC-18-15AT2 additional 3	1.22	0.04	18.43	21.30	b.d.l.	b.d.l.	0.48	0.09	0.03	12.47	b.d.l.	0.01	46.26	100.33
PCC-18-15AT2 additional 3	1.30	0.04	18.32	21.41	b.d.l.	b.d.l.	0.51	0.09	0.02	12.33	b.d.l.	0.01	46.26	100.30
PCC-18-15AT2 additional 3	1.25	0.03	18.35	21.38	b.d.l.	b.d.l.	0.54	0.09	0.02	12.46	b.d.l.	0.01	46.30	100.43
PCC-18-15AT3 additional 3	1.42	0.05	18.14	21.69	b.d.l.	b.d.l.	0.47	0.09	0.02	12.19	0.01	0.01	46.41	100.49
PCC-18-15AT3 additional 3	1.39	0.05	18.16	21.66	b.d.l.	0.01	0.48	0.09	0.03	12.22	0.01	0.02	46.40	100.50
PCC-18-15AT3 additional 3	1.17	0.04	18.41	21.31	b.d.l.	b.d.l.	0.48	0.09	0.02	12.58	0.01	0.01	46.28	100.40
PCC-18-15AT4 additional 2	1.16	0.04	18.41	21.22	b.d.l.	b.d.l.	0.52	0.09	0.02	12.59	0.01	0.01	46.19	100.25
PCC-18-15AT4 additional 2	1.02	0.03	18.58	21.05	b.d.l.	b.d.l.	0.50	0.10	0.02	12.76	b.d.l.	0.01	46.14	100.20
PCC-18-15AT6 additional 3	1.09	0.04	18.48	20.91	0.01	b.d.l.	0.51	0.09	0.02	12.66	b.d.l.	0.01	45.89	99.71
PCC-18-15AT6 additional 3	1.37	0.04	18.24	21.46	b.d.l.	b.d.l.	0.53	0.10	0.03	12.24	0.01	0.01	46.25	100.29
PCC-18-15AT6 additional 3	1.53	0.04	17.89	21.41	b.d.l.	0.01	0.55	0.10	0.03	11.95	b.d.l.	0.01	45.83	99.35

ESM 3.2. BSE images of plagioclase-clinopyroxene transect locations for transects 1, 2,3,4, 6.

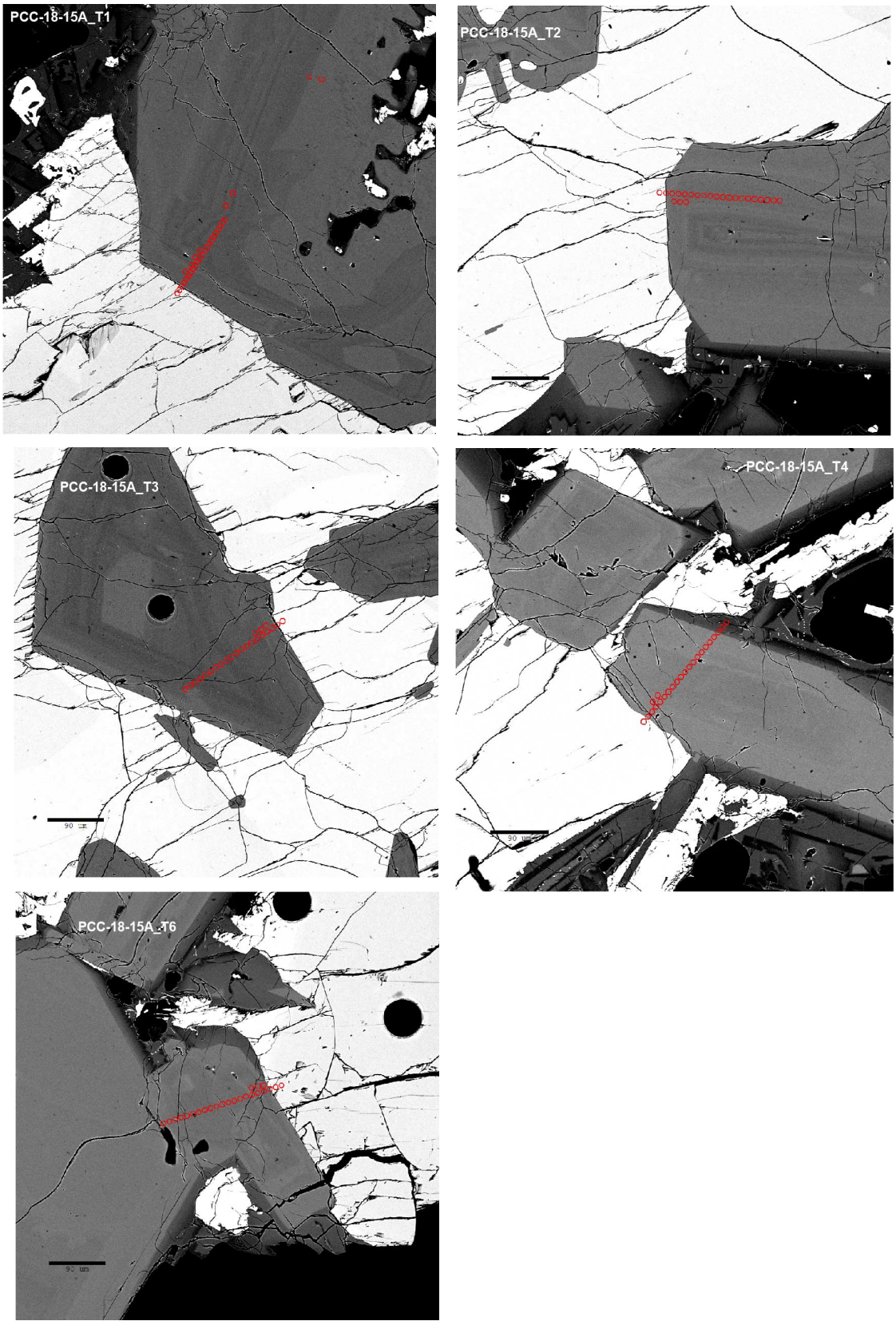

ESM 3.3. Select qualitative maps of spinel inclusions hosted within olivine. All maps are 250 µm by 250 µm.

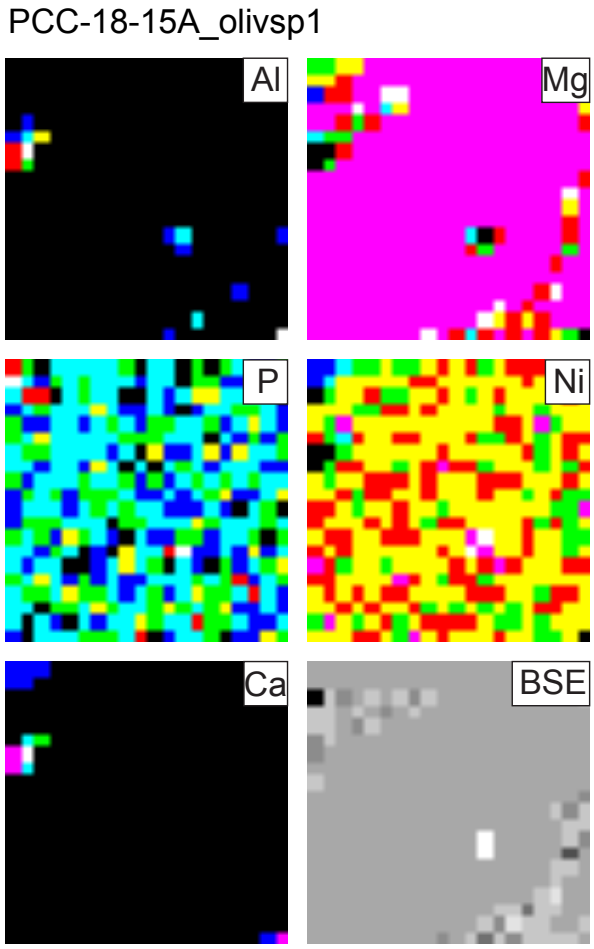

PCC-18-15A_olivsp4

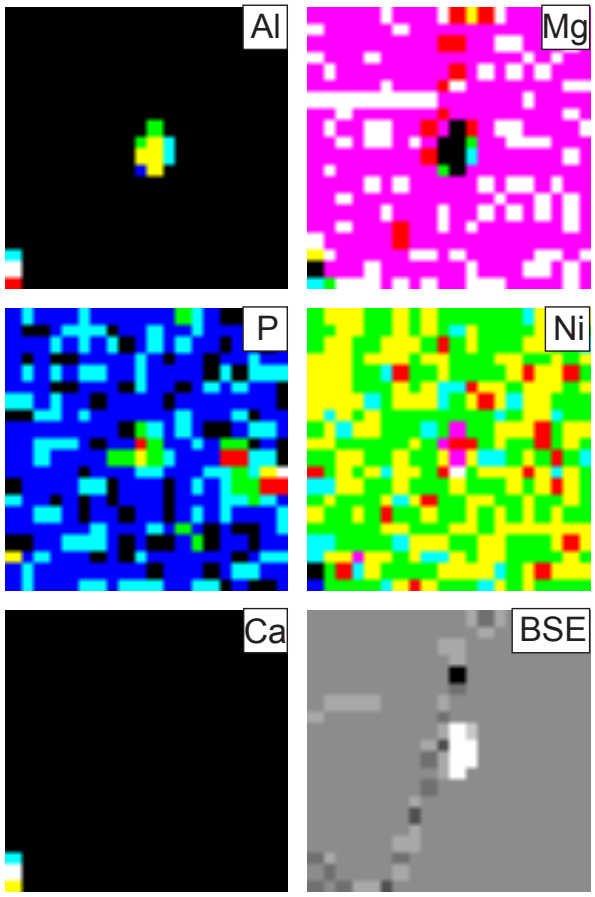

PCC-18-15A_olivsp6

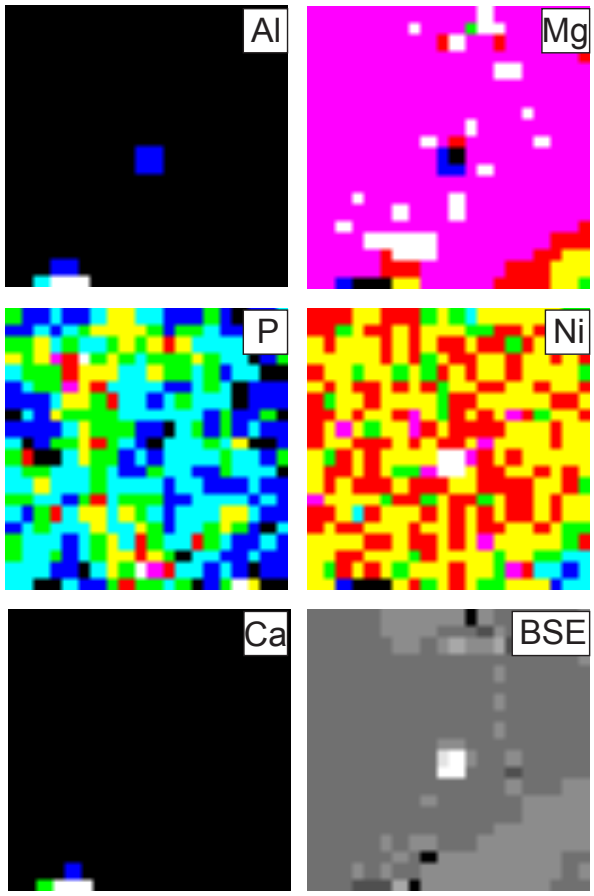

PCC-18-15A_olivsp7

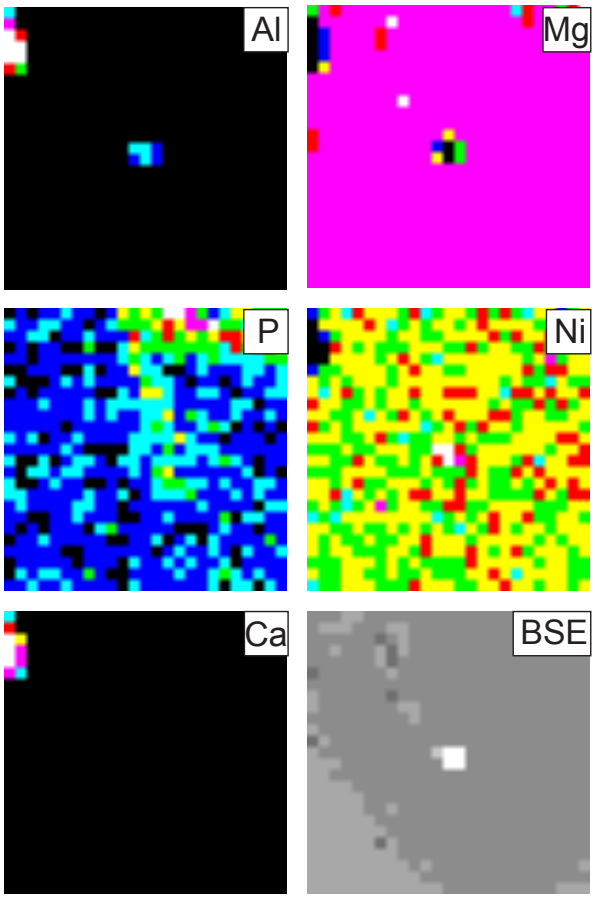

PCC-18-15C_olivsp1

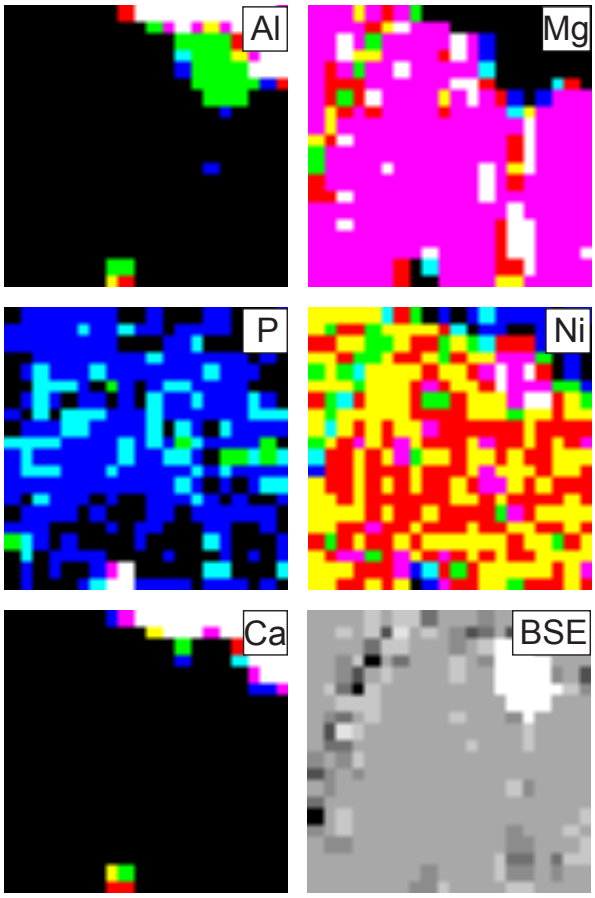

PCC-18-15C_olivsp2

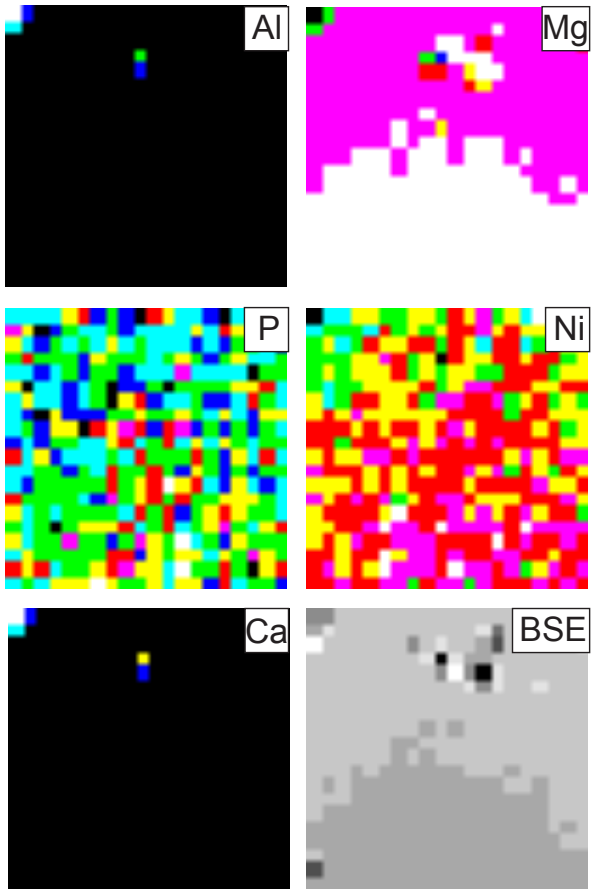

PCC-18-15C_olivsp5

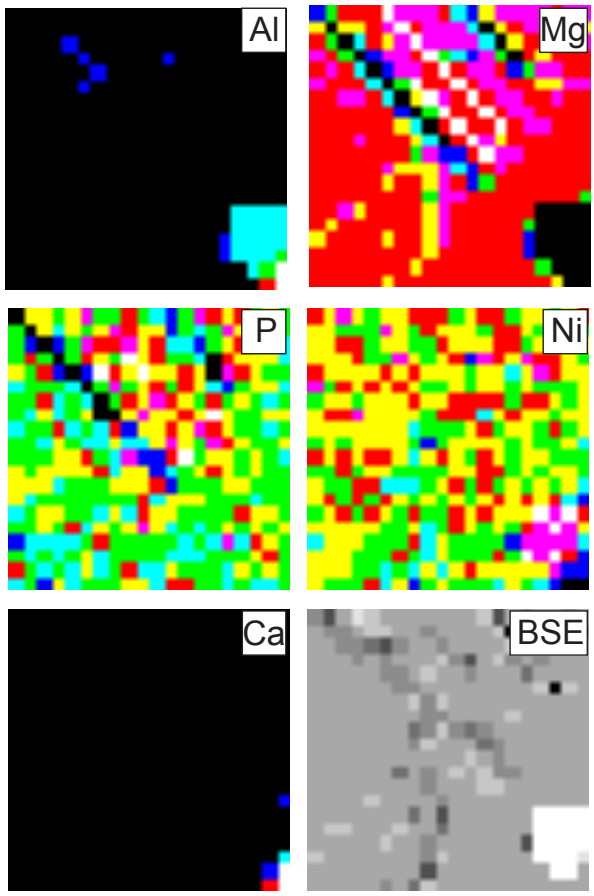

PCC-18-17A-1_olivsp1

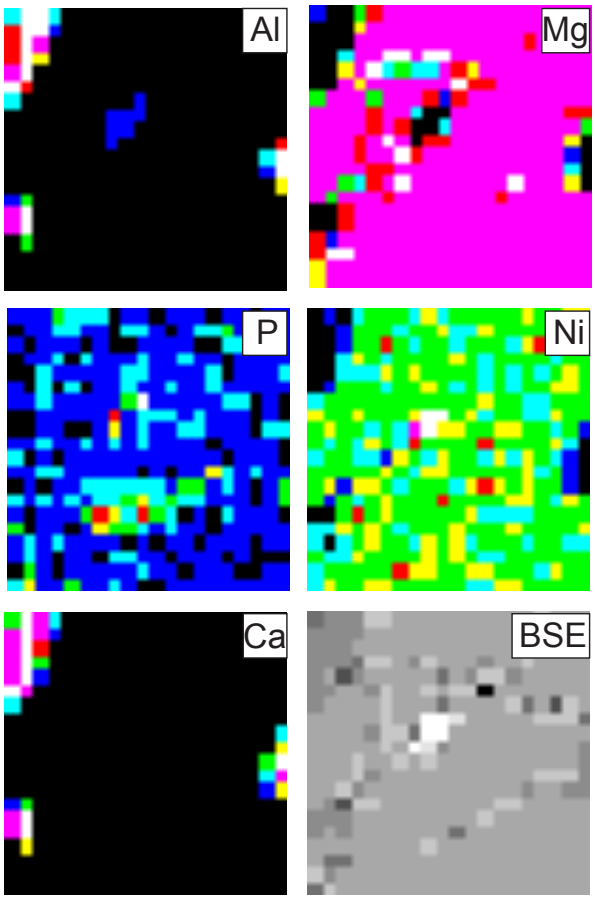

PCC-18-17A-1_olivsp4

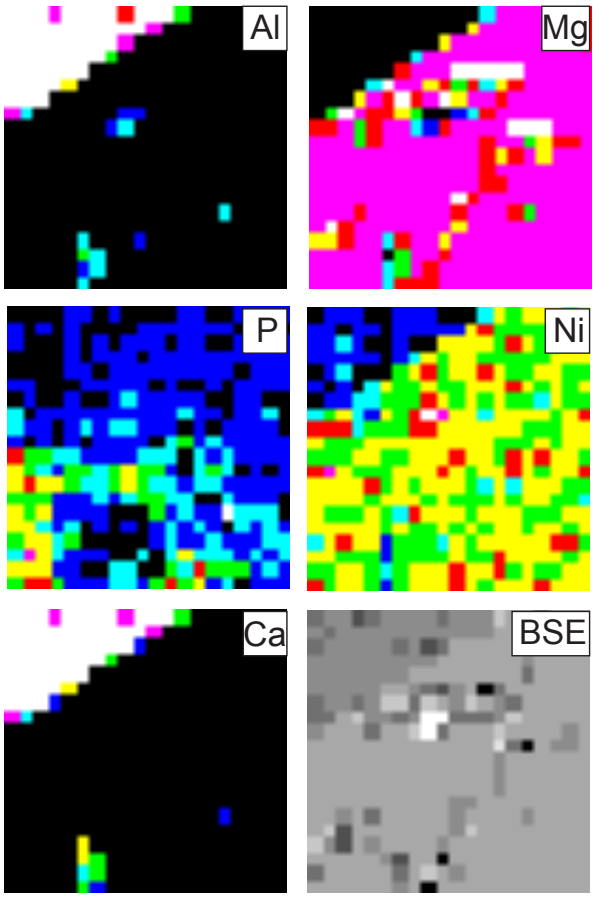

PCC-18-17A-1_olivsp5

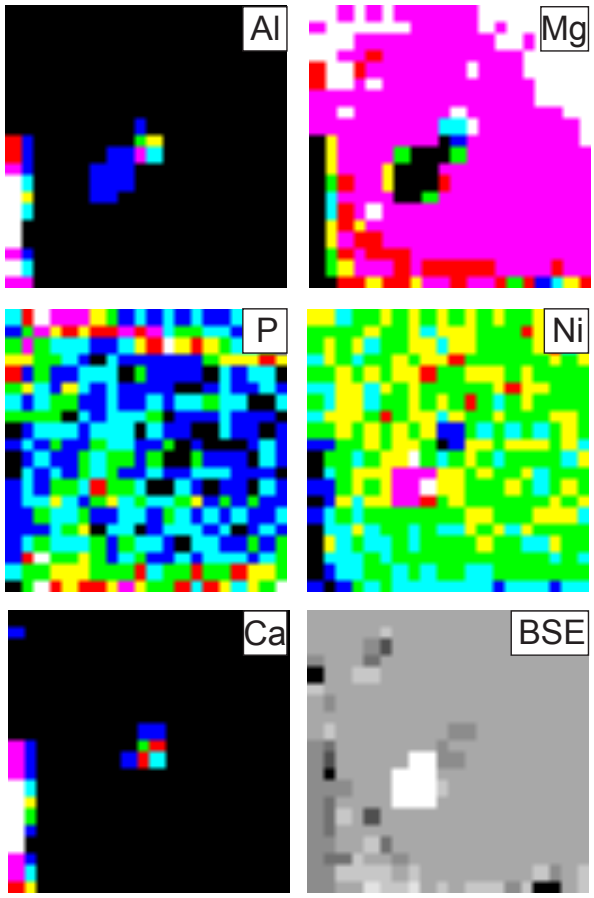

PCC-18-17A-1_olivsp7

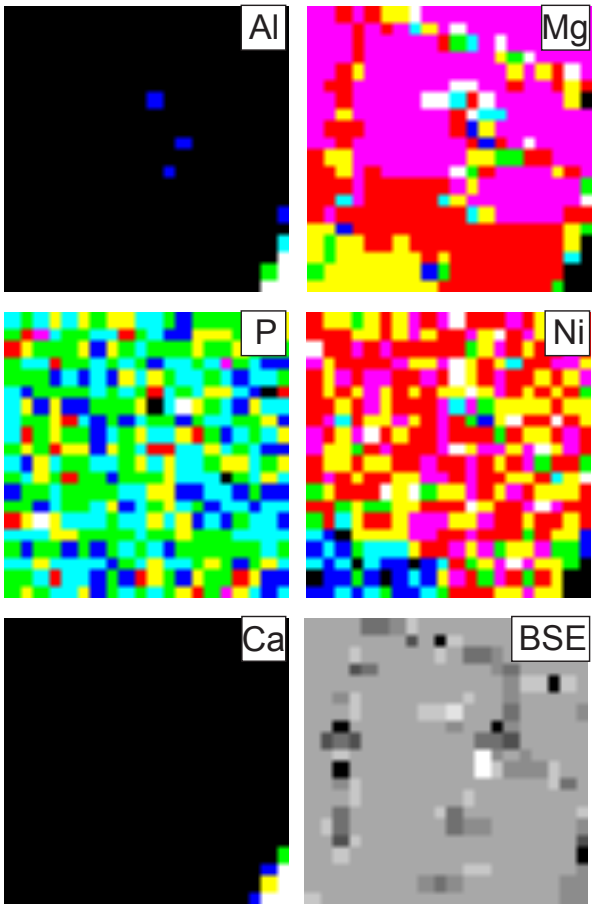

PCC-18-17A-1_olivsp11

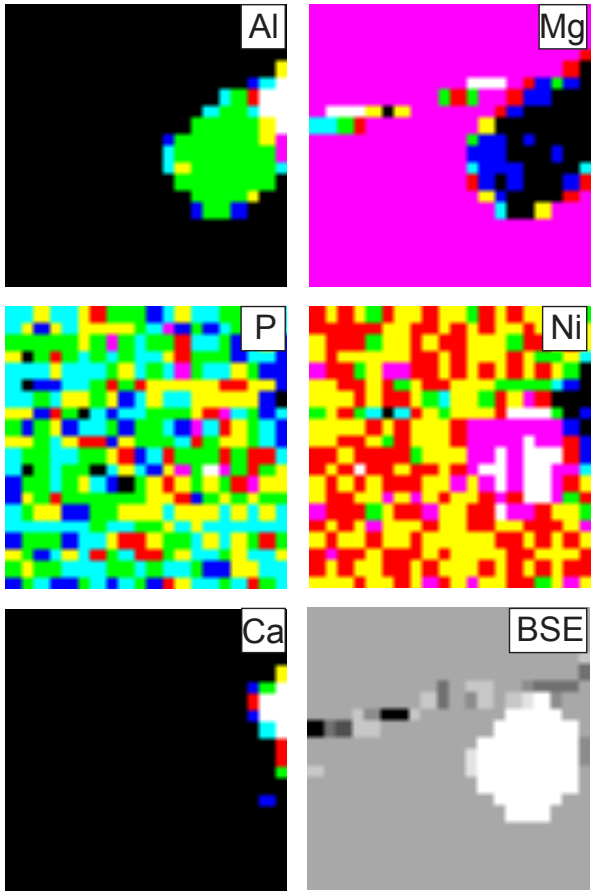

ESM 3.4. UNR EPMA analyses of olivine grains with spinel inclusions.

SAMPLE	SiO2	TiO2	Al2O3	Cr2O3	FeO	NiO	MnO	MgO	CaO	Na2O	P2O5	O	TOTAL
PCC-18-15A_olivsp1_oliv	38.31	b.d.l.	0.02	b.d.l.	23.49	0.08	0.40	37.11	0.16	0.01	b.d.l.	b.d.l.	99.59
PCC-18-15A_olivsp1_oliv	38.26	b.d.l.	0.02	0.01	23.50	0.08	0.40	37.13	0.17	b.d.l.	b.d.l.	b.d.l.	99.57
PCC-18-15A_olivsp1_oliv	38.20	b.d.l.	0.02	0.01	23.50	0.08	0.41	37.22	0.17	0.00	b.d.l.	b.d.l.	99.61
PCC-18-15A_olivsp2_oliv	38.42	b.d.l.	0.02	0.01	22.87	0.08	0.39	37.93	0.17	b.d.l.	0.01	b.d.l.	99.90
PCC-18-15A_olivsp2_oliv	38.44	b.d.l.	0.01	b.d.l.	22.91	0.08	0.40	37.82	0.17	0.00	0.01	0.00	99.85
PCC-18-15A_olivsp2_oliv	38.38	b.d.l.	0.02	b.d.l.	22.87	0.07	0.38	37.95	0.16	b.d.l.	0.02	b.d.l.	99.88
PCC-18-15A_olivsp3_oliv	38.53	0.01	0.02	b.d.l.	23.25	0.08	0.41	37.82	0.20	0.00	0.01	b.d.l.	100.34
PCC-18-15A_olivsp3_oliv	38.35	b.d.l.	0.02	0.01	23.11	0.08	0.40	37.74	0.17	0.00	b.d.l.	0.00	99.89
PCC-18-15A_olivsp3_oliv	38.35	0.02	0.02	0.01	23.76	0.07	0.40	37.16	0.18	0.00	b.d.l.	b.d.l.	99.98
PCC-18-15A_olivsp4_oliv	38.53	b.d.l.	0.02	b.d.l.	22.85	0.08	0.38	38.06	0.16	b.d.l.	b.d.l.	0.00	100.09
PCC-18-15A_olivsp4_oliv	38.45	b.d.l.	0.02	0.01	22.58	0.08	0.39	38.00	0.16	b.d.l.	b.d.l.	b.d.l.	99.71
PCC-18-15A_olivsp4_oliv	38.47	0.01	0.02	0.01	22.74	0.07	0.39	38.06	0.16	0.01	0.08	b.d.l.	100.03
PCC-18-15A_olivsp5_oliv	38.08	b.d.l.	0.02	b.d.l.	22.65	0.07	0.40	37.99	0.18	b.d.l.	b.d.l.	b.d.l.	99.41
PCC-18-15A_olivsp5_oliv	38.19	0.01	0.02	0.01	22.67	0.08	0.39	38.10	0.17	0.00	b.d.l.	b.d.l.	99.64
PCC-18-15A_olivsp5_oliv	38.22	b.d.l.	0.02	0.01	22.61	0.08	0.38	38.02	0.16	0.00	b.d.l.	0.00	99.51
PCC-18-15A_olivsp6_oliv	38.37	0.01	0.03	0.04	22.92	0.08	0.40	37.90	0.17	0.00	0.06	0.00	99.99
PCC-18-15A_olivsp6_oliv	38.37	0.01	0.03	0.03	23.38	0.07	0.40	37.57	0.17	0.01	0.07	b.d.l.	100.09
PCC-18-15A_olivsp6_oliv	38.44	0.02	0.03	0.03	23.54	0.08	0.42	37.38	0.17	0.00	0.04	b.d.l.	100.14
PCC-18-15A_olivsp7_oliv	38.33	0.01	0.02	b.d.l.	23.62	0.07	0.42	37.40	0.16	0.00	b.d.l.	0.00	100.03
PCC-18-15A_olivsp7_oliv	38.37	0.01	0.02	b.d.l.	23.36	0.07	0.41	37.56	0.16	0.00	b.d.l.	0.00	99.98
PCC-18-15A_olivsp7_oliv	38.44	b.d.l.	0.02	b.d.l.	22.98	0.07	0.39	37.97	0.17	b.d.l.	0.01	b.d.l.	100.06
PCC-18-15A_olivsp8_oliv	38.49	0.01	0.02	b.d.l.	22.84	0.08	0.38	38.00	0.17	0.01	0.03	b.d.l.	100.02
PCC-18-15A_olivsp8_oliv	38.35	0.01	0.03	0.01	22.76	0.08	0.39	38.15	0.17	0.01	0.10	b.d.l.	100.04
PCC-18-15A_olivsp8_oliv	38.24	0.02	0.02	0.01	22.65	0.08	0.40	37.93	0.17	0.01	0.12	b.d.l.	99.63
PCC-18-15A_olivsp17_oliv	38.44	0.01	0.03	0.02	22.86	0.07	0.39	38.05	0.17	0.00	0.06	b.d.l.	100.10
PCC-18-15A_olivsp17_oliv	38.24	b.d.l.	0.03	0.02	22.75	0.08	0.39	37.99	0.16	0.01	0.13	b.d.l.	99.81
PCC-18-15A_olivsp17_oliv	38.53	0.02	0.02	0.01	22.95	0.08	0.40	38.06	0.18	0.00	0.02	0.00	100.28
PCC-18-15A_olivsp10_oliv	38.54	b.d.l.	0.02	b.d.l.	22.88	0.08	0.38	38.16	0.16	b.d.l.	0.07	b.d.l.	100.29
PCC-18-15A_olivsp10_oliv	38.51	b.d.l.	0.03	b.d.l.	22.82	0.08	0.39	38.10	0.17	b.d.l.	0.09	0.00	100.19
PCC-18-15A_olivsp10_oliv	38.37	0.01	0.03	b.d.l.	22.86	0.07	0.39	38.03	0.17	0.00	0.06	b.d.l.	99.99
PCC-18-15A_olivsp13_oliv	38.12	0.01	0.02	b.d.l.	24.64	0.07	0.46	36.33	0.17	0.00	b.d.l.	b.d.l.	99.82
PCC-18-15A_olivsp13_oliv	38.55	b.d.l.	0.02	b.d.l.	23.10	0.07	0.40	37.70	0.17	b.d.l.	b.d.l.	b.d.l.	100.04
PCC-18-15A_olivsp13_oliv	38.52	b.d.l.	0.02	b.d.l.	22.81	0.08	0.41	37.73	0.19	0.01	b.d.l.	0.00	99.79
PCC-18-15A_olivsp14_oliv	37.54	0.02	0.02	b.d.l.	22.56	0.11	0.38	37.70	0.17	0.00	0.11	0.02	98.64
PCC-18-15A_olivsp14_oliv	37.50	0.01	0.02	b.d.l.	22.57	0.11	0.39	37.77	0.17	b.d.l.	b.d.l.	0.07	98.58
PCC-18-17A-1_olivsp1_oliv	37.84	b.d.l.	0.02	b.d.l.	25.88	0.04	0.46	35.27	0.16	b.d.l.	b.d.l.	0.00	99.69
PCC-18-17A-1_olivsp1_oliv	37.78	0.01	0.02	b.d.l.	26.22	0.04	0.45	34.92	0.16	b.d.l.	b.d.l.	b.d.l.	99.61
PCC-18-17A-1_olivsp1_oliv	37.81	0.01	0.02	b.d.l.	26.16	0.05	0.48	35.00	0.18	b.d.l.	b.d.l.	0.00	99.69
PCC-18-17A-1_olivsp4_oliv	37.78	0.02	0.03	b.d.l.	25.80	0.05	0.46	35.07	0.17	0.01	0.10	b.d.l.	99.48
PCC-18-17A-1_olivsp4_oliv	37.77	0.01	0.03	0.01	25.83	0.05	0.47	35.33	0.17	0.01	0.10	b.d.l.	99.77
PCC-18-17A-1_olivsp4_oliv	37.76	b.d.l.	0.03	b.d.l.	25.61	0.04	0.46	35.44	0.18	0.01	0.01	b.d.l.	99.54
PCC-18-17A-1_olivsp5_oliv	36.93	0.03	0.03	0.01	30.20	0.03	0.67	31.35	0.15	0.01	0.02	b.d.l.	99.43
PCC-18-17A-1_olivsp5_oliv	37.18	0.02	0.03	0.01	28.16	0.05	0.57	33.00	0.16	0.01	0.01	b.d.l.	99.18
PCC-18-17A-1_olivsp5_oliv	37.53	0.02	0.02	0.02	26.03	0.04	0.48	34.96	0.16	b.d.l.	b.d.l.	b.d.l.	99.26
PCC-18-17A-1_olivsp6_oliv	37.34	b.d.l.	0.03	b.d.l.	26.26	0.04	0.47	34.65	0.17	0.00	0.01	b.d.l.	98.97
PCC-18-17A-1_olivsp6_oliv	37.63	0.01	0.02	b.d.l.	26.00	0.05	0.46	35.10	0.17	0.00	b.d.l.	b.d.l.	99.43
PCC-18-17A-1_olivsp6_oliv	37.62	0.02	0.02	b.d.l.	25.87	0.04	0.47	35.18	0.17	0.00	0.01	0.00	99.41
PCC-18-17A-1_olivsp10_oliv	38.55	b.d.l.	0.03	0.01	23.74	0.07	0.39	37.31	0.17	0.00	0.03	0.00	100.31
PCC-18-17A-1_olivsp10_oliv	38.35	0.01	0.02	0.01	24.68	0.05	0.43	36.49	0.18	0.00	b.d.l.	b.d.l.	100.24
PCC-18-17A-1_olivsp10_oliv	38.44	0.01	0.03	0.01	24.30	0.06	0.41	36.69	0.17	0.01	0.01	b.d.l.	100.13
PCC-18-15C_olivsp1_oliv	38.76	b.d.l.	0.02	0.02	20.66	0.09	0.34	39.77	0.19	b.d.l.	0.02	0.00	99.87
PCC-18-15C_olivsp1_oliv	38.81	0.02	0.02	0.02	20.21	0.09	0.32	39.99	0.19	0.00	b.d.l.	b.d.l.	99.67
PCC-18-15C_olivsp1_oliv	38.93	0.01	0.03	0.03	20.40	0.09	0.33	39.87	0.19	0.00	b.d.l.	0.00	99.88
PCC-18-15C_olivsp3_oliv	37.18	0.01	0.02	b.d.l.	27.66	0.04	0.49	33.68	0.17	b.d.l.	0.01	b.d.l.	99.26
PCC-18-15C_olivsp3_oliv	38.00	0.02	0.02	b.d.l.	24.73	0.04	0.43	36.28	0.18	0.01	b.d.l.	b.d.l.	99.70
PCC-18-15C_olivsp3_oliv	37.30	0.01	0.02	b.d.l.	28.69	0.03	0.54	33.03	0.17	b.d.l.	b.d.l.	0.00	99.79
PCC-18-15C_olivsp4_oliv	38.13	0.01	0.03	0.01	22.86	0.06	0.39	37.95	0.18	b.d.l.	0.02	b.d.l.	99.63
PCC-18-15C_olivsp4_oliv	38.34	b.d.l.	0.02	0.01	22.06	0.06	0.36	38.70	0.18	0.00	b.d.l.	b.d.l.	99.76
PCC-18-15C_olivsp4_oliv	38.53	b.d.l.	0.03	0.01	22.41	0.07	0.38	38.33	0.18	0.00	0.03	0.00	99.99
PCC-18-15C_olivsp5_oliv	39.08	0.01	0.03	0.04	21.24	0.07	0.36	39.58	0.20	0.00	0.02	b.d.l.	100.63
PCC-18-15C_olivsp5_oliv	39.00	b.d.l.	0.03	0.01	20.62	0.08	0.33	40.00	0.19	0.01	b.d.l.	0.00	100.28
PCC-18-15C_olivsp5_oliv	38.94	b.d.l.	0.03	0.02	20.57	0.06	0.34	39.87	0.20	0.00	0.01	b.d.l.	100.04

ESM 3.5. UNR EPMA analyses of spinel inclusions.

SAMPLE	SiO2	TiO2	Al2O3	Cr2O3	FeO	NiO	MnO	MgO	CaO	Na2O	O	TOTAL
PCC-18-15A_olivsp1_sp100nA_3um	0.12	2.40	9.36	12.47	62.95	0.07	0.33	4.41	0.02	0.05	4.04	96.21
PCC-18-15A_olivsp2_sp_3um	0.11	2.68	9.03	10.72	64.82	0.06	0.33	4.33	0.01	0.04	4.21	96.34
PCC-18-15A_olivsp2_sp_1um	0.12	2.73	9.04	10.69	64.83	0.07	0.34	4.31	0.01	0.04	4.20	96.37
PCC-18-15A_olivsp1_sp_1um	0.11	2.35	9.37	12.37	62.65	0.06	0.34	4.35	0.02	0.04	4.02	95.67
PCC-18-15A_olivsp3_sp	0.11	3.61	9.40	11.05	64.37	0.06	0.35	4.01	0.05	0.04	3.98	97.03
PCC-18-15A_olivsp4_sp	0.10	1.17	12.09	15.45	59.18	0.08	0.34	4.99	0.01	0.04	3.75	97.20
PCC-18-15A_olivsp5_sp	0.10	0.86	10.79	16.21	59.78	0.07	0.33	4.70	0.01	0.04	3.85	96.74
PCC-18-15A_olivsp6_sp	0.11	1.41	9.90	17.93	59.02	0.06	0.35	4.73	0.02	0.03	3.70	97.27
PCC-18-15A_olivsp7_sp	0.10	1.94	9.79	13.79	62.23	0.06	0.33	4.63	0.01	0.03	4.00	96.91
PCC-18-15A_olivsp8_sp	0.13	1.22	9.98	16.31	59.35	0.07	0.35	4.70	0.02	0.03	3.79	95.95
PCC-18-15A_olivsp17_sp	0.09	1.54	9.91	16.72	60.10	0.07	0.35	4.81	0.01	0.03	3.82	97.44
PCC-18-15A_olivsp10_sp	2.70	1.00	9.65	11.42	62.91	0.08	0.32	6.38	0.03	0.04	4.04	98.59
PCC-18-15A_olivsp13_sp	0.17	3.76	7.49	4.28	72.97	0.05	0.36	3.38	0.03	0.05	4.85	97.38
PCC-18-15A_olivsp14_sp	0.15	7.40	7.42	6.72	65.86	0.12	0.35	4.50	0.04	0.04	3.91	96.47
PCC-18-17A-1_olivsp1_sp	0.14	9.09	6.72	1.89	71.44	0.04	0.39	3.31	0.01	0.05	4.14	97.21
PCC-18-17A-1_olivsp4_sp	0.10	2.65	9.63	19.07	56.87	0.03	0.39	4.21	0.05	0.03	3.28	96.32
PCC-18-17A-1_olivsp5_sp	0.12	8.44	5.10	5.17	70.62	0.02	0.43	3.30	0.02	0.04	4.14	97.40
PCC-18-17A-1_olivsp6_sp	2.69	2.98	7.96	14.94	57.92	0.03	0.41	5.02	0.04	0.03	3.20	95.21
PCC-18-17A-1_olivsp10_sp	0.09	1.00	21.13	26.22	41.54	0.05	0.36	6.85	0.01	0.03	1.86	99.14
PCC-18-15C_olivsp1_sp	0.08	1.45	17.64	26.56	42.74	0.07	0.34	7.17	0.11	0.02	2.12	98.28
PCC-18-15C_olivsp3_sp	0.09	17.75	3.16	0.10	69.37	0.00	0.52	2.84	0.02	0.04	3.03	96.91
PCC-18-15C_olivsp4_sp	0.13	2.95	10.90	20.33	53.55	0.05	0.41	4.93	0.00	0.03	2.98	96.24
PCC-18-15C_olivsp5_sp	0.07	3.36	11.56	21.99	51.64	0.05	0.35	5.72	0.09	0.03	2.80	97.65

ESM 3.5. UNR EPMA clinopyroxene spot analyses.

SAMPLE	core vs rim	Na2O	Al2O3	SiO2	MgO	P2O5	CaO	FeO	MnO	NiO	Cr2O3	TiO2	O	TOTAL
PCC-18-15A_cpx8	c	0.20	2.11	52.90	16.44	b.d.l.	21.55	6.00	0.17	0.01	0.29	0.39	b.d.l.	100.06
PCC-18-15A_cpx8	c	0.28	4.00	50.85	15.13	b.d.l.	21.69	6.57	0.16	0.02	0.46	0.69	b.d.l.	99.85
PCC-18-15A_cpx8	r	0.39	5.28	47.82	12.36	b.d.l.	20.61	11.00	0.26	b.d.l.	0.01	1.56	b.d.l.	99.28
PCC-18-15A_cpx8	r	0.50	5.48	46.90	11.24	b.d.l.	21.25	11.45	0.28	b.d.l.	b.d.l.	2.24	0.00	99.32
PCC-18-15A_cpx9	c	0.26	3.56	51.12	15.21	b.d.l.	21.68	6.67	0.17	b.d.l.	0.46	0.67	b.d.l.	99.79
PCC-18-15A_cpx9	c	0.23	2.14	52.90	16.21	b.d.l.	21.85	6.04	0.17	b.d.l.	0.26	0.41	b.d.l.	100.22
PCC-18-15A_cpx9	c	0.24	2.48	52.27	15.61	b.d.l.	22.00	6.50	0.18	0.01	0.12	0.52	b.d.l.	99.93
PCC-18-15A_cpx9	r	0.31	2.72	50.65	13.88	b.d.l.	20.29	10.49	0.29	b.d.l.	b.d.l.	0.89	b.d.l.	99.53
PCC-18-15A_cpx9	r	0.41	3.96	49.59	12.52	b.d.l.	21.49	10.21	0.29	b.d.l.	b.d.l.	1.21	0.00	99.66
PCC-18-15A_cpx10	c	0.26	3.73	51.14	15.28	b.d.l.	21.68	6.81	0.18	0.01	0.42	0.68	b.d.l.	100.19
PCC-18-15A_cpx10	r	0.43	2.81	50.50	13.29	b.d.l.	20.65	10.24	0.41	b.d.l.	b.d.l.	1.25	0.00	99.60
PCC-18-15A_cpx11	c	0.22	2.19	53.01	16.37	b.d.l.	21.90	6.12	0.21	0.01	0.27	0.40	b.d.l.	100.70
PCC-18-15A_cpx11	c	0.25	2.62	52.22	15.72	b.d.l.	21.99	6.47	0.16	b.d.l.	0.14	0.53	0.00	100.11
PCC-18-15A_cpx11	r	0.43	4.54	47.64	11.99	b.d.l.	20.87	11.61	0.25	b.d.l.	b.d.l.	1.58	b.d.l.	98.91
PCC-18-15A_cpx11	r	0.28	2.39	51.52	14.33	b.d.l.	20.61	9.68	0.28	b.d.l.	0.02	0.80	b.d.l.	99.89
PCC-18-15A_cpx12	c	0.26	2.55	52.23	15.56	b.d.l.	21.87	6.85	0.17	0.01	0.08	0.58	0.00	100.15
PCC-18-15A_cpx12	c	0.25	2.61	52.18	15.49	b.d.l.	21.89	6.72	0.17	b.d.l.	0.10	0.59	0.00	100.00
PCC-18-15A_cpx12	r	0.36	4.60	49.03	12.83	b.d.l.	21.25	9.92	0.25	0.01	b.d.l.	1.31	0.00	99.58
PCC-18-15A_cpx12	r	0.44	4.87	47.75	11.68	b.d.l.	20.99	11.54	0.24	b.d.l.	0.01	1.62	0.00	99.15
PCC-18-15A_cpx13	c	0.22	2.15	52.72	16.22	b.d.l.	21.80	6.11	0.16	0.02	0.25	0.40	0.00	100.04
PCC-18-15A_cpx13	c	0.24	3.64	51.20	15.28	b.d.l.	22.02	6.43	0.15	0.01	0.40	0.65	b.d.l.	100.02
PCC-18-15A_cpx13	r	0.49	5.39	46.19	10.90	b.d.l.	21.32	11.82	0.31	b.d.l.	b.d.l.	2.19	b.d.l.	98.61
PCC-18-15A_cpx13	r	0.26	2.86	51.78	15.42	b.d.l.	21.82	6.65	0.17	b.d.l.	0.14	0.61	b.d.l.	99.72
PCC-18-15A_cpx14	c	0.24	2.29	52.09	15.92	b.d.l.	22.05	6.15	0.17	b.d.l.	0.23	0.45	b.d.l.	99.59
PCC-18-15A_cpx14	c	0.20	2.08	52.94	16.25	b.d.l.	21.97	5.96	0.16	b.d.l.	0.25	0.41	b.d.l.	100.21
PCC-18-15A_cpx14	r	0.25	2.62	51.69	15.31	b.d.l.	21.08	7.95	0.22	0.01	0.05	0.67	b.d.l.	99.85
PCC-18-15A_cpx14	r	0.31	2.52	51.18	13.98	b.d.l.	20.62	10.07	0.28	b.d.l.	0.01	0.85	b.d.l.	99.81
PCC-18-15A_cpx14	r	0.22	2.47	52.22	15.86	b.d.l.	22.13	6.15	0.15	0.01	0.22	0.48	b.d.l.	99.90
PCC-18-15A_cpx15	c	0.26	2.85	51.71	15.32	b.d.l.	21.91	6.72	0.20	b.d.l.	0.11	0.62	b.d.l.	99.71
PCC-18-15A_cpx15	r	0.47	4.85	47.84	11.18	b.d.l.	21.60	11.43	0.30	b.d.l.	b.d.l.	1.77	0.00	99.46
PCC-18-15A_cpx15	r	0.38	4.39	49.13	12.78	b.d.l.	20.77	10.57	0.24	b.d.l.	0.01	1.35	b.d.l.	99.62
PCC-18-15C_cpx8	c	0.27	3.48	51.03	14.79	b.d.l.	21.75	7.40	0.18	b.d.l.	0.22	0.67	b.d.l.	99.78
PCC-18-15C_cpx8	c	0.19	2.04	52.88	16.21	b.d.l.	21.12	6.58	0.22	b.d.l.	0.23	0.37	0.00	99.86
PCC-18-15C_cpx8	r	0.37	4.81	47.98	11.88	b.d.l.	20.69	11.69	0.25	b.d.l.	b.d.l.	1.53	b.d.l.	99.20
PCC-18-15C_cpx8	r	0.36	4.76	48.17	12.41	b.d.l.	20.72	10.88	0.24	b.d.l.	0.01	1.37	b.d.l.	98.91
PCC-18-15C_cpx9	c	0.27	4.60	50.17	14.80	b.d.l.	20.93	7.43	0.21	0.01	0.29	0.85	0.00	99.55
PCC-18-15C_cpx9	c	0.25	3.94	50.92	14.85	b.d.l.	21.82	7.10	0.17	b.d.l.	0.36	0.68	b.d.l.	100.09
PCC-18-15C_cpx9	c	0.25	3.16	51.40	15.04	b.d.l.	21.79	7.26	0.18	b.d.l.	0.22	0.59	0.00	99.89
PCC-18-15C_cpx9	r	0.38	4.01	49.32	12.27	b.d.l.	20.72	11.22	0.31	b.d.l.	0.01	1.16	b.d.l.	99.41
PCC-18-15C_cpx9	r	0.36	4.00	49.33	12.37	b.d.l.	21.13	10.73	0.30	b.d.l.	b.d.l.	1.20	b.d.l.	99.42
PCC-18-15C_cpx9	r	0.36	4.40	48.90	12.90	b.d.l.	20.70	10.71	0.23	b.d.l.	0.01	1.34	0.00	99.55
PCC-18-15C_cpx10	c	0.29	4.77	50.32	14.62	b.d.l.	21.14	7.96	0.21	b.d.l.	0.16	0.92	b.d.l.	100.40
PCC-18-15C_cpx10	c	0.20	2.13	53.41	16.21	b.d.l.	21.52	6.64	0.19	b.d.l.	0.18	0.41	b.d.l.	100.90
PCC-18-15C_cpx10	c	0.21	2.13	52.96	16.11	b.d.l.	21.47	6.82	0.21	0.01	0.16	0.40	b.d.l.	100.49
PCC-18-15C_cpx10	c	0.23	2.38	52.40	15.75	b.d.l.	21.49	7.17	0.19	b.d.l.	0.15	0.45	b.d.l.	100.22
PCC-18-15C_cpx10	r	0.36	4.32	49.16	12.79	b.d.l.	20.79	10.94	0.28	b.d.l.	b.d.l.	1.35	0.00	99.99
PCC-18-15C_cpx10	r	0.38	4.26	49.05	12.41	b.d.l.	20.68	11.70	0.28	b.d.l.	0.01	1.30	0.00	100.07

SAMPLE	core vs rim	Na2O	Al2O3	SiO2	MgO	P2O5	CaO	FeO	MnO	NiO	Cr2O3	TiO2	O	TOTAL
PCC-18-15C_cpx11	c	0.20	2.01	52.55	15.99	b.d.l.	21.41	6.84	0.19	0.01	0.18	0.40	0.00	99.78
PCC-18-15C_cpx11	c	0.20	2.03	52.98	16.18	b.d.l.	21.49	6.68	0.20	b.d.l.	0.22	0.39	0.00	100.39
PCC-18-15C_cpx11	r	0.37	4.35	48.82	12.34	b.d.l.	20.78	11.30	0.25	b.d.l.	b.d.l.	1.28	b.d.l.	99.49
PCC-18-15C_cpx11	r	0.38	4.52	48.31	12.03	b.d.l.	20.65	11.73	0.28	b.d.l.	0.01	1.40	b.d.l.	99.30
PCC-18-15C_cpx12	c	0.37	3.61	49.24	12.33	b.d.l.	20.83	11.37	0.37	b.d.l.	b.d.l.	1.37	b.d.l.	99.50
PCC-18-15C_cpx12	r	0.35	2.89	50.34	12.60	b.d.l.	19.72	12.15	0.50	b.d.l.	b.d.l.	1.12	b.d.l.	99.68
PCC-18-17A-1_cpx8	c	0.24	4.63	50.10	14.30	b.d.l.	21.83	7.50	0.18	b.d.l.	0.20	0.92	0.00	99.90
PCC-18-17A-1_cpx8	c	0.20	2.03	52.55	16.06	b.d.l.	20.64	7.81	0.26	b.d.l.	0.11	0.42	b.d.l.	100.08
PCC-18-17A-1_cpx8	r	0.37	3.73	49.58	13.06	b.d.l.	20.43	10.40	0.30	b.d.l.	b.d.l.	1.20	b.d.l.	99.06
PCC-18-17A-1_cpx8	r	0.36	3.29	50.28	13.53	b.d.l.	20.25	10.38	0.37	b.d.l.	b.d.l.	1.22	b.d.l.	99.65
PCC-18-17A-1_cpx9	c	0.26	3.99	50.60	14.24	b.d.l.	21.75	8.19	0.18	b.d.l.	0.08	0.83	0.00	100.13
PCC-18-17A-1_cpx9	c	0.19	2.21	53.16	16.15	b.d.l.	21.39	6.85	0.19	b.d.l.	0.12	0.43	0.00	100.70
PCC-18-17A-1_cpx9	r	0.35	2.85	50.83	13.90	b.d.l.	20.20	10.08	0.42	b.d.l.	b.d.l.	1.07	b.d.l.	99.70
PCC-18-17A-1_cpx9	r	0.39	3.35	50.60	13.35	b.d.l.	20.65	10.48	0.32	b.d.l.	b.d.l.	1.20	0.00	100.33
PCC-18-17A-1_cpx10	c	0.27	3.66	50.74	14.24	b.d.l.	21.52	8.57	0.21	b.d.l.	0.03	0.85	b.d.l.	100.08
PCC-18-17A-1_cpx10	c	0.37	4.43	48.93	13.15	b.d.l.	19.27	11.84	0.35	b.d.l.	b.d.l.	1.53	b.d.l.	99.84
PCC-18-17A-1_cpx10	r	0.26	4.26	50.45	14.41	b.d.l.	21.43	8.07	0.19	b.d.l.	0.13	0.84	0.00	100.06
PCC-18-17A-1_cpx10	r	0.36	4.08	49.41	13.61	b.d.l.	18.68	11.80	0.36	b.d.l.	b.d.l.	1.31	0.00	99.62
PCC-18-17A-1_cpx11	c	0.19	2.25	53.06	16.16	b.d.l.	21.44	7.04	0.20	b.d.l.	0.13	0.43	0.00	100.90
PCC-18-17A-1_cpx11	r	0.41	4.36	49.01	12.97	b.d.l.	19.13	12.03	0.40	b.d.l.	b.d.l.	1.59	b.d.l.	99.90
PCC-18-17A-1_cpx12	c	0.19	2.25	52.76	16.28	b.d.l.	21.09	6.98	0.19	b.d.l.	0.11	0.42	b.d.l.	100.28
PCC-18-17A-1_cpx12	c	0.29	3.09	51.60	14.59	b.d.l.	21.58	8.26	0.22	b.d.l.	b.d.l.	0.68	b.d.l.	100.32
PCC-18-17A-1_cpx12	r	0.37	3.78	49.78	13.10	b.d.l.	20.54	10.50	0.29	b.d.l.	b.d.l.	1.17	b.d.l.	99.53
PCC-18-17A-1_cpx13	c	0.19	2.18	52.95	16.28	b.d.l.	21.03	7.12	0.23	0.02	0.10	0.41	0.00	100.50
PCC-18-17A-1_cpx13	c	0.29	2.89	51.88	14.99	b.d.l.	21.57	7.93	0.21	b.d.l.	0.07	0.70	b.d.l.	100.53
PCC-18-17A-1_cpx13	r	0.38	3.45	49.96	13.36	b.d.l.	20.44	10.70	0.31	b.d.l.	b.d.l.	1.09	0.00	99.69
PCC-18-17A-1_cpx13	r	0.35	4.03	49.36	13.81	b.d.l.	19.83	10.31	0.30	b.d.l.	b.d.l.	1.18	b.d.l.	99.17
PCC-18-17A-1_cpx14	c	0.24	4.73	49.96	14.37	b.d.l.	21.62	7.44	0.18	b.d.l.	0.35	0.88	0.00	99.78
PCC-18-17A-1_cpx14	c	0.25	2.17	52.38	15.36	b.d.l.	21.03	8.01	0.24	0.02	0.02	0.49	b.d.l.	99.97
PCC-18-17A-1_cpx14	r	0.36	3.13	50.47	13.57	b.d.l.	20.64	10.35	0.36	b.d.l.	b.d.l.	1.09	b.d.l.	99.97
PCC-18-17A-1_cpx14	r	0.29	1.71	52.41	14.58	b.d.l.	19.65	10.35	0.43	b.d.l.	b.d.l.	0.67	b.d.l.	100.09
PCC-18-16-1_cpx7	c	0.26	4.60	50.52	14.46	b.d.l.	22.04	7.13	0.14	b.d.l.	0.25	0.70	b.d.l.	100.09
PCC-18-16-1_cpx7	c	0.25	2.94	52.19	15.33	b.d.l.	22.13	6.77	0.18	b.d.l.	0.36	0.55	b.d.l.	100.72
PCC-18-16-1_cpx7	r	0.40	4.34	48.86	12.42	b.d.l.	20.23	11.81	0.33	b.d.l.	b.d.l.	1.26	b.d.l.	99.64
PCC-18-16-1_cpx7	r	0.38	4.69	48.03	12.60	b.d.l.	18.89	12.63	0.38	b.d.l.	b.d.l.	1.56	b.d.l.	99.17
PCC-18-16-1_cpx8	c	0.24	4.03	50.80	14.81	b.d.l.	21.96	7.15	0.17	b.d.l.	0.17	0.73	b.d.l.	100.06
PCC-18-16-1_cpx8	c	0.25	4.30	50.40	14.76	b.d.l.	21.71	7.05	0.15	0.01	0.36	0.77	b.d.l.	99.77
PCC-18-16-1_cpx8	r	0.37	4.70	48.57	12.83	b.d.l.	19.25	12.33	0.29	b.d.l.	b.d.l.	1.33	b.d.l.	99.69
PCC-18-16-1_cpx8	r	0.34	4.72	48.75	12.96	b.d.l.	20.22	11.11	0.26	b.d.l.	b.d.l.	1.30	0.00	99.68
PCC-18-16-1_cpx9	c	0.18	2.11	52.83	16.90	b.d.l.	20.38	6.93	0.20	b.d.l.	0.25	0.38	b.d.l.	100.15
PCC-18-16-1_cpx9	c	0.25	2.66	52.33	15.52	b.d.l.	21.89	6.97	0.17	b.d.l.	0.13	0.52	b.d.l.	100.44
PCC-18-16-1_cpx9	r	0.36	4.89	48.40	13.08	b.d.l.	19.02	12.27	0.31	b.d.l.	b.d.l.	1.37	0.00	99.71
PCC-18-16-1_cpx9	r	0.35	4.10	49.03	13.79	b.d.l.	17.77	12.89	0.35	b.d.l.	0.01	1.20	0.00	99.47
PCC-18-16-1_cpx10	c	0.23	2.44	52.50	15.77	b.d.l.	21.90	6.62	0.19	0.01	0.10	0.47	b.d.l.	100.22
PCC-18-16-1_cpx10	r	0.36	4.34	49.27	12.84	b.d.l.	20.31	11.56	0.27	b.d.l.	b.d.l.	1.22	b.d.l.	100.16
PCC-18-16-1_cpx10	r	0.37	4.77	48.53	12.94	b.d.l.	19.30	11.93	0.32	b.d.l.	0.01	1.28	b.d.l.	99.44
PCC-18-16-1_cpx11	c	0.24	4.37	50.47	14.63	b.d.l.	21.81	7.24	0.17	b.d.l.	0.21	0.81	b.d.l.	99.95
PCC-18-16-1_cpx11	r	0.36	5.07	48.03	12.97	b.d.l.	19.44	11.48	0.29	b.d.l.	0.01	1.36	0.00	99.00
PCC-18-16-1_cpx11	r	0.41	4.73	47.85	12.35	b.d.l.	19.69	12.10	0.33	b.d.l.	b.d.l.	1.60	b.d.l.	99.07
PCC-18-16-1_cpx12	c	0.26	2.99	51.61	15.11	b.d.l.	21.78	7.32	0.18	b.d.l.	0.14	0.61	b.d.l.	99.99
PCC-18-16-1_cpx12	r	0.37	4.11	48.99	12.85	b.d.l.	20.38	11.42	0.31	b.d.l.	b.d.l.	1.32	0.00	99.74
PCC-18-16-1_cpx13	c	0.24	2.64	52.44	15.57	b.d.l.	21.99	6.80	0.17	b.d.l.	0.14	0.49	b.d.l.	100.49
PCC-18-16-1_cpx13	r	0.37	4.56	48.55	12.51	b.d.l.	19.99	11.82	0.28	b.d.l.	b.d.l.	1.37	b.d.l.	99.46
PCC-18-16-1_cpx13	r	0.38	4.99	47.88	12.55	b.d.l.	20.25	11.46	0.27	b.d.l.	0.02	1.46	b.d.l.	99.26
PCC-18-16-1_cpx14	c	0.24	2.76	52.09	15.46	b.d.l.	22.02	6.82	0.18	b.d.l.	0.14	0.53	0.00	100.24
PCC-18-16-1_cpx14	c	0.23	2.70	52.11	15.67	b.d.l.	21.93	6.78	0.18	0.01	0.14	0.51	b.d.l.	100.24
PCC-18-16-1_cpx14	r	0.36	5.40	47.72	12.86	b.d.l.	19.60	11.41	0.29	b.d.l.	0.01	1.36	0.00	99.01
PCC-18-16-1_cpx14	r	0.37	4.32	48.45	12.62	b.d.l.	20.02	11.82	0.31	b.d.l.	b.d.l.	1.24	0.00	99.16

References

Bachmann, O., & Bergantz, G. W. (2004). On the Origin of Crystal-poor Rhyolites: Extracted from Batholithic Crystal Mushes. *Journal of Petrology*, *45*(8), 1565–1582. https://doi.org/10.1093/petrology/egh019

Bindeman, I. N., Davis, A. M., & Drake, M. J. (1998). Ion Microprobe Study of Plagioclase-Basalt Partition Experiments at Natural Concentration Levels of Trace Elements. *Geochimica et Cosmochimica Acta*, *62*(7), 1175–1193. https://doi.org/10.1016/S0016-7037(98)00047-7

Cashman, K. V., Sparks, R. S. J., & Blundy, J. D. (2017). Vertically extensive and unstable magmatic systems: A unified view of igneous processes. *Science*, *355*(6331), eaag3055. https://doi.org/10.1126/science.aag3055

Castro, J. M., Schipper, C. I., Mueller, S. P., Militzer, A. S., Amigo, A., Parejas, C. S., & Jacob, D. (2013). Storage and eruption of near-liquidus rhyolite magma at Cordón Caulle, Chile. *Bulletin of Volcanology*, *75*(4), 702. https://doi.org/10.1007/s00445-013-0702-9

Clynne, M. A., & Borg, L. E. (1997). OLIVINE AND CHROMIAN SPINEL IN PRIMITIVE CALC-ALKALINE AND THOLEIITIC LAVAS FROM THE SOUTHERNMOST CASCADE RANGE, CALIFORNIA: A REFLECTION OF RELATIVE FERTILITY OF THE SOURCE. *THE CANADIAN MINERALOGIST*.

Coogan, L. A., Saunders, A. D., & Wilson, R. N. (2014). Aluminum-in-olivine thermometry of primitive basalts: Evidence of an anomalously hot mantle source for large igneous provinces. *Chemical Geology*, *368*, 1–10. https://doi.org/10.1016/j.chemgeo.2014.01.004

Cooper, K. M., Sims, K. W. W., Eiler, J. M., & Banerjee, N. (2016). Timescales of storage and recycling of crystal mush at Krafla Volcano, Iceland. *Contributions to Mineralogy and Petrology*, *171*(6), 54. https://doi.org/10.1007/s00410-016-1267-3

Costa, F., Chakraborty, S., & Dohmen, R. (2003). Diffusion coupling between trace and major elements and a model for calculation of magma residence times using plagioclase. *Geochimica et Cosmochimica Acta*, *67*(12), 2189–2200. https://doi.org/10.1016/S0016-7037(02)01345-5

Dohmen, R., & Blundy, J. (2014). A predictive thermodynamic model for element partitioning between plagioclase and melt as a function of pressure, temperature and composition. *American Journal of Science*, *314*(9), 1319–1372. https://doi.org/10.2475/09.2014.04

Dohmen, R., & Chakraborty, S. (2007). Fe–Mg diffusion in olivine II: Point defect chemistry, change of diffusion mechanisms and a model for calculation of diffusion coefficients in natural olivine. *Physics and Chemistry of Minerals*, *34*(6), 409–430. https://doi.org/10.1007/s00269-007-0158-6

Donovan, J. J., Singer, J. W., & Armstrong, J. T. (2016). A new EPMA method for fast trace element analysis in simple matrices. *American Mineralogist*, *101*(8), 1839–1853. https://doi.org/10.2138/am-2016-5628

Faak, K., Chakraborty, S., & Coogan, L. A. (2013). Mg in plagioclase: Experimental calibration of a new geothermometer and diffusion coefficients. *Geochimica et Cosmochimica Acta*, *123*, 195–217. https://doi.org/10.1016/j.gca.2013.05.009

Faak, K., Coogan, L. A., & Chakraborty, S. (2014). A new Mg-in-plagioclase geospeedometer for the determination of cooling rates of mafic rocks. *Geochimica et Cosmochimica Acta*, *140*, 691–707. https://doi.org/10.1016/j.gca.2014.06.005

Faak, K., Coogan, L. A., & Chakraborty, S. (2015). Near conductive cooling rates in the upper-plutonic section of crust formed at the East Pacific Rise. *Earth and Planetary Science Letters*, *423*, 36–47. https://doi.org/10.1016/j.epsl.2015.04.025

Faak, K., & Gillis, K. M. (2016). Slow cooling of the lowermost oceanic crust at the fast-spreading East Pacific Rise. *Geology*, *44*(2), 115–118. https://doi.org/10.1130/G37353.1

Fagents, S. A., Gregg, T. K. P., & Lopes, R. M. C. (2013). *Modeling Volcanic Processes: The Physics and Mathematics of Volcanism*. Cambridge University Press.

Hildreth, W. (2004). Volcanological perspectives on Long Valley, Mammoth Mountain, and Mono Craters: Several contiguous but discrete systems. *Journal of Volcanology and Geothermal Research*, *136*(3), 169–198. https://doi.org/10.1016/j.jvolgeores.2004.05.019

Jay, J., Costa, F., Pritchard, M., Lara, L., Singer, B., & Herrin, J. (2014). Locating magma reservoirs using InSAR and petrology before and during the 2011–2012 Cordón Caulle silicic eruption. *Earth and Planetary Science Letters*, *395*, 254–266. https://doi.org/10.1016/j.epsl.2014.03.046

Jennings, E. S., Gibson, S. A., & Maclennan, J. (2019). Hot primary melts and mantle source for the Paraná-Etendeka flood basalt province: New constraints from Al-in-olivine thermometry. *Chemical Geology*, *529*, 119287. https://doi.org/10.1016/j.chemgeo.2019.119287

Kretz, R. (1994). Petrology of veined gneisses of the Otter complex, southern Grenville Province. *Canadian Journal of Earth Sciences*, *31*(5), 835–851. https://doi.org/10.1139/e94-077

LaTourrette, T., & Wasserburg, G. J. (1998). Mg diffusion in anorthite: Implications for the formation of early solar system planetesimals. *Earth and Planetary Science Letters*, *158*(3), 91–108. https://doi.org/10.1016/S0012-821X(98)00048-X

Lubbers, J., Kent, A. J. R., & de Silva, S. (2022). Thermal Budgets of Magma Storage Constrained by Diffusion Chronometry: The Cerro Galán Ignimbrite. *Journal of Petrology*, *63*(7), egac048. https://doi.org/10.1093/petrology/egac048

Mutch, E. J. F., Maclennan, J., & Madden-Nadeau, A. L. (2022). The dichotomous nature of Mg partitioning between plagioclase and melt: Implications for diffusion chronometry. *Geochimica et Cosmochimica Acta*, *339*, 173–189. https://doi.org/10.1016/j.gca.2022.10.035

Nakamura, M. (1995). Continuous mixing of crystal mush and replenished magma in the ongoing Unzen eruption. *Geology*, *23*(9), 807–810.

Neave, D. A., & Putirka, K. D. (2017). A new clinopyroxene-liquid barometer, and implications for magma storage pressures under Icelandic rift zones. *American Mineralogist*, *102*(4), 777–794. https://doi.org/10.2138/am-2017-5968

Németh, P., Tribaudino, M., Bruno, E., & Buseck, P. R. (2007). TEM investigation of Ca-rich plagioclase: Structural fluctuations related to the $I\bar{1}$-$P\bar{1}$ phase transition. *American Mineralogist*, *92*(7), 1080–1086. https://doi.org/10.2138/am.2007.2504

Phelps, P. R., Gonnermann, H. M., Winslow, H., Ruprecht, P., Pritchard, M. E., Delgado, F., & Liao, Y. (2023). Feasibility of melt segregation from a crystal mush in response to the 2011-12 eruption at Cordon Caulle. *Geophysical Journal International (in review)*

Ruprecht, P., Simon, A. C., & Fiege, A. (2020). The Survival of Mafic Magmatic Enclaves and the Timing of Magma Recharge. *Geophysical Research Letters*, *47*(14), e2020GL087186. https://doi.org/10.1029/2020GL087186

Seropian, G., Schipper, C. I., Harmon, L. J., Smithies, S. L., Kennedy, B. M., Castro, J. M., Alloway, B. V., & Forte, P. (2021). A century of ongoing silicic volcanism at Cordón Caulle, Chile: New constraints on the magmatic system involved in the 1921–1922, 1960 and 2011–2012 eruptions. *Journal of Volcanology and Geothermal Research*, *420*, 107406. https://doi.org/10.1016/j.jvolgeores.2021.107406

Singer, B. S., Jicha, B. R., Harper, M. A., Naranjo, J. A., Lara, L. E., & Moreno-Roa, H. (2008). Eruptive history, geochronology, and magmatic evolution of the Puyehue-Cordon Caulle volcanic complex, Chile. *Geological Society of America Bulletin*, *120*(5–6), 599–618. https://doi.org/10.1130/B26276.1

Van Orman, J. A., Cherniak, D. J., & Kita, N. T. (2014). Magnesium diffusion in plagioclase: Dependence on composition, and implications for thermal resetting of the 26Al–26Mg early solar system chronometer. *Earth and Planetary Science Letters*, *385*, 79–88. https://doi.org/10.1016/j.epsl.2013.10.026

Wan, Z., Coogan, L. A., & Canil, D. (2008). Experimental calibration of aluminum partitioning between olivine and spinel as a geothermometer. *American Mineralogist*, *93*(7), 1142–1147. https://doi.org/10.2138/am.2008.2758

Wieser, P. E., Kent, A. J. R., Till, C. B., Donovan, J., Neave, D. A., Blatter, D. L., & Krawczynski, M. J. (2023). Barometers Behaving Badly I: Assessing the Influence of Analytical and Experimental Uncertainty on Clinopyroxene Thermobarometry Calculations at Crustal Conditions. *Journal of Petrology*, *64*(2), egac126. https://doi.org/10.1093/petrology/egac126

Winslow, H., Ruprecht, P., Gonnermann, H. M., Phelps, P. R., Muñoz-Saez, C., Delgado, F., Pritchard, M., & Amigo, A. (2022). Insights for crystal mush storage utilizing mafic enclaves from the 2011–12 Cordón Caulle eruption. *Scientific Reports*, *12*(1), 9734. https://doi.org/10.1038/s41598-022-13305-y

Wong, K., Ferguson, D., Matthews, S., Morgan, D., Tadesse, A. Z., Sinetebeb, Y., & Yirgu, G. (2022). Exploring rift geodynamics in Ethiopia through olivine-spinel Al-exchange thermometry and

rare-earth element distributions. *Earth and Planetary Science Letters*, *597*, 117820. https://doi.org/10.1016/j.epsl.2022.117820

Zellmer, G. F., Blake, S., Vance, D., Hawkesworth, C., & Turner, S. (1999). Plagioclase residence times at two island arc volcanoes (Kameni Islands, Santorini, and Soufriere, St. Vincent) determined by Sr diffusion systematics. *Contributions to Mineralogy and Petrology*, *136*(4), 345–357. https://doi.org/10.1007/s004100050543

Zhukova, I., O'Neill, H., & Campbell, I. H. (2017). A subsidiary fast-diffusing substitution mechanism of Al in forsterite investigated using diffusion experiments under controlled thermodynamic conditions. *Contributions to Mineralogy and Petrology*, *172*(7), 53. https://doi.org/10.1007/s00410-017-1365-x

Chapter 4

Timescales of magmatic processes using Fe-Mg chemical and isotopic zoning in olivine

Heather Winslow[1], Philipp Ruprecht[1], Martin Oeser[2], Stefan Weyer[2]
[1]*University of Nevada, Reno*
[2]*Leibniz Universität Hannover, Germany*

Abstract

Fe and Mg isotope analyses are used to decipher the nature of chemical zoning (crystal growth vs diffusion) in olivine grains from mafic enclaves at Cordón Caulle, Chile, and improve timescale estimates calculated via diffusion chronometry. Isotopic analyses reveal chemical zonation is a product of diffusion throughout the entire grain with re-equilibration signatures within the core interior and large fractionation signatures at the rims (>1‰ in δ^{56}Fe and δ^{26}Mg), thus preserving two distinct phases of diffusion. Phase one assess timescales of re-equilibration operating within the interior of the core that has overprinted original chemical and isotopic profiles. An analytical model shows that full re-equilibration of olivine cores, with an ~10 mol% forsterite (Fo) variation and using crystals with ~100-250 μm crystal radius, takes ~10,000-80,000 years to re-equilibrate under shallow mush conditions. Phase 2 utilizes numerical solutions for Fe-Mg interdiffusion across the core to rim boundary that shows late-stage crystal growth and equilibration occurred on the order of ~2 months to 12 years prior to eruption. Isotopic analyses confirmed chemical zonation in Cordón Caulle olivine was entirely diffusion-driven and distilled the nuance of two growth and equilibration episodes improving estimates of the temporal magmatic evolution.

Introduction

Crystals hosted in magmatic systems preserve a wealth of information in their chemical zonation about pre-, syn-, and post-eruptive processes such as magma storage constraints and evidence of mixing and assimilation (Costa et al., 2008; Ruprecht et al., 2012; Cooper & Kent, 2014; Holness et al., 2019; Costa et al., 2020). This zonation can also preserve the rates and timescales on which these magmatic processes occur through diffusion chronometry (Costa et al., 2008, 2020). However, the interpretation of timescale estimates can be unreliable if the

nature of the chemical zonation is not determined (Teng et al. 2007; Teng et al. 2011; Sio et al. 2013; Oeser et al. 2015; Oeser et al. 2018). Chemical zonation at magmatic temperatures can be a product of varying processes, including the two endmembers of crystal growth and diffusion. If diffusion chronometry is conducted on zonation produced via crystal growth, the diffusion timescale estimates are meaningless and unreliable. In recent years, studies have shown that analysis of Fe and Mg isotopes along olivine zonation is a robust method in deciphering the processes that generate chemical zonation (i.e. crystal growth vs diffusion), thus improving estimates of magmatic timescales derived from diffusion studies (Teng et al. 2007; Richter et al., 2009; Dauphas et al., 2010; Teng et al. 2011; Sio et al. 2013; Oeser et al. 2015; Oeser et al. 2018). Diffusion is a product of disequilibrium between elemental compositions, and the kinetic process of diffusion is the system regaining equilibirum. In normal zonation, Fe and Mg diffuse in oppostie directions in olivine (Mg out of the crystal, Fe into the crystal), and during diffusion, lighter isotopes diffuse faster than their heavier counterparts leading to measurable kinetic fractionation (Teng et al., 2011; Weyer & Seitz, 2012; Sio et al., 2013; Oeser et al., 2015). This results in anticorrelated Fe-Mg isotopic profiles under diffusive conditions. Alternatively, crystal growth occurs presumably in equilibrium with the melt and does not fractioante isotopes at high temperatures. Consequently, crystal growth experienences minimal isotopic effects leading to flat isotopic profiles. Studies have shown that kinetic isotopic fractionation (generated by diffusive processes) can exceed signatures of equilibrium fractionation (generated by crystal growth) by an order of magnitude (Teng et al., 2011; Weyer & Seitz, 2012; Sio et al., 2013; Oeser et al., 2015). Consequently, Fe and Mg isotopes can be used as magmatic tracers that create distinct and unambiguous signatures for diffusion and crystal growth processes. Here we utilize this method to discern the details of magma storage processes operating at the active volcanic complex,

Puyehue-Cordón Caulle, Chile, and obtain realiable timescale estimates of magma residence and differentiation processes prior to eruption. Cordón Caulle presents a unique opportunity to test the limits of diffusvie processes

Cordón Caulle is part of a silicic fissure system within a larger volcanic complex, Puyehue-Cordón Caulle, in the Southern Andean Volcanic Zone (Singer et al., 2008; Winslow et al., 2022). There have been three rhyolitic historic eruptions in the last century (1921-22, 1960, 2011-12) with explosive and effusive eruptive styles (Castro et al., 2013; Jay et al., 2014; Schipper et al., 2021; Winslow et al., 2022). The most recent eruption contains crystal-rich basaltic enclaves hosted within the effusive rhyolite flow that represent fragments of an underlying crystal-rich magma mush (Winslow et al., 2022). The crystal's simple zonation paired with primitive whole-rock and mineral-scale compositions provides evidence for storage in a thermally and compositionally buffered system that is not disturbed by continual recharge events (Winslow et al. 2022). The crystal-rich magma mush represents a quasi-closed and simple system that is dominated by magmatic differentiation and can be used test the ability to preserve growth conditions in a simple magmatic system. Thus, these enclaves present a unique opportunity to test the nature of chemical zonation in a system where crystal growth dominates and mixing has not overprinted the growth zonation.

This study investigates the timescales associated with quasi-closed magma storage at Cordón Caulle and requires the use of isotopic analyses to decipher the nature of chemical zonation. Cordón Caulle's history of high crystallinity and significant fractionation paired with long-term storage in a crystal mush suggest both crystal growth and diffusion processes may impact chemical zonation at the crystal scale. Thus, it is imperative to distill the nature of zonation in the mafic enclaves to reliably retrieve magma residence estimates through diffusion chronometry.

Samples

We use crystal-rich (55-70 vol%) olivine-bearing basaltic enclaves from the 2011-12 Cordón Caulle eruption. The mafic enclaves display interlocking cumulate-like textures, simple zonation profiles within mineral phases, and are among the most basaltic endmember (50-53 wt% SiO_2, ~ 5- 9 wt% MgO, $Mg\#_{\sim 53\text{-}66}$) compared to mafic enclaves globally (Winslow et al. 2022). Interstitial melt within the enclaves is compositionally identical to the rhyolitic host melt (~ 75 wt% SiO_2), suggesting the crystal-poor rhyolite magma was derived directly from the underlying basaltic magma mush through efficient melt extraction (Winslow et al., 2022). The bulk rock major and trace element chemistry records crystal fractionation processes that is not strongly affected by crustal melting or assimilation which is suggestive of closed-system processes. Such efficient fractionation and high crystallinity mean the cores of the phenocrysts are quickly out of equilibrium with the evolved interstitial melt leading to large compositional contrasts. As such, the enclaves present a unique opportunity to test the origin of chemical zonation in a system where crystal growth dominates, mixing has not overprinted the growth zonation, and the large compositional gradient combined with extended storage within a crystal mush allows for effective diffusion processes (Chapter 3). The olivine grains display normal zonation in Mg and Fe with core compositions ranging from $Fo_{\sim 70\text{-}86}$ and rim compositions ranging from $Fo_{\sim 58\text{-}64}$ [Fo = 100*atomic Mg/(Mg+Fe)]. For individual grains, the difference between core and rim forsterite contents ranges from ~ 10 mol% up to 21 mol% (i.e. Fo_{73} core with Fo_{52} rim from PCC-18-15C olivine 1, line 2). The significant compositional contrasts of Mg and Fe within individual grains makes the mafic enclaves suitable samples to test diffusion-driven fractionation.

Methods

In-situ Fe and Mg isotope analyses

In situ Fe and Mg isotope analyses were collected on olivine grains within four enclave samples (PCC-18-15A, 15C, 16-1, 17A-1) using the femtosecond laser ablation coupled with multicollector inductively coupled plasma mass spectrometry (fs-laser ablation MC-ICP-MS) at the Institut für Mineralogie of Leibniz Universität Hannover (Germany). Methods, standardizations, and monitoring of instrumental mass bias were completed following the methods of Oeser et al. (2015) and results are reported in ESM 4.1-4.2. Bracketing standards used for Fe isotopes were BHVO-2G, BIR-1G, and IRMM-14, and standards used for Mg isotopes were BIR-1G, GOR 132-G, and DSM-3. Unknowns were analyzed using sample-standard bracketing with standards being measured every transect. Transects were collected from core to rim perpendicular to Fe-Mg zonation. In this study we report δ^{56}Fe and δ^{26}Mg values where,

$$\delta^{56}Fe_{sample} = \left(\frac{^{56}Fe/^{54}Fe_{sample}}{^{56}Fe/^{54}Fe_{BHVO-2G}} - 1\right) \times 10^3 \quad \text{(Eq. 1)}$$

$$\delta^{26}Mg_{sample} = \left(\frac{^{26}Mg/^{24}Mg_{sample}}{^{26}MG/^{24}Mg_{GOR132-G}} - 1\right) \times 10^3 \quad \text{(Eq. 2)}$$

and,

$$\delta^{56}\text{Fe} = \delta^{56}Fe_{sample} + \delta^{56}Fe_{BHVO-2G/IRMM-14} \quad \text{(Eq. 3)}$$

$$\delta^{26}\text{Mg} = \delta^{26}Mg_{sample} + \delta^{26}Mg_{GOR132-G/DSM-3} \quad \text{(Eq. 4)}$$

Electron Probe Microanalyzer Analyses

Major and trace element transects of select olivine crystals were analyzed using the JEOL JXA-iHP200F electron probe microanalyzer equipped with five wavelength dispersive spectrometers at the University of Nevada, Reno. A mean atomic number background method was used for standardizations (Donovan et al., 2016). For all analyses, we used a beam current of

50 nA, accelerating voltage of 15 kV, and a 1 μm spot size. The following elements were analyzed: Na (40 s), Al (60 s), Si (20 s), Mg (20 s), P (30 s), Ca (60 s), Fe (20 s), Mn (40 s), Ni (50 s), Cr (50 s), Ti (10 s). Results are reported in ESM 4.3. Transects were collected on several olivine grains adjacent to isotope transect pits to record the associated forsterite profiles used for modeling.

Qualitative maps of phosphorous (P) in three olivine grains were collected using the JEOL JXA-iHP200F electron probe microanalyzer at the University of Nevada, Reno. The maps display relative concentrations of P within olivine (ESM 4.4). Phosphorous is typically present in mafic magmas and preserves information about growth rates in olivine (Shea et al., 2015; 2019). P mapping can also decipher between processes that produce chemical zonation because it records rapid skeletal crystal growth. P diffusion is slow compared to Fe-Mg interdiffusion and preserves initial growth histories (Shea et al., 2015; 2019).

Diffusion Model

For our diffusion model, we use a 1-D diffusion equation that is solved numerically using the finite difference method, with the time-dependent diffusion coefficient varying as a function of forsterite content and position along the profile (Costa et al., 2008). The Fe-Mg diffusivity was calculated parallel to the *c*-axis [001] using the following equation (Dohmen & Chakraborty, 2007; Dohmen et al., 2007; Collinet et al., 2017):

$$D_{Fe-Mg} = 10^{-9.21} \times \left(\frac{fO_2}{10^{-7}}\right)^{1/6} \times 10^{3(X_{Fe}-0.1)} \times exp\left(-\frac{201{,}000+(P-10^5)\times 7\times 10^{-6}}{RT}\right) \quad \text{(Eq. 5)}$$

where $D_{Fe\text{-}Mg}$ is the diffusion coefficient of Fe-Mg interdiffusion in m^2/s, fO_2 is the oxygen fugacity in Pascals (Pa) (Huebner & Sato, 1970; Zhou, 1981; Schwab & Kustner, 1981; Herd, 2008), P is the lithostatic storage pressure in Pa, T is the temperature in Kelvin, and X_{Fe} is the

mole fraction of fayalite. Pressure and temperature values are taken from Chapter 3, which determined a range of applicable temperature and pressure estimates for these samples. Cpx-liq barometry estimates range from ~50-350 MPa, and pressure range leads to negligible difference in Fe-Mg interdiffusion and therefore associated timescale estimates. Thus, 200 MPa was used as an average pressure estimate. Mg-in-plagioclase thermometry produced a range of temperatures from 918-965°C, and these two end members were used to bracket changes in timescale estimates from slowest (920°C) to fastest (970°C) temperature conditions. The temperature constraints will strongly impact results. Here we chose to use the previously calculated storage temperatures for the mush (Chapter 3) as our thermal parameters in the model. Typical basalt storage temperatures are hotter and would increase diffusivity. Because Fe-Mg diffusion in olivine is anisotropic, we also calculate Fe-Mg diffusivity parallel to the *a/b*-axes [100, 010] which are both six times slower than diffusivity in the *c*-axis direction (referred to as D*c* and D*ab* hereafter; Nakamura & Schmalzried, 1983; Dohmen & Chakraborty, 2007; Hartley et al., 2016). Electron backscattered diffraction (EBSD) analyses would determine the axial direction; however, this data has yet to be collected, so we will utilize both the *c*- and *ab*-axis diffusivities to determine the minimum and maximum timescales and constrain an informed range of estimates.

Results

Olivine grains from Cordón Caulle display homogenous Fo interiors, considered flat cores (Winslow et al., 2022), with normally zoned evolved rim compositions. The evolved rims are present whenever olivine grains are not shielded by other mineral phases and are exposed to the evolving melt. The *in-situ* Fe and Mg isotope analyses display strong coupling between isotopic variations and chemical zonation (Fig. 4.1). We observe flat or negligible isotopic fractionation

within olivine cores and significant isotopic fractionation near the rims with inversely correlated isotopic signatures (Fig. 4.1, 4.2). The magnitude of variation in isotopic zoning across all analyzed olivine grains reaches up to 1.25‰ in $\delta^{56}Fe$, and 1.92‰ in $\delta^{26}Mg$ within all samples (Fig. 4.3). Individual grains display variations up to >1‰ in $\delta^{56}Fe$ and $\delta^{26}Mg$ (Fig. 4.1). Additionally, analyses reveal largely negative correlations between $\delta^{56}Fe$ and $\delta^{26}Mg$ across all samples and grains (Fig. 4.3). Qualitative P maps reveal skeletal growth patterns throughout the olivine in 2 grains within samples PCC-18-15C and PCC-18-15A (ESM 4.4). Sample PCC-18-17A-1 displays concentric P zoning in one grain (ESM 4.4). Skeletal growth recorded in P concentrations is indicative of rapid growth or undercooling (Welsch et al., 2013; Shea et al., 2015; 2018) and may reveal out-of-sequence growth histories during rapid growth (Salas et al. 2021).

Isotopic signatures for Cordón Caulle olivine appear to be isotopically light compared to standard basalt compositions (Fig. 4.4). The sample grains are on the lower portions of the terrestrial fractionation line (TFL) as a result of lighter $\delta^{57}Fe$ and $\delta^{56}Fe$ ratios. *In-situ* isotope analyses were also collected on Fe-oxides in three of the samples and are isotopically heavier than both the olivine grains from Cordón Caulle and the standards (Fig. 4.4). Sample PCC-18-15C displays the largest distribution on the TFL (>1‰ variation in $\delta^{56}Fe$ and $\delta^{57}Fe$; Fig. 4.4B) compared to smaller variations and isotopically heavier ranges in the other three samples (~0.3‰ variation in $\delta^{56}Fe$, ~0.6‰ variation in $\delta^{57}Fe$) (Fig. 4.4). Sample PCC-18-15C also displays the largest magnitude of isotopic fractionation in $\delta^{56}Fe$ and $\delta^{26}Mg$ compared to other samples (Fig. 4.1).

Discussion

Crystal Growth vs Diffusion

The coupling of isotopic and chemical zoning, negative correlations between $\delta^{56}Fe$ and $\delta^{26}Mg$, and the large magnitude of isotopic fractionation throughout all samples are indicative of diffusion-driven processes impacting the entire olivine grain (Teng et al., 2011; Sio et al., 2013; Oeser et al., 2015; Oeser et al., 2018). We observe two distinct phases of diffusion-driven processes: (1) the interiors of the cores that display flat, homogenous chemical zonation in forsterite paired with flat or negligible isotopic fractionation and (2) the core to rim boundary that displays large isotope fractionation paired with the normal zonation in forsterite (Fig. 4.1). The negligible fractionation in the olivine cores from Phase 1 can be a result of two scenarios: crystal growth or diffusive re-equilibration (Sio et al., 2013; Oeser et al., 2015). This is a product of how isotopes fractionate at magmatic temperatures. Crystal growth does not fractionate isotopes at magmatic temperatures and results in negligible or flat isotopic trends. In contrast, diffusive processes result in large kinetic fractionation at the onset of diffusion; however, if diffusion is allowed to progress over extended periods, both elemental and isotopic concentrations will re-equilibrate back to flat profiles. Re-equilibration will overprint initial chemical zonation and isotope fractionation signatures and produce flat profiles (Sio et al., 2013; Oeser et al., 2015; Winslow et al., 2020).

The enclaves have experienced extended storage within a thermally buffered crystal mush providing ideal conditions for re-equilibration to progress (Winslow et al., 2022). We present multiple lines of evidence for ongoing diffusive processes impacting the entirety of the olivine grains, including the coupling of isotopic and chemical Fo zoning, negative correlations between $\delta^{56}Fe$ and $\delta^{26}Mg$ across all samples, and the large magnitude of isotopic fractionation. These combined points suggest that the olivine grains experience kinetic isotopic fractionation produced from Fe-Mg interdiffusion and that the cores underwent diffusive re-equilibration as

opposed to equilibrium fractionation from crystal growth (Oeser et al., 2015). Thus, we can assume timescales calculated from these profiles would be reliable as diffusion has impacted the chemical and isotopic zonation throughout the entire grain.

Additionally, our P zoning results suggests olivine went through rapid growth to produce the skeletal morphology, but also exhibits diffusive driven zonation in Fo content (ESM 4.4; Welsch et al., 2013; Shea et al., 2015). Fo zoning throughout the entire grain does not reflect skeletal patterns, and studies suggest the non-conformity between dendritic P zones and concentric Fo zones is a product of Fe-Mg interdiffusion attempting to regain equilibrium (Shea et al., 2015; Shea et al., 2019). This would be in contrast toward initial Fo growth zonation that retain the skeletal growth patterns (Shea et al., 2015). Ultimately, we observe evidence for diffusive processes impacting olivine zonation using isotopic signatures, Fo zoning, and P zoning.

Timescale Estimates from Diffusion Models

Here we model the diffusion of forsterite profiles given the insight from isotopic signatures that diffusion is the dominant process impacting chemical zonation (e.g., Oeser et al., 2015; Oeser et al., 2018). Isotopic data has revealed two distinct phases of diffusion has occurred. Phase 1 encompasses diffusive re-equilibration within the interior of the core that is now compositionally flat in both elemental and isotopic zoning (Fig. 4.1). Phase 2 describes the chemical and isotopic zonation from the flat core to the evolved rim (core ~Fo_{73-74}, and rim ~Fo_{56-62}) that represents late-stage differentiation.

We use Fo diffusion modeling to reveal the timescales associated with Phase 2: the final olivine rim growth and storage prior to eruption. A range of timescales are produced for each of the four modeled grains reflecting variables in diffusivity from grain orientations as well as ranges in temperature (Fig. 4.5-8); results are summarized in Table 4.1. Minimum estimates for

three of the grains range from ~2-8 months using D*c* at 970°C, and maximum estimates range from ~3-12 years using D*ab* at 920°C (Table 4.1, Fig. 4.5-7), with profile lengths of ~150-165 μm. The fourth modeled grain, PCC-18-15C, is the largest grain with a modeled length of ~226 μm. The minimum timescale for this sample is ~1.5 years using D*c* at 970°C (Fig. 4.8C), while the maximum estimate is ~30 years using D*ab* at 920°C (Fig. 4.8B). Future work will also use diffusion modeling of isotopic profiles to further refine the models. Previous studies have shown timescales collected from Fo diffusion models is comparable as an initial estimate to the respective isotopic timescales (Oeser et al., 2015; Oeser et al., 2018).

Assuming diffusion profiles are along the *c*-axis and occurred at higher temperatures, results point toward relatively quick timescales of ~2-8 months for the smaller grains and a maximum of ~1.5 years for the larger grain for re-equilibration after a final growth episode. The quick timescales may suggest that final crystal growth and late-stage differentiation related to re-equilibration occurred shortly before the eruption. The whole-rock and melt chemistry of the enclaves and rhyolite may also support late-stage differentiation. Whole-rock chemistry of the rhyolite is ~70 wt% SiO_2; however, interstitial glass of the enclaves is slightly higher at ~75 wt% SiO_2 (Winslow et al., 2022). Under the conceptual model of the enclaves representing a crystal mush that generated the rhyolite melt cap, we expect these compositions to be identical. While they overlap and are nearly identical in other major and trace elements, the difference in SiO_2 suggests the enclaves have undergone further differentiation than the rhyolite whole-rock chemistry. The mafic enclaves represent fragments of the crystal mush but have been separated from the main crystal mush storage system once incorporated into the rhyolite. Timescales suggest late-stage differentiation is recorded in the enclaves after rhyolite incorporation. Thus, the final step in differentiation is impacting the interstitial melt of the enclaves while hosted in

the rhyolite, and the larger crystal mush may not undergo these changes as effectively. Ultimately, this suggests the interstitial glass of the crystal mush prior to incorporation is likely closer to the rhyolite whole-rock composition at ~70 wt% SiO_2, but once the enclaves are incorporated into the rhyolite, experience further differentiation elevating the interstitial glass to ~75 wt% SiO_2, which is the same as the interstitial glass in the rhyolite, and impacting the crystal record and diffusion models.

The enclaves were incorporated into the rhyolitic effusive flow which initially erupted approximately two weeks after the onset of eruption on June 4, 2011. Lava effusion sourced from the crater continued through March 2012, but the flow front continued to evolve through January 2013 (Tuffen et al. 2013; Farquharson et al., 2015). The continued evolution of the flow field for over a year after its cessation of producing new material points toward a level of thermal insulation in the flow (Tuffen et al., 2013). As a result, olivine diffusive re-equilibration could be sustained syn-eruptively and for several months post-eruption supporting the calculated timescales of months to ~1.5 years. Additionally, the "thin rim+melt" pairing for cpx-liq barometry from Chapter 3 suggests shallow pressures of <30 MPa. This cpx-liq pairing comes from very thin and evolved rims on clinopyroxene that seemingly represent the final episodes of growth and differentiation occurring at shallow, potentially conduit-level, depth associated with syn-eruptive processes. Both olivine and clinopyroxene have quantitative constraints supporting quicker pre-eruptive timescales at shallow levels with final steps of differentiation. Plagioclase may also support similar findings based on elemental zonation with high anorthite cores, lower anorthite mantles, and extremely thin rims with the lowest An content. These rims represent a final late-stage crystal growth period with evolved compositions (Winslow et al. 2022).

Alternatively, under the cooler extent of storage temperatures along the *c*-axis, timescales report a range from ~7 months to 2 years in the smaller grains and ~5 years in the large grain. These extended timescales are not likely related to syn-eruptive processes but may still be associated with pre-eruptive disruptions in the shallow magma chamber. Signals of pre-eruptive unrest of seismic activity and inflation were recorded up to ~7 months prior to the onset of eruption (Delgado et al., 2016; Basualto et al., 2023). Surficial inflation is typically a product of magma injection, production, or reorganization. This magma movement may have impacted the crystal record causing late-stage differentiation.

Regardless of grain orientation or temperature variables, we reveal that olivine core to evolved rim equilibration processes occurred on the order of months to less than 12 years (and 30 years in one single analyses) prior to eruption. Delgado et al (2021) indicates there were three phases of surficial uplift in the Cordón Caulle graben area that occurred in the ~8 years prior to eruption, with slower rates of inflation from 2003-2008 (3-4 mm/yr) and increased inflation from 2008-2010 (30 mm/yr). Previous assessments of enclave incorporation into the rhyolite melt cap from Mg-in-plagioclase geospeedometry suggest the enclaves were incorporated on the order of hundreds to thousands of years ago (Chapter 3). Thus, the enclaves would be present in the system for any later stage disruptions or magma reorganizations in the melt lens cap.

The enclaves exhibit a range in whole-rock and mineral chemistry that have been interpreted to represent variations within the crystal mush, where lower Fo olivine represent the long-lived mush and higher Fo olivine provide evidence for more recent mafic additions that compositionally sustain the mush chemistry (Winslow et al. (2022). The chemical variability may be connected to the variance observed in the timescales produced from Fo zoning. PCC-18-15C is the largest grain modeled, and the sample it is from is on the lower end of whole rock

Mg# (Fig. 4.9) compared to other samples. It is also the grain that exhibits the longest timescales. The variability in timescales and bulk-rock chemistry shows the preservation of mush heterogeneity and that enclaves that had experienced long-lived storage versus more recent additions in the mush were incorporated into the rhyolite.

Olivine Core Re-equilibration

The previous section modeled Phase 2 of the diffusive processes using Fo profiles from the homogenous core to the evolved rim to reveal timescales of late-stage crystallization and differentiation. This scenario makes an assumption about initial conditions for the olivine and the starting Fo contents. Based on the isotopic record (Fig. 4.1-3), there is evidence that diffusion impacted the entirety of the olivine grain. We observe two distinct trends of diffusion signatures. The core shows a plateau of negligible fractionation trends whereas the remainder of the grain shows large diffusive fractionation trends where Fo is also zoned. The latter is what was modeled in the previous section, estimating re-equilibration after two growth episodes from the initial flat interior toward more evolved rims. The former trends can be used to estimate timescales associated within the homogenous cores and are addressed in this section. We previously deduced that the flat isotopic trends for the interior of olivine grains are a result of diffusive processes. When the flat isotopic record is combined with flat Fo profiles, we assume diffusive re-equilibration was the driving force. We test this theory in this section by looking at melt-liquid equilibrium compositions between the olivine Fo compositions and their host (the mafic enclave) whole-rock Mg# compositions.

Long-lived storage within a thermally buffered crystal mush (Winslow et al., 2022; Chapter 3) presents an ideal environment for Fe-Mg interdiffusion to progress toward full re-equilibration and overprint initial Fo compositions resulting in unzoned cores as observed in our samples (Fig.

4.1; Winslow et al., 2022). Olivine cores in Cordón Caulle enclaves are largely not in equilibrium with the rhyolitic interstitial melt (i.e., orthopyroxene overgrowth and evolved rims), and the enclave samples they are hosted in have elevated whole-rock Mg# for their associated olivine Fo contents relative to the melt-liquid equilibrium (Fig. 4.9; $K_D^{Ol/liq}$=0.27-0.3; Roeder & Emslie 1970; Toplis, 2005). As presented in Winslow et al. (2020), this disequilibrium can be explained through accumulation or diffusive re-equilibration processes. Our samples lack chemical evidence for accumulation (major and trace element data; Winslow et al., 2022), have lower amounts of olivine phase assemblage (~10-15 vol%; Winslow et al., 2022), and do not display textural features of compression or alignment of grains that would be associated with accumulation (Holness et al., 2019). The lack of evidence for accumulation paired with the chemical and isotopic arguments previously made for diffusion driven processes, we suggest the olivine experienced diffusive re-equilibration. During re-equilibration, initial Fo contents in olivine have been overprinted. The original olivine Fo contents can be reconstructed using the relationship between Mg# in the whole-rock data with Fo content in olivine under the melt-liquid equilibrium conditions. Using this framework, we can reveal the Fo compositions that were present prior to diffusive re-equilibration under the assumption that accumulation was not impacting our samples (Fig. 4.9). Prior to re-equilibration, we estimate the original olivine Fo content ranged from $Fo_{85\text{-}90}$, compared to their current observed range at $Fo_{70\text{-}80}$ (Fig. 4.9). The results imply initial core compositions were closer to $Fo_{85\text{-}90}$ and equilibrated to $Fo_{70\text{-}80}$ compositions, which is an ~10 mol% variation (Fig. 4.9). To estimate the time required for Fe-Mg interdiffusion to reach the center of olivine grains, we use the following analytical solution that uses a planar-confined source and infinite reservoir relationship,

$$\Delta c(t) = 0.2\mathrm{erf}\left(\frac{x}{2\sqrt{Dt}}\right) \quad \text{(Eq. 6)}$$

where the concentration gradient within the interior of the core is within 1% of the edge of the core (Δc). The equation and model parameters follow that of Winslow et al. (2020). Typical diffusivities (D) used for Fe-Mg diffusion in basaltic systems (1000-1100°C, 400-700 MPa, ~100-250 μm crystal radius) range between 6.4×10^{-18} and 1.1×10^{-16} m^2/s (Dohmen and Chakraborty, 2007); however, we will also consider the storage parameters estimated in Chapter 3 that present shallower pressures and cooler storage temperatures (~100-300 MPa, ~920-970°C). Under the conditions presented in Chapter 3, the Fe-Mg diffusivities are slower and range from 3.04×10^{-18} and 7.76×10^{-18} m^2/s. We present both ranges of diffusivities in the model (Fig. 4.10). Using crystal radii of ~100-250 μm, as observed in mafic enclaves of the 2011-12 Cordón Caulle eruption, and combining those length scales with the associated range of $D_{Fe\text{-}Mg}$ from shallow mush conditions, we estimate full olivine core equilibration requires ~10,000-80,000 years (Fig. 4.10, solid line). These results present first ever estimates toward the longevity of the crystal mush storage system at Cordón Caulle and are indicative of protracted storage within the crust. Diffusion is highly dependent on temperature, and we acknowledge the use of previously calculated temperature estimates from Chapter 3 are cooler compared to typical basalts. Cooler temperatures will result in slower timescales. Because of this, our shallow mush parameters produce maximum timescale estimates. For comparison, we also present equilibration estimates using typical basalt conditions resulting in a dispersed range from 100-80,000 years depending on which diffusivity is used (Fig. 4.10, dashed line). Here, the typical basalt conditions experience hotter storage temperatures and thus, produces timescales several magnitudes shorter (10^4 vs 10^2 yr). Aluminum-in-olivine thermometry from Chapter 3 reveals initial crystallization temperatures ranged from 1240-1320°C, and furthermore, it is reasonable that these grains experienced varying temperatures that could have reduced the estimated

timeframe. However, we do not expect protracted storage occurred at deeper or hotter conditions in the crust based on the lack of differentiation present in the enclaves. Cordón Caulle enclaves present some of the most primitive compositions both regionally and in PCC's entire eruptive history (Winslow et al., 2022), and exhibit primitive whole-rock compositions (Fig. 4.9; Schmidt & Jagoutz, 2017). Extended storage within distinct magma chambers would likely result in continued differentiation and ultimately a more evolved crystal mush (i.e. andesite) at shallow levels as opposed to our basaltic mush at shallow depth (Christopher et al., 2015; Cashman et al., 2017). Thus, we focus on the proposed extended storage in shallow mush and utilize storage parameters calculated from Chapter 3. Our estimates of core equilibration lasting ~10,000-80,000 years is based on consistent storage in the shallow mush at 920-970°C and likely represents a maximum estimate. Ultimately, we can assume the olivine cores, and by extension the lifetime of olivine within the crystal mush, were stored on the order of tens of thousands of years with a maximum estimate of 80,000 years.

Conclusion

This is the first study to explore the history of the Cordón Caulle mafic enclaves using these techniques and provides first-ever timescale estimates associated with storage and pre-eruptive magmatic processes. The results of this study demonstrate the utility of isotopic analyses used in tandem with chemical data to reliably estimate timescales of magmatic processes in zoned olivine. The inversely correlated fractionation of Fe and Mg isotopes across chemical zonation, the negative relationship between Fe and Mg, and the large magnitude of fractionation are all indicators that Fe-Mg interdiffusion impacted the entirety of the grains. Isotopic analyses also revealed two distinct phases of diffusion processes where negligible fractionation was observed across the chemically flat cores and large fractionation trends were present near the rim. We

argue that both trends are a result of diffusion processes and reveal separate magmatic histories for Cordón Caulle. The first phase requires diffusive re-equilibration within an olivine that originally contained high Fo content cores (Fo_{85-90}) and lower, yet still mafic, Fo rims (Fo_{70-80}). While Fe-Mg interdiffusion can progress relatively quickly into olivine crystals, full equilibration of chemical zonation takes much longer. Results from this study suggest Cordón Caulle's magmatic system requires ~10,000-80,000 years to fully re-equilibrate and create the observed flat homogenous cores. These are first insights toward the long-term temporal evolution of Cordón Caulle's crystal mush storage system and suggest this system has existed on the orders of 10^4 years. While these grains may have undergone crystallization at much hotter temperatures, the basaltic chemistry and simple chemical zoning does not suggest extended storage, differentiation, or complex mixing interactions prior to mush incorporation, thus, supporting long-lived storage in a thermally buffered crystal mush to re-equilibrate. The second diffusive phase recorded in these grains occurs between the homogenized cores (Fo_{70-80}) and their evolved rims where isotopic data reported significant fractionation. Estimated timescales reveal late-stage processes of a final crystal growth episode on the order of months to <12 years prior to eruption (with one scenario of 30 years) and could be corroborated by similar pre-eruptive processes recorded in clinopyroxene rim growths and seismic and uplift unrest signals. Isotopic analyses paired with diffusion chronometry has advanced our understanding about Cordón Caulle's storage system, pre-eruptive processes, and long-term evolution.

Future Work

While this study has progressed our understanding of the diffusive processes affecting olivine grains and the timescales different phases are re-equilibrating, there are several advancements that could improve this study in the future. Next steps would be to obtain EBSD analyses on the

isotopic and Fo profiles to retrieve axial information (*c*- vs *ab*-axis). This would allow the proper diffusion coefficient to be selected for each individual grain, and thus, narrow the range of timescale estimates. This step is currently in progress. Another direction to advance this study would be to build upon the Fo diffusion modeling by incorporating isotopic modeling to corroborate timescales and refine any complexities in the transect profiles. This work is in progress and requires modeling the ratio of ^{56}Fe and ^{54}Fe diffusivities using the following equation from Richter et al., (1999):

$$\frac{D_H}{D_L}=\left(\frac{M_L}{M_H}\right)^{\beta} \quad \text{(Eq. 7)}$$

where D is the diffusion coefficient, L and H are the light and heavy isotopes of the same element, respectively (^{54}Fe, ^{56}Fe), M is the mass of the isotopes in atomic mass units, and beta (β) is a dimensionless empirical constant (Richter et al., 1999; Richter et al., 2016; Watkins & Antonelli, 2021).

Lastly, another direction to advance this study would be to investigate the mechanisms behind generating systematically light Fe isotopes observed in the olivine phase (Fig. 4.4). As discussed in the Results section, Fe compositions are systematically lighter than comparable basalt standards (Oeser et al., 2015; Collinet et al., 2017). Sample PCC-18-15C has the most pronounced variation reaching up to ~1$^0/_{00}$ variation in δ^{56}Fe and δ^{57}Fe. The lighter compositions could be a consequence of an open magmatic system that has already experienced some form of differentiation or fractionation to alter the crystal mush's bulk composition toward systematically lighter Fe isotopes. However, we have argued for relatively closed-system processes at Cordón Caulle given its high Mg# in whole rock compositions, high Fo content olivine, and lack common chemical signatures for crystal fractionation, especially in trace element trends, within the enclaves themselves (Winslow et al., 2022). If the system had not undergone prior bulk

fractionation, the complementary heavy Fe isotopes must be within an alternative phase in the enclaves. Preliminary isotopic analyses of Fe-oxides revealed systematically heavier Fe compositions, thus, resolving these challenges at an initial level. Mass balance calculations would quantitatively confirm if the heavy isotopes in the oxides counteract for the light compositions in olivine and would contribute to this conceptual model. Investigation toward the variance in light isotopes across all samples would also further this research and is a focus of future work.

Table 4.1. Output of timescales for olivine Fo diffusion models across all variables (temperature and axial orientation).

Sample	920°C	970°C	Axis	Length (µm)
PCC-18-16-1_oliv 1 line 2	9 mo	2.5 mo	D*c*	151
	4.5 yr	1.3 yr	D*ab*	
PCC-18-16-1_oliv 3 line 1	7 mo	2 mo	D*c*	165
	3.4 yr	1 yr	D*ab*	
PCC-18-17A-1_oliv 10 line 1	2.25 yr	8 mo	D*c*	160
	12 yr	4.5 yr	D*ab*	
PCC-18-15C_oliv 1 line 1	5 yr	1.5 yr	D*c*	226
	30 yr	9.5 yr	D*ab*	

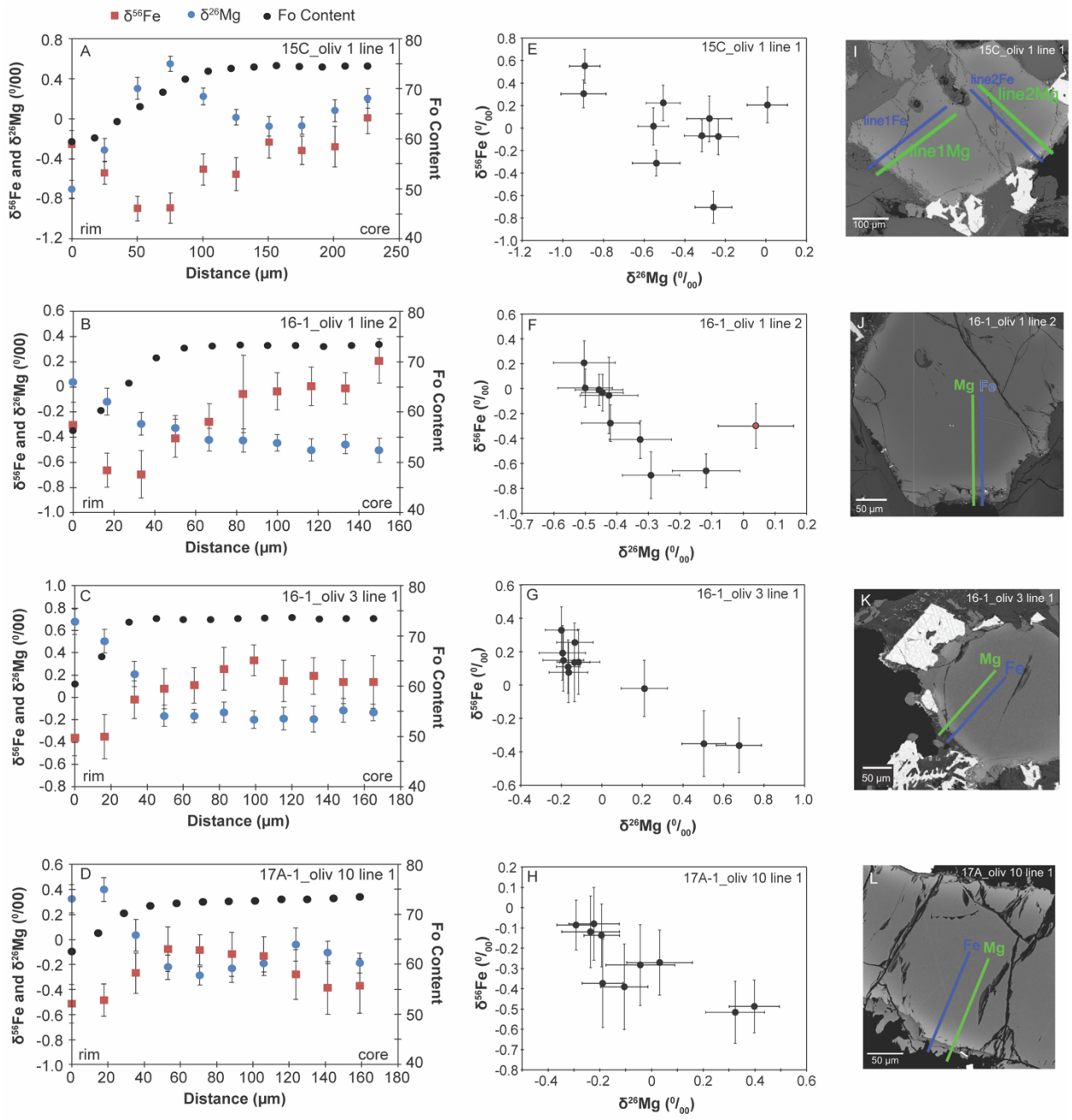

Figure 4.1. Compilation of isotopic ratios, Fo content, Fe and Mg ratios, BSE images with the location of respective isotopic transects. (A-D) display negligible core fractionation with large fractionation at the rims and chemical zonation correlates with fractionation trends. (E-H) Fe and Mg ratios for individual grains displaying negative correlations indicative of diffusion processes. Panel (F) passes over Fe-oxide near the rim which is reflected in the data as the red point. (I-L) BSE maps of selected grains with the isotopic transect locations and where Fo profiles were collected. Error bars represent analytical uncertainty (2 SD).

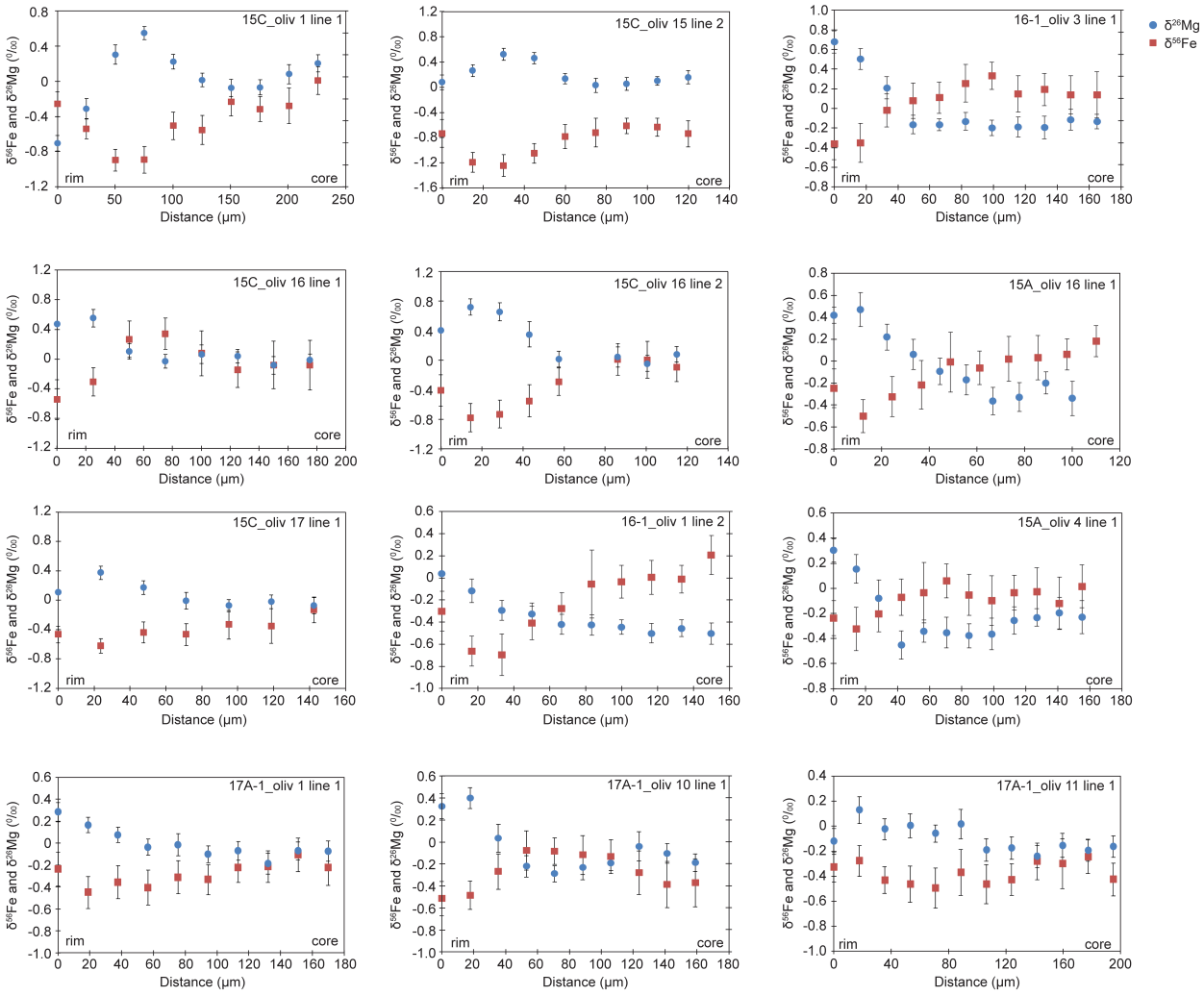

Figure 4.2. Fe and Mg isotopic profiles. Similar trends across all four samples showing negligible fractionation in the cores of the grains and a distinct shift with large fractionation at the rims of the grains. Error bars represent analytical uncertainty (2 SD).

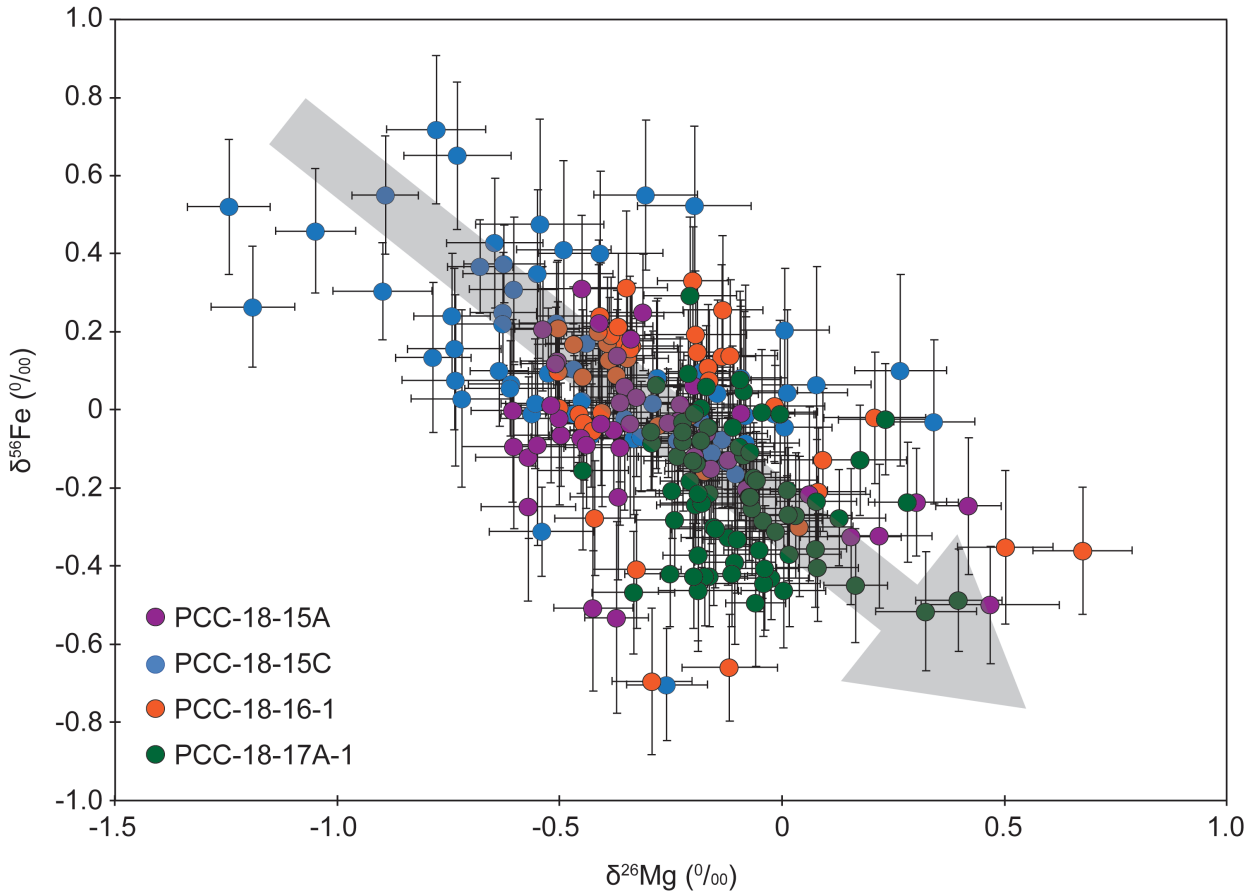

Figure 4.3. Mg and Fe ratios for all grains within the four analyzed samples. Error bars represent analytical uncertainty (2 SD). Figure displays negative correlation across all samples and grains indicative of diffusion-driven processes.

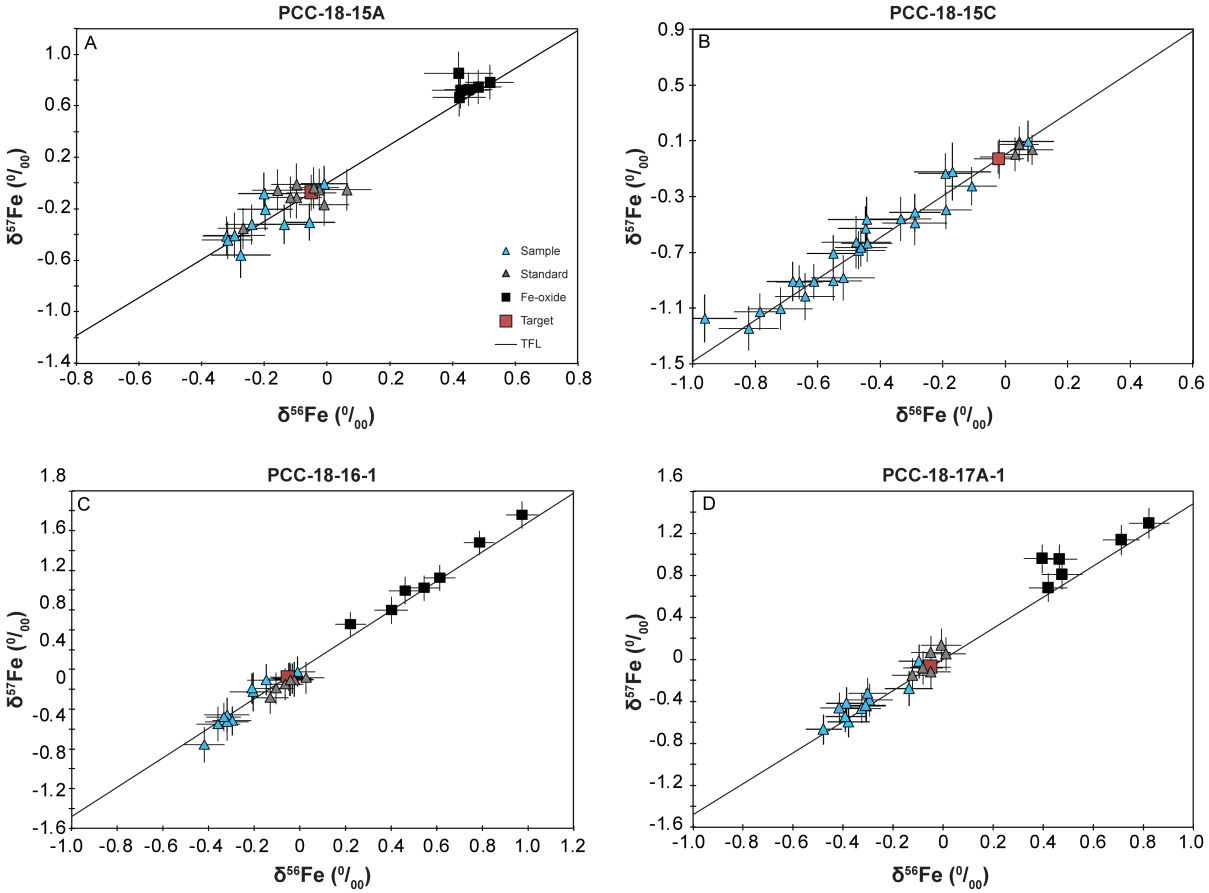

Figure 4.4. Ratios of Fe isotopes for olivine and Fe-oxide grains compared to standard concentrations. Error bars represent analytical uncertainty (2 SD). Olivine grains display systematically light concentrations and Fe-oxides display systematically heavy concentrations. TFL is the terrestrial fractionation line.

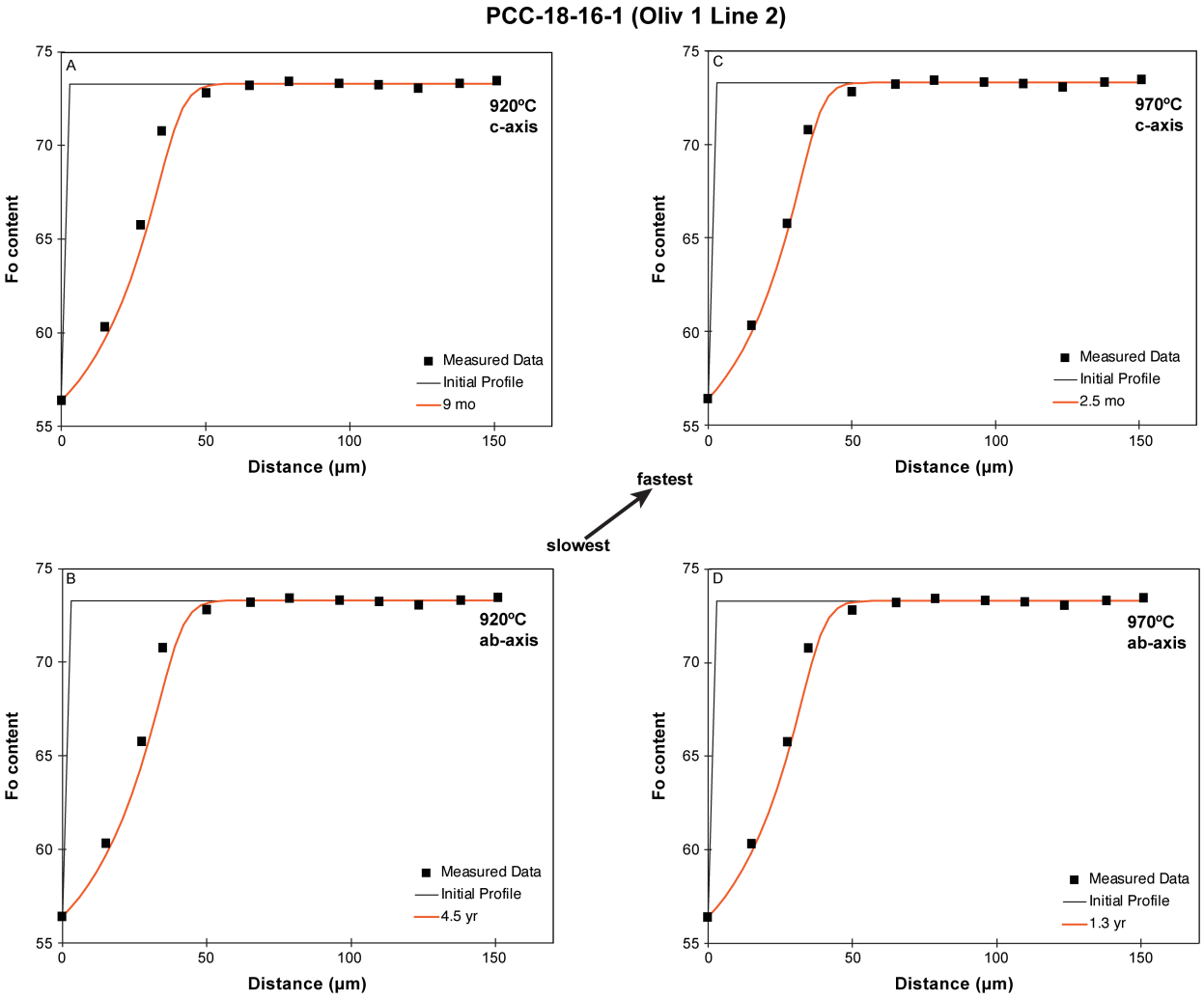

Figure 4.5. Results of diffusion modeling approach using Eq. 5 for sample PCC-18-16-1 (olivine 1, line 2). Measured data are the Fo profiles collected via EPMA across the isotopic transects. Panels (A, B) display results for diffusivities under 920°C temperatures but varying axial orientations. Panels (C, D) display results for diffusivities under 970°C temperatures but varying axial orientations. Panel (B) provides the maximum timescale estimate using the lower temperature and slower axial orientation for Fe-Mg diffusion. Panel (C) provides minimum timescale estimate using the higher temperature and fastest axial orientation.

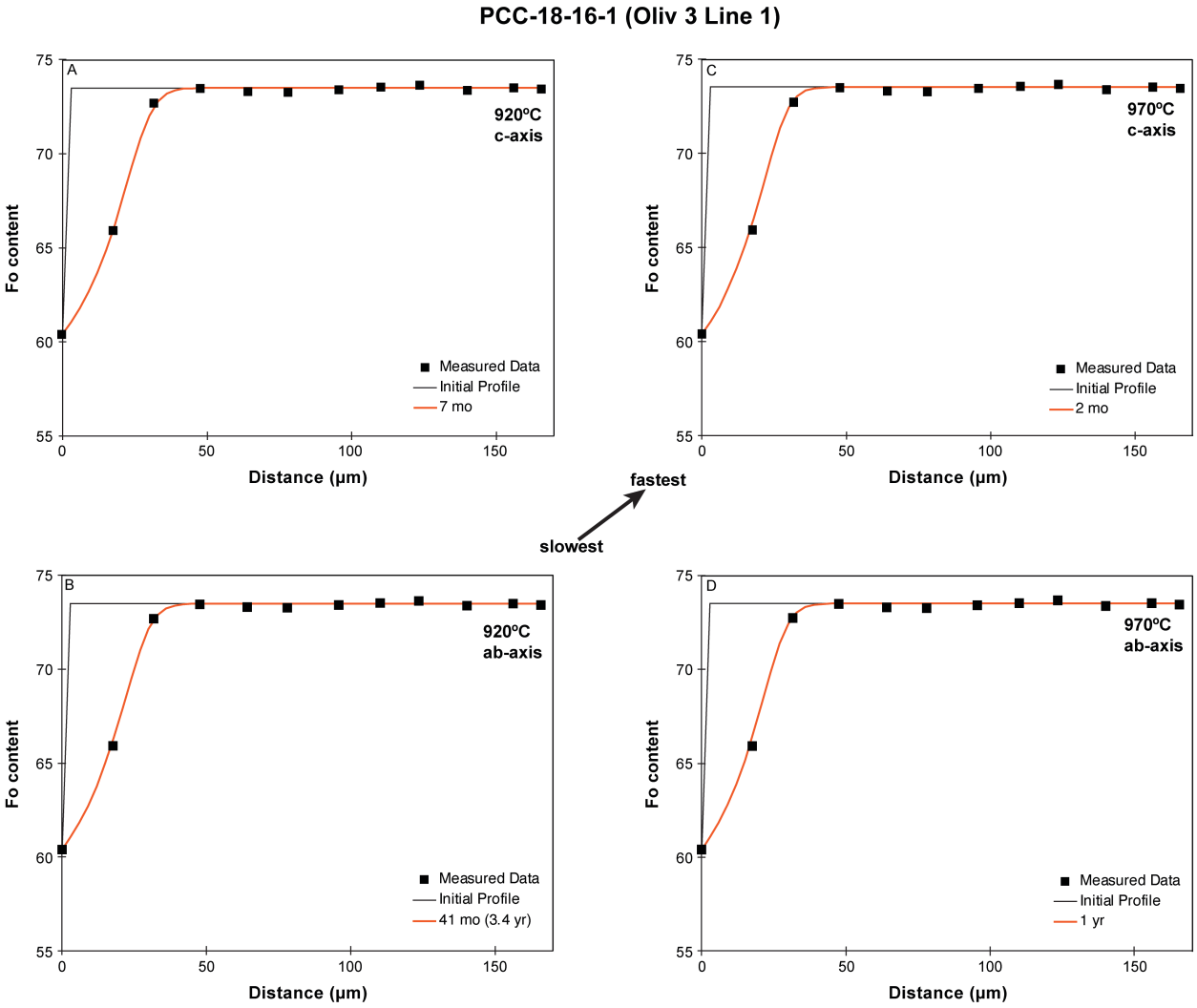

Figure 4.6. Results of diffusion modeling approach using Eq. 5 for sample PCC-18-16-1 (olivine 3, line 1). Measured data are the Fo profiles collected via EPMA across the isotopic transects. Panels (A, B) display results for diffusivities under 920°C temperatures but varying axial orientations. Panels (C, D) display results for diffusivities under 970°C temperatures but varying axial orientations. Panel (B) provides the maximum timescale estimate using the lower temperature and slower axial orientation for Fe-Mg diffusion. Panel (C) provides minimum timescale estimate using the higher temperature and fastest axial orientation.

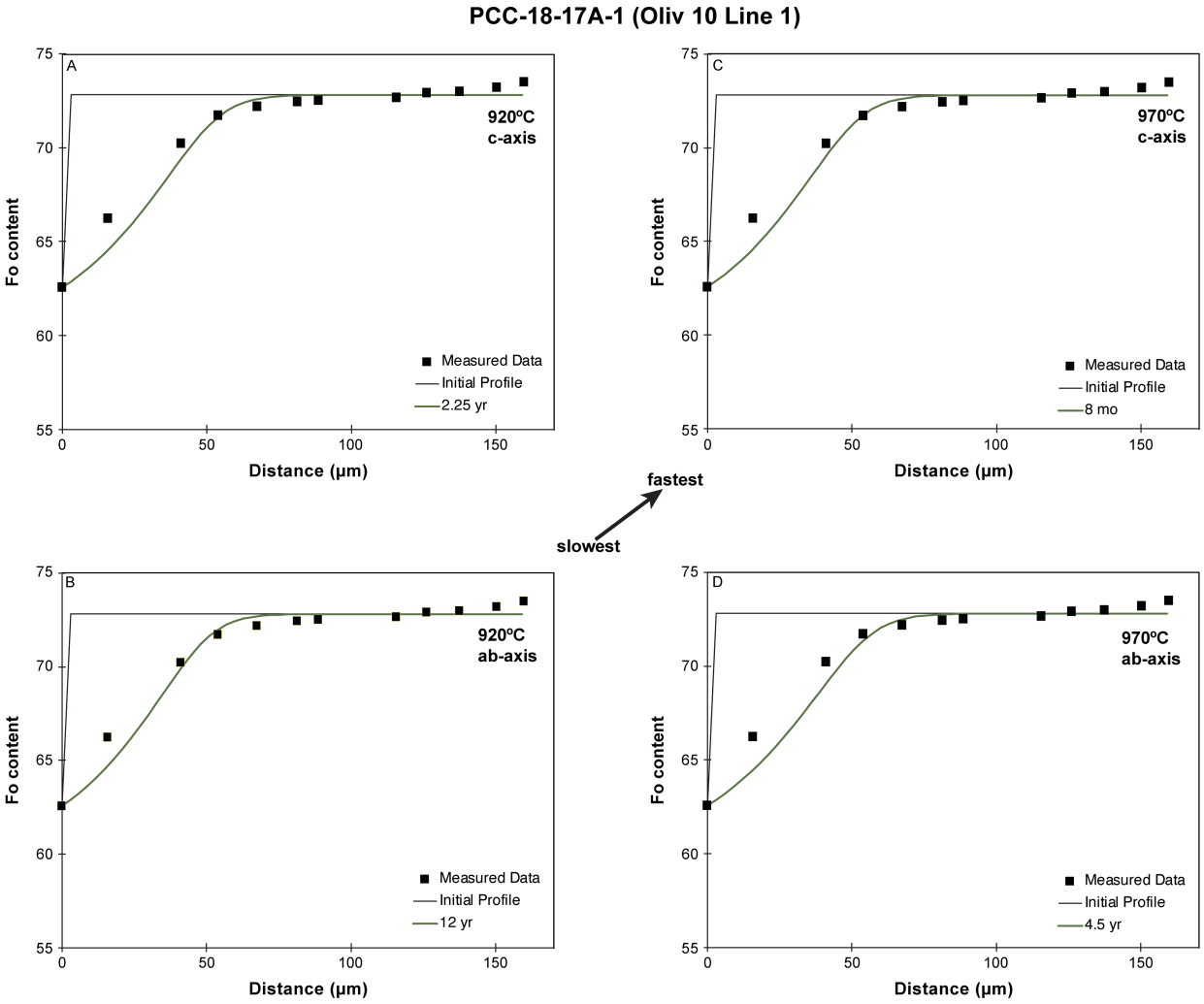

Figure 4.7. Results of diffusion modeling approach using Eq. 5 for sample PCC-18-17A-1 (olivine 10, line 1). Measured data are the Fo profiles collected via EPMA across the isotopic transects. Panels (A, B) display results for diffusivities under 920°C temperatures but varying axial orientations. Panels (C, D) display results for diffusivities under 970°C temperatures but varying axial orientations. Panel (B) provides the maximum timescale estimate using the lower temperature and slower axial orientation for Fe-Mg diffusion. Panel (C) provides minimum timescale estimate using the higher temperature and fastest axial orientation.

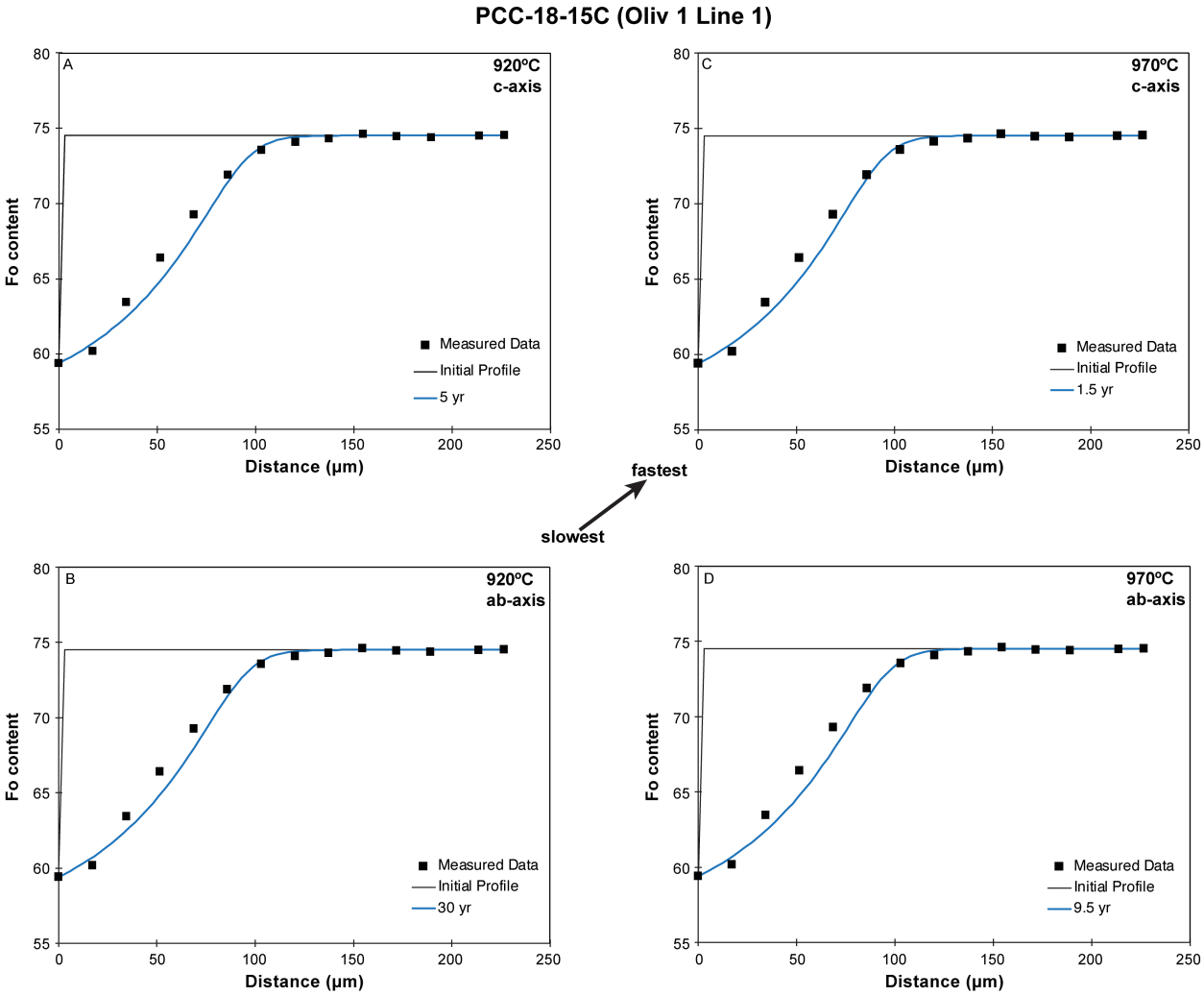

Figure 4.8. Results of diffusion modeling approach using Eq. 5 for sample PCC-18-15C (olivine 1, line 1). Measured data are the Fo profiles collected via EPMA across the isotopic transects. Panels (A, B) display results for diffusivities under 920°C temperatures but varying axial orientations. Panels (C, D) display results for diffusivities under 970°C temperatures but varying axial orientations. Panel (B) provides the maximum timescale estimate using the lower temperature and slower axial orientation for Fe-Mg diffusion. Panel (C) provides minimum timescale estimate using the higher temperature and fastest axial orientation.

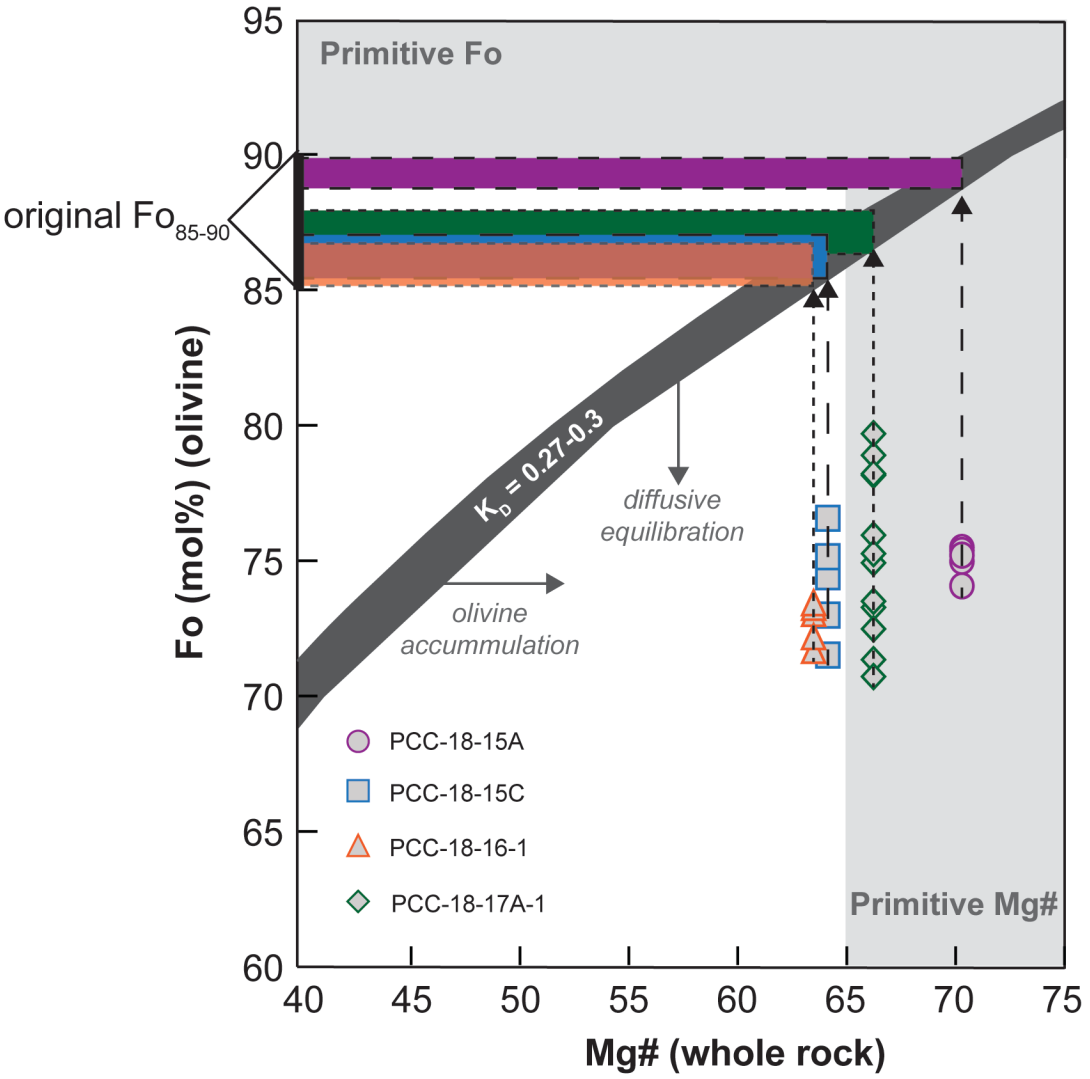

Figure 4.9. Mg# of the whole rock vs Fo content of olivine grains from four samples. Samples plot offset from melt-liquid equilibrium line and have been affected by diffusive equilibration. Reassessment of their initial compositions results in original Fo content of Fo_{85-90}. Mg# calculated on molar basis ((Mg/(Mg + Fe)*100)) and assumed 20% Fe^{3+}. Grey rectangles indicate primitive compositions from Schmidt & Jagoutz (2017).

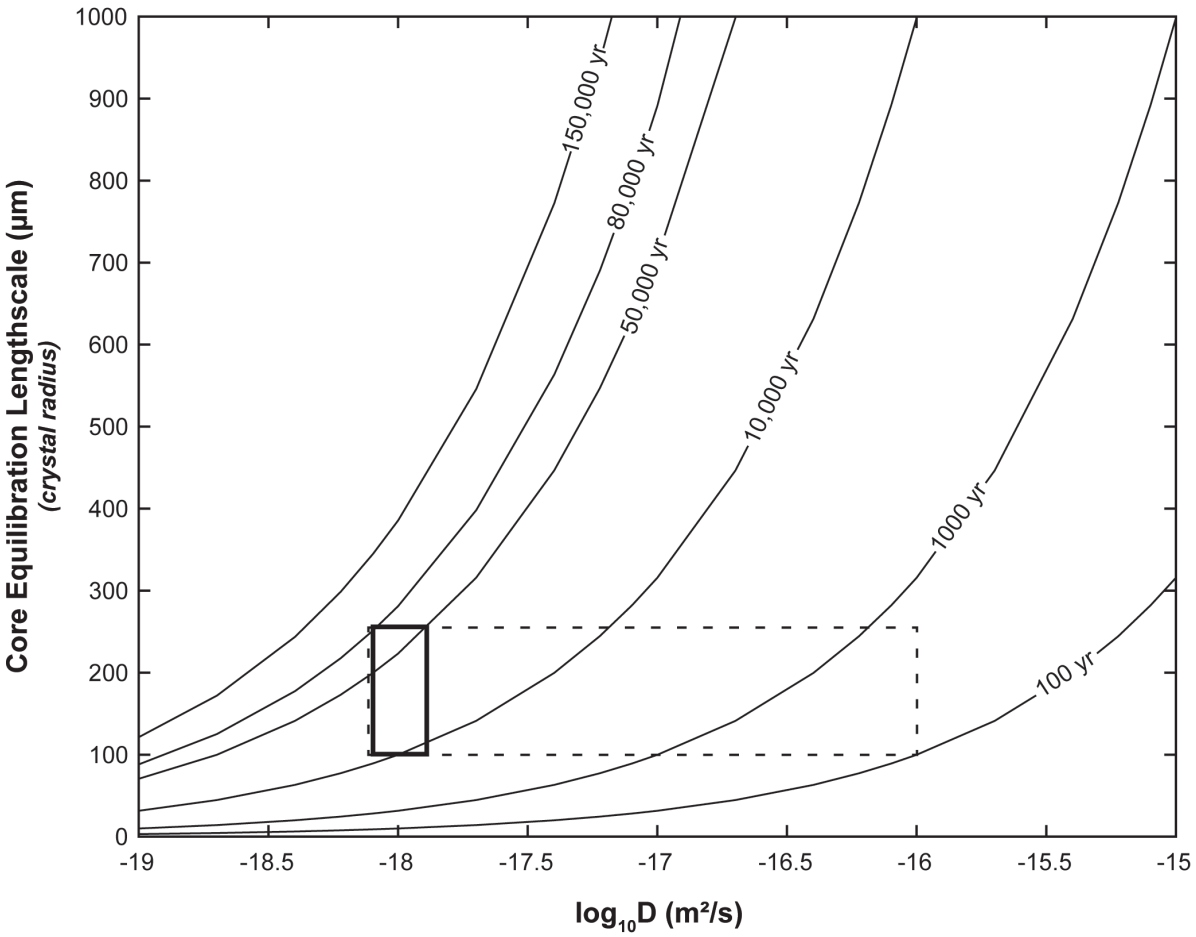

Figure 4.10. Equilibrium length scale for olivine under shallow mush conditions (black box) and typical basalt conditions (dashed box). Length scale is estimated using an initially zoned olivine grain with ~10% variation from core to rim. Equilibration assumes final concentration in the interior of the crystal is within 1% of the rim concentration. Equilibration timescale calculated from Eq. 6 and for shallow mush conditions (~100-300 MPA, 920-970ºC) reports ~10,000-80,000 years.

ESM 4.1. fs-LA-MC-ICP-MS Fe and Mg isotopic ratios for olivine transects.

Sample	δ56Fe [‰]	2 σ	δ26Mg [‰]	2 σ2
016_17A-1_ol11_2023-01-09	-0.43	0.13	-0.16	0.09
	-0.24	0.13	-0.19	0.09
	-0.30	0.20	-0.15	0.09
	-0.28	0.15	-0.24	0.09
	-0.43	0.13	-0.17	0.09
	-0.46	0.15	-0.19	0.09
	-0.37	0.18	0.02	0.12
	-0.50	0.16	-0.06	0.07
	-0.46	0.15	0.00	0.09
	-0.43	0.11	-0.02	0.08
	-0.28	0.12	0.13	0.11
	-0.33	0.12	-0.12	0.10
018_17A-1_ol10_2023-01-09	-0.37	0.22	-0.19	0.08
	-0.39	0.21	-0.11	0.09
	-0.28	0.20	-0.04	0.13
	-0.14	0.15	-0.19	0.07
	-0.12	0.18	-0.24	0.11
	-0.09	0.12	-0.29	0.07
	-0.08	0.18	-0.22	0.10
	-0.27	0.16	0.03	0.13
	-0.49	0.13	0.40	0.10
	-0.52	0.15	0.32	0.11
020_17A-1_ol10-2_2023-01-09	-0.27	0.17	0.02	0.09
	-0.31	0.15	-0.15	0.10
	-0.36	0.16	-0.05	0.08
	-0.17	0.14	-0.06	0.08
	-0.21	0.19	0.01	0.09
	-0.18	0.15	-0.21	0.07
	-0.04	0.17	-0.17	0.08
	-0.03	0.11	-0.22	0.08
	-0.21	0.15	-0.16	0.11
	-0.25	0.17	-0.07	0.09
	-0.42	0.14	-0.11	0.07
	-0.08	0.17	-0.18	0.09
022_17A-1_ol13_2023-01-09	-0.15	0.21	-0.45	0.10
	-0.47	0.16	-0.33	0.09
	-0.21	0.12	-0.25	0.08
	-0.42	0.14	-0.25	0.10
	-0.43	0.13	-0.20	0.08
	-0.44	0.14	-0.04	0.13
	-0.40	0.14	0.08	0.09
	-0.24	0.16	0.08	0.09
	-0.13	0.14	0.18	0.11
	-0.02	0.14	0.23	0.11
024_17A-1_ol14-1_2023-01-09	-0.01	0.24	0.00	0.08
	-0.12	0.15	-0.09	0.12
	0.05	0.20	-0.09	0.12
	0.09	0.16	-0.21	0.09
	0.29	0.20	-0.21	0.10
	0.06	0.16	-0.17	0.06
	0.01	0.19	-0.18	0.07
	-0.01	0.16	-0.05	0.13
	-0.09	0.13	-0.10	0.08
	-0.18	0.12	-0.06	0.14
027_17A-1_ol14-2_2023-01-09	-0.04	0.21	-0.11	0.11
	0.08	0.23	-0.09	0.09
	-0.01	0.19	-0.20	0.08
	-0.06	0.15	-0.29	0.10
	0.06	0.22	-0.28	0.10
	-0.24	0.17	-0.18	0.09
	-0.13	0.23	-0.20	0.11
	-0.05	0.18	-0.22	0.12
029_17A-1_ol1_2023-01-09	-0.22	0.16	-0.07	0.09
	-0.11	0.15	-0.07	0.08
	-0.21	0.14	-0.19	0.09
	-0.22	0.14	-0.07	0.09
	-0.33	0.14	-0.10	0.08
	-0.31	0.15	-0.02	0.10
	-0.41	0.16	-0.04	0.07
	-0.36	0.15	0.08	0.07
	-0.45	0.15	0.16	0.07
	-0.24	0.15	0.28	0.09

Sample	δ56Fe [‰]	2 σ	δ26Mg [‰]	2 σ2
009_15A_ol4_2023-01-10	0.02	0.17	-0.23	0.13
	-0.12	0.21	-0.20	0.13
	-0.03	0.19	-0.23	0.07
	-0.03	0.14	-0.26	0.11
	-0.10	0.20	-0.36	0.13
	-0.05	0.16	-0.38	0.10
	0.06	0.14	-0.35	0.12
	-0.04	0.24	-0.34	0.09
	-0.07	0.14	-0.45	0.11
	-0.20	0.14	-0.08	0.14
	-0.32	0.17	0.15	0.11
	-0.24	0.14	0.30	0.09
014_15A_ol15_2023-01-10	-0.06	0.13	-0.50	0.11
	-0.12	0.21	-0.57	0.12
	-0.09	0.26	-0.55	0.05
	0.00	0.23	-0.61	0.09
	-0.09	0.21	-0.60	0.12
	-0.02	0.22	-0.50	0.13
	-0.25	0.24	-0.57	0.11
	-0.51	0.21	-0.42	0.09
	-0.53	0.24	-0.37	0.07
	-0.22	0.21	-0.37	0.11
019_15A_ol16_2023-01-10	0.18	0.14	-0.34	0.16
	0.06	0.14	-0.20	0.10
	0.03	0.20	-0.33	0.13
	0.02	0.20	-0.36	0.12
	-0.06	0.15	-0.17	0.14
	-0.01	0.27	-0.09	0.12
	-0.22	0.22	0.06	0.14
	-0.32	0.18	0.22	0.12
	-0.50	0.15	0.47	0.16
	-0.25	0.18	0.42	0.07
021_15A_ol25_2023-01-10	-0.09	0.16	-0.44	0.10
	0.01	0.20	-0.52	0.10
	-0.04	0.16	-0.41	0.09
	0.14	0.14	-0.37	0.08
	0.12	0.15	-0.50	0.09
	0.21	0.16	-0.54	0.08
	0.12	0.15	-0.51	0.08
	0.22	0.21	-0.41	0.10
	0.31	0.19	-0.45	0.10
	0.25	0.15	-0.31	0.09
	-0.15	0.19	-0.16	0.07
	-0.13	0.17	-0.12	0.09
015_16-1_ol1-1_2023-01-11	0.13	0.20	-0.35	0.09
	0.18	0.13	-0.37	0.08
	0.17	0.15	-0.47	0.07
	0.16	0.16	-0.34	0.09
	0.13	0.16	-0.39	0.08
	0.17	0.17	-0.39	0.06
	0.19	0.15	-0.38	0.09
	0.16	0.19	-0.34	0.11
	0.09	0.17	-0.37	0.08
	-0.04	0.12	-0.28	0.12
	-0.16	0.20	-0.17	0.09
	0.01	0.14	-0.02	0.11
017_16-1_ol1-2_2023-01-11	0.21	0.18	-0.50	0.10
	-0.01	0.13	-0.46	0.08
	0.00	0.15	-0.50	0.09
	-0.03	0.15	-0.45	0.07
	-0.05	0.31	-0.43	0.09
	-0.28	0.15	-0.42	0.09
	-0.41	0.15	-0.33	0.10
	-0.70	0.19	-0.29	0.09
	-0.66	0.14	-0.12	0.11
	-0.30	0.18	0.04	0.12
019_16-1_ol2_2023-01-11	0.20	0.17	-0.41	0.07
	0.10	0.18	-0.50	0.15
	0.08	0.17	-0.45	0.09
	0.24	0.14	-0.41	0.14
	0.31	0.20	-0.35	0.09
	0.21	0.19	-0.37	0.08
	-0.01	0.24	-0.40	0.13
	-0.01	0.16	-0.21	0.09
	-0.21	0.16	0.08	0.11
	-0.13	0.18	0.09	0.10

Sample	δ56Fe [‰]	2 σ	δ26Mg [‰]	2 σ2
021_16-1_ol3-1_2023-01-11	0.14	0.24	-0.13	0.08
	0.14	0.19	-0.12	0.11
	0.19	0.16	-0.19	0.11
	0.15	0.19	-0.19	0.10
	0.33	0.14	-0.20	0.08
	0.26	0.19	-0.13	0.09
	0.11	0.16	-0.17	0.06
	0.08	0.18	-0.16	0.10
	-0.02	0.17	0.21	0.11
	-0.35	0.20	0.50	0.11
	-0.36	0.16	0.68	0.11
014_15C-ol16_2022-06-16	-0.08	0.34	-0.01	0.08
	-0.08	0.32	-0.08	0.12
	-0.14	0.24	0.04	0.09
	0.08	0.30	0.06	0.12
	0.34	0.21	-0.03	0.09
	0.27	0.25	0.10	0.10
	-0.31	0.19	0.55	0.12
	-0.54	0.27	0.48	0.14
016_15C-ol16_2022-06-16	-0.09	0.20	0.08	0.10
	0.01	0.25	-0.05	0.11
	0.01	0.21	0.04	0.14
	-0.29	0.19	0.02	0.11
	-0.55	0.22	0.35	0.17
	-0.73	0.19	0.65	0.12
	-0.78	0.19	0.72	0.11
	-0.41	0.21	0.40	0.14
019_15C-ol15_2022-06-16	-0.68	0.12	0.37	0.07
	-0.49	0.23	0.41	0.11
	-0.60	0.18	0.31	0.10
	-0.74	0.16	0.24	0.09
	-0.63	0.14	0.25	0.07
	-0.53	0.17	0.09	0.10
	-0.45	0.14	0.02	0.09
	-0.56	0.13	-0.01	0.07
	-0.43	0.13	-0.07	0.09
	-0.61	0.16	0.07	0.10
	-0.63	0.18	0.22	0.11
021_15C-ol15_2022-06-16	-0.74	0.21	0.16	0.11
	-0.64	0.14	0.10	0.07
	-0.61	0.12	0.05	0.10
	-0.72	0.23	0.03	0.11
	-0.78	0.19	0.13	0.08
	-1.05	0.16	0.46	0.09
	-1.24	0.17	0.52	0.09
	-1.19	0.15	0.26	0.09
	-0.73	0.22	0.08	0.12
026_15C-ol17_2022-06-16	-0.13	0.17	-0.07	0.11
	-0.35	0.24	-0.02	0.09
	-0.33	0.19	-0.07	0.08
	-0.47	0.15	-0.01	0.11
	-0.44	0.14	0.17	0.09
	-0.62	0.10	0.37	0.09
	-0.47	0.11	0.11	0.09
029_15C-ol1_2022-06-16	0.01	0.16	0.20	0.10
	-0.28	0.20	0.08	0.11
	-0.32	0.14	-0.07	0.09
	-0.24	0.16	-0.08	0.10
	-0.55	0.17	0.02	0.08
	-0.51	0.16	0.22	0.08
	-0.89	0.15	0.55	0.08
	-0.90	0.12	0.30	0.11
	-0.54	0.11	-0.31	0.12
	-0.26	0.14	-0.70	0.09
031_15C-ol1_2022-06-16	-0.18	0.11	0.10	0.08
	-0.12	0.11	-0.13	0.08
	-0.02	0.13	-0.01	0.09
	-0.16	0.11	-0.11	0.09
	-0.10	0.17	-0.17	0.08
	-0.09	0.13	-0.11	0.06
	-0.18	0.18	-0.02	0.08
	-0.20	0.20	0.52	0.13
	-0.65	0.17	0.43	0.11

ESM 4.2. fs-LA-MC-ICP-MS Fe isotopic ratios for Fe-oxides.

Sample	δ56Fe [‰]	2 σ	δ57Fe [‰]	2σ
042_17A-1_ox1_2023-01-09	0.71	0.07	1.14	0.14
044_17A-1_ox2_2023-01-09	0.40	0.07	0.96	0.14
045_17A-1_ox3_2023-01-09	0.46	0.07	0.95	0.14
047_17A-1_ox4_2023-01-09	0.42	0.08	0.68	0.14
050_17A-1_ox5_2023-01-09	0.47	0.08	0.81	0.15
052_17A-1_ox6_2023-01-09	0.82	0.08	1.30	0.15
050_15A_ox1_2023-01-10	0.42	0.11	0.85	0.17
052_15A_ox1b_2023-01-10	0.42	0.08	0.66	0.15
054_15A_ox2_2023-01-10	0.52	0.08	0.78	0.13
056_15A_ox3_2023-01-10	0.48	0.07	0.74	0.13
057_15A_ox4_2023-01-10	0.45	0.08	0.73	0.13
059_15A_ox5_2023-01-10	0.43	0.09	0.72	0.14
044_16-1_ox1_2023-01-11	0.98	0.07	1.56	0.14
046_16-1_ox2_2023-01-11	0.46	0.07	0.80	0.14
048_16-1_ox3_2023-01-11	0.40	0.07	0.60	0.14
050_16-1_ox4_2023-01-11	0.54	0.07	0.82	0.13
051_16-1_ox5_2023-01-11	0.61	0.07	0.92	0.13
053_16-1_ox6_2023-01-11	0.22	0.07	0.46	0.13
055_16-1_ox7_2023-01-11	0.79	0.07	1.28	0.12

ESM 4.3. UNR EPMA olivine Fo profiles for respective isotopic transects.

SAMPLE	Fo content	RELDIST	Na2O	Al2O3	SiO2	MgO	P2O5	CaO	FeO	MnO	NiO	Cr2O3	TiO2	O	TOTAL
PCC-18-15C_oliv1_line1	74.52	0.00	b.d.l.	0.03	38.33	37.84	0.01	0.19	23.07	0.37	0.05	0.01	b.d.l.	0.00	99.90
PCC-18-15C_oliv1_line1	74.48	17.17	0.01	0.03	38.10	37.78	0.03	0.19	23.08	0.40	0.04	0.01	b.d.l.	b.d.l.	99.66
PCC-18-15C_oliv1_line1	74.37	34.35	b.d.l.	0.04	38.20	37.74	0.04	0.19	23.18	0.40	0.05	0.01	b.d.l.	b.d.l.	99.85
PCC-18-15C_oliv1_line1	74.42	51.53	b.d.l.	0.03	37.96	37.87	0.04	0.19	23.20	0.41	0.05	b.d.l.	b.d.l.	0.00	99.74
PCC-18-15C_oliv1_line1	74.60	68.71	b.d.l.	0.03	38.19	37.84	b.d.l.	0.19	22.97	0.36	0.04	b.d.l.	b.d.l.	b.d.l.	99.63
PCC-18-15C_oliv1_line1	74.29	85.86	b.d.l.	0.03	38.02	37.79	b.d.l.	0.19	23.32	0.40	0.05	b.d.l.	b.d.l.	b.d.l.	99.79
PCC-18-15C_oliv1_line1	74.07	103.06	b.d.l.	0.03	38.28	37.59	b.d.l.	0.18	23.46	0.38	0.04	0.01	b.d.l.	0.00	99.97
PCC-18-15C_oliv1_line1	73.54	120.21	b.d.l.	0.03	38.01	37.29	b.d.l.	0.19	23.92	0.42	0.05	b.d.l.	b.d.l.	0.00	99.91
PCC-18-15C_oliv1_line1	71.87	137.41	b.d.l.	0.03	38.02	36.11	0.02	0.18	25.19	0.45	0.04	b.d.l.	b.d.l.	0.00	100.04
PCC-18-15C_oliv1_line1	69.26	154.57	b.d.l.	0.03	37.45	34.34	b.d.l.	0.18	27.17	0.51	0.03	b.d.l.	b.d.l.	0.00	99.72
PCC-18-15C_oliv1_line1	66.39	171.76	0.01	0.03	36.90	32.63	0.02	0.18	29.44	0.63	0.02	b.d.l.	b.d.l.	b.d.l.	99.87
PCC-18-15C_oliv1_line1	63.43	189.26	0.01	0.03	36.73	30.65	b.d.l.	0.17	31.51	0.66	b.d.l.	b.d.l.	b.d.l.	b.d.l.	99.77
PCC-18-15C_oliv1_line1	60.17	213.79	b.d.l.	0.03	35.78	28.61	0.03	0.17	33.75	0.74	b.d.l.	b.d.l.	b.d.l.	b.d.l.	99.10
PCC-18-15C_oliv1_line1	59.40	226.62	0.01	0.04	35.81	28.12	0.06	0.17	34.26	0.74	b.d.l.	b.d.l.	b.d.l.	0.00	99.23
PCC-18-15C_oliv1_line2	73.21	0.00	b.d.l.	0.03	38.05	37.12	b.d.l.	0.19	24.21	0.41	0.04	b.d.l.	b.d.l.	b.d.l.	100.07
PCC-18-15C_oliv1_line2	73.57	18.29	b.d.l.	0.03	38.32	37.04	0.02	0.19	23.72	0.41	0.05	0.01	b.d.l.	b.d.l.	99.80
PCC-18-15C_oliv1_line2	73.80	35.08	b.d.l.	0.03	38.04	37.42	0.04	0.19	23.68	0.42	0.04	b.d.l.	b.d.l.	b.d.l.	99.87
PCC-18-15C_oliv1_line2	73.83	50.92	b.d.l.	0.03	37.98	37.39	b.d.l.	0.20	23.63	0.40	0.05	b.d.l.	b.d.l.	0.00	99.66
PCC-18-15C_oliv1_line2	73.61	66.96	b.d.l.	0.03	38.39	37.62	0.01	0.19	24.04	0.39	0.05	b.d.l.	b.d.l.	b.d.l.	100.72
PCC-18-15C_oliv1_line2	73.67	81.93	b.d.l.	0.03	38.39	37.27	0.02	0.19	23.74	0.37	0.05	b.d.l.	b.d.l.	b.d.l.	100.05
PCC-18-15C_oliv1_line2	73.29	98.74	b.d.l.	0.04	38.01	37.01	0.12	0.21	24.04	0.41	0.04	b.d.l.	b.d.l.	b.d.l.	99.86
PCC-18-15C_oliv1_line2	73.04	117.50	b.d.l.	0.04	38.42	36.92	0.05	0.20	24.30	0.44	0.05	b.d.l.	b.d.l.	b.d.l.	100.42
PCC-18-15C_oliv1_line2	72.98	132.30	b.d.l.	0.03	38.18	36.96	b.d.l.	0.20	24.40	0.45	0.04	b.d.l.	b.d.l.	0.00	100.28
PCC-18-15C_oliv1_line2	73.33	148.96	b.d.l.	0.03	38.36	37.08	0.06	0.19	24.03	0.39	0.04	b.d.l.	b.d.l.	b.d.l.	100.18
PCC-18-15C_oliv1_line2	73.78	164.50	b.d.l.	0.03	38.50	37.66	b.d.l.	0.19	23.85	0.37	0.04	b.d.l.	b.d.l.	b.d.l.	100.66
PCC-18-15C_oliv1_line2	73.49	180.85	b.d.l.	0.03	38.67	37.16	b.d.l.	0.19	23.89	0.42	0.04	b.d.l.	b.d.l.	b.d.l.	100.41
PCC-18-15C_oliv1_line2	68.72	197.20	b.d.l.	0.03	37.53	34.14	b.d.l.	0.18	27.70	0.52	0.04	b.d.l.	b.d.l.	b.d.l.	100.14
PCC-18-15C_oliv1_line2	58.36	213.73	b.d.l.	0.04	36.29	27.80	0.02	0.16	35.36	0.77	b.d.l.	b.d.l.	b.d.l.	b.d.l.	100.44
PCC-18-15C_oliv1_line2	52.72	223.32	0.01	0.05	35.55	24.62	0.03	0.17	39.37	0.81	b.d.l.	b.d.l.	b.d.l.	b.d.l.	100.61
PCC-18-16-1_oliv3_line 1	73.42	0.00	b.d.l.	0.04	38.14	37.40	0.05	0.20	24.13	0.40	0.04	b.d.l.	b.d.l.	b.d.l.	100.39
PCC-18-16-1_oliv3_line 1	73.50	17.65	0.01	0.05	38.13	36.96	0.05	0.20	23.75	0.38	0.04	b.d.l.	b.d.l.	0.00	99.56
PCC-18-16-1_oliv3_line 1	73.37	31.79	b.d.l.	0.05	38.39	37.24	0.07	0.20	24.09	0.44	0.04	b.d.l.	b.d.l.	b.d.l.	100.54
PCC-18-16-1_oliv3_line 1	73.64	47.76	b.d.l.	0.04	38.49	37.53	0.06	0.19	23.94	0.41	0.05	b.d.l.	b.d.l.	b.d.l.	100.71
PCC-18-16-1_oliv3_line 1	73.53	64.26	b.d.l.	0.03	38.26	37.37	0.05	0.20	23.98	0.36	0.03	b.d.l.	b.d.l.	b.d.l.	100.30
PCC-18-16-1_oliv3_line 1	73.41	78.08	0.01	0.03	38.63	37.42	0.07	0.19	24.16	0.42	0.05	0.01	b.d.l.	b.d.l.	100.99
PCC-18-16-1_oliv3_line 1	73.27	95.76	b.d.l.	0.03	38.46	37.59	0.02	0.21	24.45	0.42	0.04	b.d.l.	b.d.l.	b.d.l.	101.22
PCC-18-16-1_oliv3_line 1	73.30	110.26	b.d.l.	0.03	38.55	37.34	0.04	0.19	24.25	0.42	0.05	b.d.l.	b.d.l.	0.00	100.87
PCC-18-16-1_oliv3_line 1	73.46	123.56	0.00	0.03	38.20	37.22	0.02	0.19	23.97	0.42	0.04	b.d.l.	b.d.l.	b.d.l.	100.10
PCC-18-16-1_oliv3_line 1	72.71	140.21	b.d.l.	0.03	38.37	36.92	0.02	0.19	24.70	0.44	0.04	b.d.l.	b.d.l.	b.d.l.	100.71
PCC-18-16-1_oliv3_line 1	65.91	156.17	b.d.l.	0.03	37.21	32.43	b.d.l.	0.15	29.90	0.62	0.03	b.d.l.	b.d.l.	0.00	100.38
PCC-18-16-1_oliv3_line 1	60.38	165.73	0.01	0.04	36.64	28.99	0.01	0.15	33.90	0.75	0.02	b.d.l.	b.d.l.	b.d.l.	100.52
PCC-18-16-1_oliv1_line 1	73.48	0.00	0.05	0.21	38.28	36.85	0.05	0.27	23.72	0.40	0.05	b.d.l.	b.d.l.	b.d.l.	99.87
PCC-18-16-1_oliv1_line 1	73.07	12.72	0.01	0.04	37.98	37.00	0.09	0.22	24.31	0.41	0.04	b.d.l.	b.d.l.	b.d.l.	100.10
PCC-18-16-1_oliv1_line 1	73.11	28.49	0.01	0.07	37.89	37.03	0.11	0.23	24.28	0.43	0.04	b.d.l.	b.d.l.	b.d.l.	100.09
PCC-18-16-1_oliv1_line 1	73.51	44.67	b.d.l.	0.04	38.17	37.33	0.08	0.20	23.99	0.36	0.04	b.d.l.	b.d.l.	b.d.l.	100.21
PCC-18-16-1_oliv1_line 1	73.33	63.01	b.d.l.	0.04	38.50	37.34	0.02	0.20	24.21	0.41	0.04	0.01	b.d.l.	b.d.l.	100.79
PCC-18-16-1_oliv1_line 1	73.24	80.29	0.00	0.04	38.42	37.02	0.04	0.21	24.11	0.41	0.05	b.d.l.	b.d.l.	b.d.l.	100.30
PCC-18-16-1_oliv1_line 1	73.13	93.92	0.01	0.04	37.83	37.17	0.03	0.20	24.34	0.43	0.05	b.d.l.	b.d.l.	0.00	100.09
PCC-18-16-1_oliv1_line 1	73.28	108.19	0.01	0.04	38.43	37.30	0.03	0.19	24.24	0.40	0.05	b.d.l.	b.d.l.	b.d.l.	100.71
PCC-18-16-1_oliv1_line 1	73.34	122.12	b.d.l.	0.04	38.38	37.15	0.03	0.21	24.07	0.41	0.04	b.d.l.	b.d.l.	0.00	100.33
PCC-18-16-1_oliv1_line 1	72.97	136.56	0.01	0.03	38.27	37.09	0.01	0.21	24.50	0.45	0.04	b.d.l.	b.d.l.	b.d.l.	100.60
PCC-18-16-1_oliv1_line 1	69.48	150.99	b.d.l.	0.04	37.96	34.69	0.01	0.19	27.16	0.50	0.04	b.d.l.	b.d.l.	0.00	100.59
PCC-18-16-1_oliv1_line 1	61.77	165.37	0.01	0.04	36.63	29.80	b.d.l.	0.15	32.89	0.68	0.03	b.d.l.	b.d.l.	b.d.l.	100.23
PCC-18-16-1_oliv1_line 2	73.46	0.00	b.d.l.	0.03	38.61	37.32	b.d.l.	0.19	24.03	0.40	0.05	b.d.l.	b.d.l.	b.d.l.	100.64
PCC-18-16-1_oliv1_line 2	73.30	15.09	0.00	0.04	38.59	37.06	0.02	0.20	24.06	0.43	0.05	0.01	b.d.l.	b.d.l.	100.47
PCC-18-16-1_oliv1_line 2	73.05	27.55	0.01	0.04	38.52	37.09	0.02	0.19	24.39	0.35	0.04	b.d.l.	b.d.l.	b.d.l.	100.66
PCC-18-16-1_oliv1_line 2	73.24	34.81	0.01	0.03	38.78	36.95	0.02	0.19	24.07	0.40	0.05	b.d.l.	b.d.l.	b.d.l.	100.51
PCC-18-16-1_oliv1_line 2	73.29	50.06	0.00	0.03	38.70	36.91	0.01	0.20	23.98	0.40	0.05	b.d.l.	b.d.l.	b.d.l.	100.30
PCC-18-16-1_oliv1_line 2	73.41	65.21	0.01	0.04	38.65	37.12	b.d.l.	0.19	23.96	0.41	0.05	b.d.l.	b.d.l.	b.d.l.	100.43
PCC-18-16-1_oliv1_line 2	73.19	78.77	b.d.l.	0.03	38.32	37.15	0.01	0.20	24.25	0.43	0.04	b.d.l.	b.d.l.	b.d.l.	100.43
PCC-18-16-1_oliv1_line 2	72.81	96.15	0.01	0.04	38.53	36.82	0.02	0.20	24.52	0.47	0.04	b.d.l.	b.d.l.	b.d.l.	100.63
PCC-18-16-1_oliv1_line 2	70.77	109.86	0.01	0.03	38.03	35.52	0.02	0.18	26.15	0.51	0.05	b.d.l.	b.d.l.	b.d.l.	100.49
PCC-18-16-1_oliv1_line 2	65.76	123.55	0.01	0.04	37.69	32.29	0.01	0.17	29.96	0.62	0.03	b.d.l.	b.d.l.	0.00	100.82
PCC-18-16-1_oliv1_line 2	60.31	138.03	0.01	0.04	36.58	28.82	0.04	0.17	33.81	0.71	0.02	b.d.l.	b.d.l.	0.00	100.20
PCC-18-16-1_oliv1_line 2	56.38	150.85	0.04	0.05	36.64	26.12	0.02	0.17	36.02	0.84	0.01	0.01	b.d.l.	0.00	99.94
PCC-18-17A-1_oliv10_line1	73.48	0.00	b.d.l.	0.03	38.44	37.60	0.06	0.19	24.20	0.44	0.07	0.01	b.d.l.	0.00	101.04
PCC-18-17A-1_oliv10_line1	73.18	15.76	0.01	0.03	38.53	37.35	0.07	0.19	24.40	0.39	0.05	b.d.l.	b.d.l.	b.d.l.	101.03
PCC-18-17A-1_oliv10_line1	72.97	41.07	b.d.l.	0.03	38.64	37.21	0.02	0.19	24.57	0.42	0.05	0.01	b.d.l.	b.d.l.	101.13
PCC-18-17A-1_oliv10_line1	72.92	53.89	0.00	0.03	38.06	37.05	0.07	0.19	24.53	0.43	0.05	0.01	b.d.l.	b.d.l.	100.42
PCC-18-17A-1_oliv10_line1	72.64	67.34	0.01	0.03	38.44	37.12	0.04	0.19	24.93	0.44	0.05	0.01	b.d.l.	0.00	101.26
PCC-18-17A-1_oliv10_line1	72.51	81.33	0.01	0.03	38.10	36.84	0.04	0.17	24.90	0.44	0.05	b.d.l.	b.d.l.	b.d.l.	100.59
PCC-18-17A-1_oliv10_line1	72.45	88.55	0.01	0.03	38.39	36.69	0.03	0.18	24.88	0.45	0.06	b.d.l.	b.d.l.	b.d.l.	100.71
PCC-18-17A-1_oliv10_line1	72.17	115.48	0.01	0.03	38.59	36.62	0.02	0.18	25.18	0.48	0.04	0.01	b.d.l.	b.d.l.	101.15
PCC-18-17A-1_oliv10_line1	71.70	126.13	b.d.l.	0.03	38.20	36.26	0.02	0.17	25.51	0.45	0.05	b.d.l.	b.d.l.	b.d.l.	100.70
PCC-18-17A-1_oliv10_line1	70.20	137.44	0.01	0.03	38.03	35.25	0.01	0.18	26.67	0.53	0.05	b.d.l.	b.d.l.	b.d.l.	100.74
PCC-18-17A-1_oliv10_line1	66.22	150.22	0.01	0.03	37.35	32.66	0.02	0.16	29.70	0.63	0.04	b.d.l.	b.d.l.	b.d.l.	100.60
PCC-18-17A-1_oliv10_line1	62.55	159.62	b.d.l.	0.03	36.66	30.22	0.02	0.14	32.26	0.72	0.03	b.d.l.	b.d.l.	b.d.l.	100.08
PCC-18-17A-1_oliv10_line2	71.46	0.00	b.d.l.	0.03	38.19	36.19	0.03	0.18	25.76	0.51	0.06	b.d.l.	b.d.l.	0.00	100.95
PCC-18-17A-1_oliv10_line2	71.19	14.29	b.d.l.	0.03	38.00	35.99	0.04	0.18	25.97	0.47	0.05	b.d.l.	b.d.l.	b.d.l.	100.74
PCC-18-17A-1_oliv10_line2	70.91	28.59	0.00	0.03	37.87	35.77	0.04	0.17	26.16	0.48	0.04	b.d.l.	b.d.l.	0.00	100.57
PCC-18-17A-1_oliv10_line2	70.67	42.87	0.00	0.03	38.04	35.52	0.03	0.18	26.27	0.51	0.04	b.d.l.	b.d.l.	0.00	100.63
PCC-18-17A-1_oliv10_line2	70.42	57.17	0.01	0.03	37.95	35.52	0.04	0.19	26.60	0.47	0.05	0.01	b.d.l.	0.00	100.87
PCC-18-17A-1_oliv10_line2	70.48	71.47	b.d.l.	0.03	37.83	35.39	0.05	0.18	26.43	0.48	0.05	0.01	b.d.l.	b.d.l.	100.45
PCC-18-17A-1_oliv10_line2	69.94	85.75	0.01	0.04	37.90	35.27	0.06	0.18	27.02	0.50	0.04	0.01	b.d.l.	b.d.l.	101.02
PCC-18-17A-1_oliv10_line2	69.95	100.04	0.01	0.04	37.82	35.11	0.05	0.19	26.89	0.51	0.05	b.d.l.	b.d.l.	b.d.l.	100.67
PCC-18-17A-1_oliv10_line2	69.92	114.34	0.01	0.03	37.83	35.10	0.05	0.18	26.92	0.50	0.04	b.d.l.	b.d.l.	0.00	100.67
PCC-18-17A-1_oliv10_line2	69.94	128.64	0.00	0.03	37.62	34.99	0.06	0.18	26.81	0.52	0.05	b.d.l.	b.d.l.	b.d.l.	100.27
PCC-18-17A-1_oliv10_line2	69.14	142.92	0.01	0.03	38.05	34.40	0.03	0.18	27.37	0.60	0.04	b.d.l.	b.d.l.	b.d.l.	100.70
PCC-18-17A-1_oliv10_line2	65.91	157.21	b.d.l.	0.03	37.52	32.55	b.d.l.	0.16	30.02	0.65	0.04	b.d.l.	b.d.l.	b.d.l.	100.97
PCC-18-17A-1_oliv10_line2	62.65	168.43	b.d.l.	0.04	36.55	30.46	0.03	0.15	32.38	0.69	0.03	b.d.l.	b.d.l.	b.d.l.	100.33

ESM 4.4. Qualitative maps with relative concentrations of phosphorous (P) in olivine. Light red indicates higher P concentrations. Dark red indicates lower P concentrations.

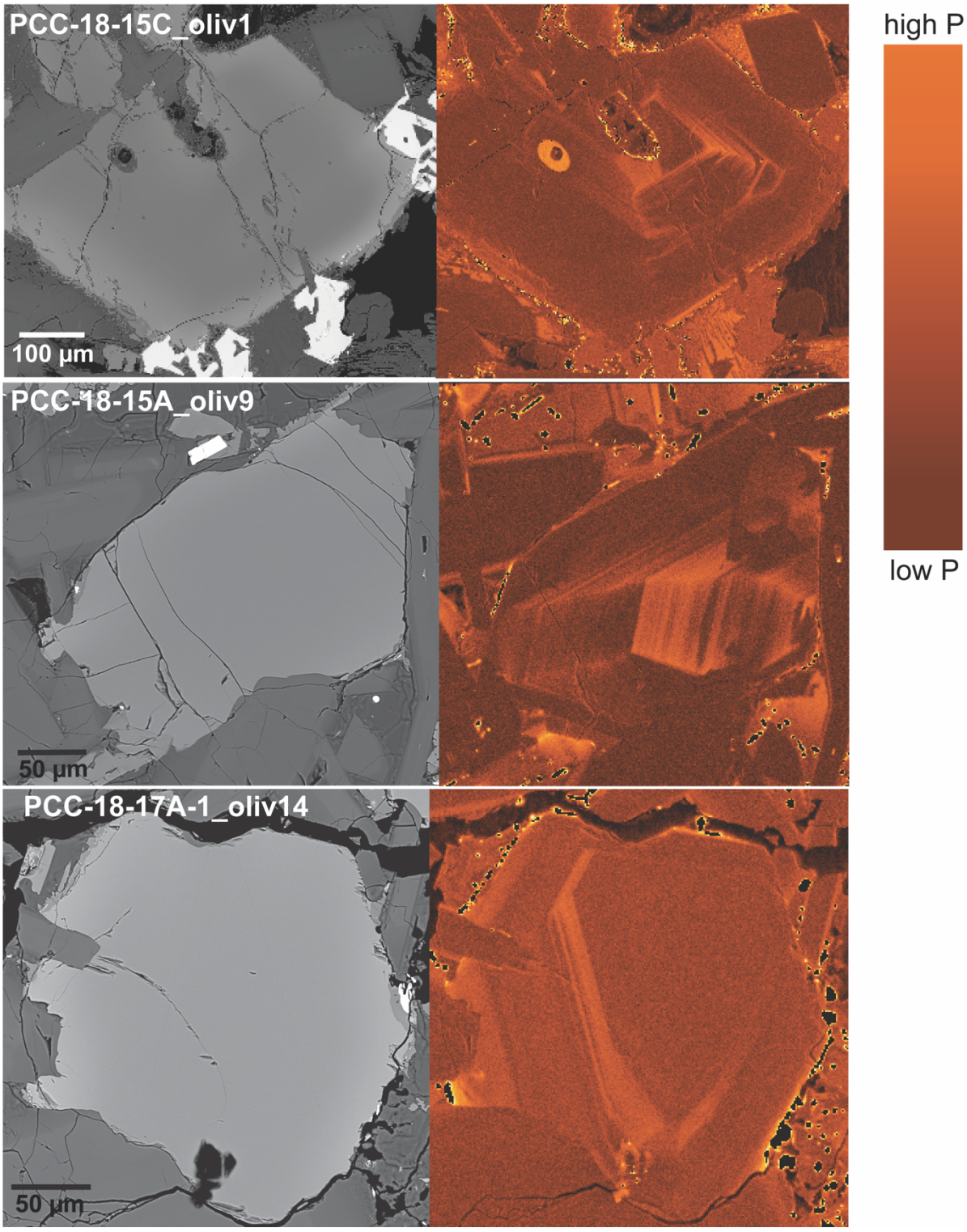

References

Basualto, D., Tassara, A., Lazo-Gil, J., Franco-Marin, L., Cardona, C., San Martín, J., Gil-Cruz, F., Calabi-Floddy, M., & Farías, C. (2023). Anatomy of a high-silica eruption as observed by a local seismic network: The June 2011 Puyehue–Cordón Caulle event (southern Andes, Chile). *Solid Earth*, *14*(1), 69–87. https://doi.org/10.5194/se-14-69-2023

Castro, J. M., Schipper, C. I., Mueller, S. P., Militzer, A. S., Amigo, A., Parejas, C. S., & Jacob, D. (2013). Storage and eruption of near-liquidus rhyolite magma at Cordón Caulle, Chile. *Bulletin of Volcanology*, *75*(4), 702. https://doi.org/10.1007/s00445-013-0702-9

Christopher, T. E., Blundy, J., Cashman, K., Cole, P., Edmonds, M., Smith, P. J., Sparks, R. S. J., & Stinton, A. (2015). Crustal-scale degassing due to magma system destabilization and magma-gas decoupling at Soufrière Hills Volcano, Montserrat. *Geochemistry, Geophysics, Geosystems*, *16*(9), 2797–2811. https://doi.org/10.1002/2015GC005791

Collinet, M., Charlier, B., Namur, O., Oeser, M., Médard, E., & Weyer, S. (2017). Crystallization history of enriched shergottites from Fe and Mg isotope fractionation in olivine megacrysts. *Geochimica et Cosmochimica Acta*, *207*, 277–297. https://doi.org/10.1016/j.gca.2017.03.029

Cooper, K. M., & Kent, A. J. R. (2014). Rapid remobilization of magmatic crystals kept in cold storage. *Nature*, *506*(7489), 480–483. https://doi.org/10.1038/nature12991

Costa, F., Dohmen, R., & Chakraborty, S. (2008). Time Scales of Magmatic Processes from Modeling the Zoning Patterns of Crystals. *Reviews in Mineralogy and Geochemistry*, *69*(1), 545–594. https://doi.org/10.2138/rmg.2008.69.14

Costa, F., Shea, T., & Ubide, T. (2020). Diffusion chronometry and the timescales of magmatic processes. *Nature Reviews Earth & Environment*, *1*(4), Article 4. https://doi.org/10.1038/s43017-020-0038-x

Dauphas, N., Teng, F.-Z., & Arndt, N. T. (2010). Magnesium and iron isotopes in 2.7 Ga Alexo komatiites: Mantle signatures, no evidence for Soret diffusion, and identification of diffusive transport in zoned olivine. *Geochimica et Cosmochimica Acta*, *74*(11), 3274–3291. https://doi.org/10.1016/j.gca.2010.02.031

Delgado, F. (2021). Rhyolitic volcano dynamics in the Southern Andes: Contributions from 17 years of InSAR observations at Cordón Caulle volcano from 2003 to 2020. *Journal of South American Earth Sciences*, *106*, 102841. https://doi.org/10.1016/j.jsames.2020.102841

Delgado, F., Pritchard, M. E., Basualto, D., Lazo, J., Córdova, L., & Lara, L. E. (2016). Rapid reinflation following the 2011–2012 rhyodacite eruption at Cordón Caulle volcano (Southern Andes) imaged by InSAR: Evidence for magma reservoir refill. *Geophysical Research Letters*, *43*(18), 9552–9562. https://doi.org/10.1002/2016GL070066

Dohmen, R., Becker, H.-W., & Chakraborty, S. (2007). Fe–Mg diffusion in olivine I: Experimental determination between 700 and 1,200°C as a function of composition, crystal orientation and

oxygen fugacity. *Physics and Chemistry of Minerals*, *34*(6), 389–407. https://doi.org/10.1007/s00269-007-0157-7

Dohmen, R., & Chakraborty, S. (2007). Fe–Mg diffusion in olivine II: Point defect chemistry, change of diffusion mechanisms and a model for calculation of diffusion coefficients in natural olivine. *Physics and Chemistry of Minerals*, *34*(6), 409–430. https://doi.org/10.1007/s00269-007-0158-6

Donovan, J. J., Singer, J. W., & Armstrong, J. T. (2016). A new EPMA method for fast trace element analysis in simple matrices. *American Mineralogist*, *101*(8), 1839–1853. https://doi.org/10.2138/am-2016-5628

Farquharson, J. I., James, M. R., & Tuffen, H. (2015). Examining rhyolite lava flow dynamics through photo-based 3D reconstructions of the 2011–2012 lava flowfield at Cordón-Caulle, Chile. *Journal of Volcanology and Geothermal Research*, *304*, 336–348. https://doi.org/10.1016/j.jvolgeores.2015.09.004

Hartley, M. E., Morgan, D. J., Maclennan, J., Edmonds, M., & Thordarson, T. (2016). Tracking timescales of short-term precursors to large basaltic fissure eruptions through Fe–Mg diffusion in olivine. *Earth and Planetary Science Letters*, *439*, 58–70. https://doi.org/10.1016/j.epsl.2016.01.018

Herd, C. D. K. (2008). Basalts as Probes of Planetary Interior Redox State. *Reviews in Mineralogy and Geochemistry*, *68*(1), 527–553. https://doi.org/10.2138/rmg.2008.68.19

Holness, M. B., Stock, M. J., & Geist, D. (2019). Magma chambers versus mush zones: Constraining the architecture of sub-volcanic plumbing systems from microstructural analysis of crystalline enclaves. *Philosophical Transactions of the Royal Society A: Mathematical, Physical and Engineering Sciences*, *377*(2139), 20180006. https://doi.org/10.1098/rsta.2018.0006

Huebner, J. S., & Sato, M. (1970). The oxygen fugacity-temperature relationships of manganese oxide and nickel oxide buffers1. *American Mineralogist*, *55*(5–6), 934–952.

Jay, J., Costa, F., Pritchard, M., Lara, L., Singer, B., & Herrin, J. (2014). Locating magma reservoirs using InSAR and petrology before and during the 2011–2012 Cordón Caulle silicic eruption. *Earth and Planetary Science Letters*, *395*, 254–266. https://doi.org/10.1016/j.epsl.2014.03.046

Nakamura, A., & Schmalzried, H. (1983). On the nonstoichiometry and point defects of olivine. *Physics and Chemistry of Minerals*, *10*(1), 27–37. https://doi.org/10.1007/BF01204323

Oeser, M., Dohmen, R., Horn, I., Schuth, S., & Weyer, S. (2015). Processes and time scales of magmatic evolution as revealed by Fe–Mg chemical and isotopic zoning in natural olivines. *Geochimica et Cosmochimica Acta*, *154*, 130–150. https://doi.org/10.1016/j.gca.2015.01.025

Oeser, M., Ruprecht, P., & Weyer, S. (2018). Combined Fe-Mg chemical and isotopic zoning in olivine constraining magma mixing-to-eruption timescales for the continental arc volcano Irazú (Costa Rica) and Cr diffusion in olivine. *American Mineralogist*, *103*(4), 582–599. https://doi.org/10.2138/am-2018-6258

Richter, F., Chaussidon, M., Mendybaev, R., & Kite, E. (2016). Reassessing the cooling rate and geologic setting of Martian meteorites MIL 03346 and NWA 817. *Geochimica et Cosmochimica Acta*, *182*, 1–23. https://doi.org/10.1016/j.gca.2016.02.020

Richter, F. M., Dauphas, N., & Teng, F.-Z. (2009). Non-traditional fractionation of non-traditional isotopes: Evaporation, chemical diffusion and Soret diffusion. *Chemical Geology*, *258*(1), 92–103. https://doi.org/10.1016/j.chemgeo.2008.06.011

Richter, F. M., Liang, Y., & Davis, A. M. (1999). Isotope fractionation by diffusion in molten oxides. *Geochimica et Cosmochimica Acta*, *63*(18), 2853–2861. https://doi.org/10.1016/S0016-7037(99)00164-7

Roeder, P. L., & Emslie, R. F. (1970). Olivine-liquid equilibrium. *Contributions to Mineralogy and Petrology*, *29*(4), 275–289. https://doi.org/10.1007/BF00371276

Ruprecht, P., Bergantz, G. W., Cooper, K. M., & Hildreth, W. (2012). The Crustal Magma Storage System of Volcán Quizapu, Chile, and the Effects of Magma Mixing on Magma Diversity. *Journal of Petrology*, *53*(4), 801–840. https://doi.org/10.1093/petrology/egs002

Salas, P., Ruprecht, P., Hernández, L., & Rabbia, O. (2021). Out-of-sequence skeletal growth causing oscillatory zoning in arc olivines. *Nature Communications*, *12*, 4069. https://doi.org/10.1038/s41467-021-24275-6

Schipper, C. I., Castro, J. M., Kennedy, B. M., Tuffen, H., Whattam, J., Wadsworth, F. B., Paisley, R., Fitzgerald, R. H., Rhodes, E., Schaefer, L. N., Ashwell, P. A., Forte, P., Seropian, G., & Alloway, B. V. (2021). Silicic conduits as supersized tuffisites: Clastogenic influences on shifting eruption styles at Cordón Caulle volcano (Chile). *Bulletin of Volcanology*, *83*(2), 11. https://doi.org/10.1007/s00445-020-01432-1

Schmidt, M. W., & Jagoutz, O. (2017a). The global systematics of primitive arc melts. *Geochemistry, Geophysics, Geosystems*, *18*(8), 2817–2854. https://doi.org/10.1002/2016GC006699

Schmidt, M. W., & Jagoutz, O. (2017b). The global systematics of primitive arc melts. *Geochemistry, Geophysics, Geosystems*, *18*(8), 2817–2854. https://doi.org/10.1002/2016GC006699

Schwab, R., & Kustner, D. (1981). The equilibrium fugacities of important oxygen buffers in technology and petrology. *Neues Jahrb. Mineral. Abh.*, *140*, 111–142.

Shea, T., Hammer, J. E., Hellebrand, E., Mourey, A. J., Costa, F., First, E. C., Lynn, K. J., & Melnik, O. (2019). Phosphorus and aluminum zoning in olivine: Contrasting behavior of two nominally incompatible trace elements. *Contributions to Mineralogy and Petrology*, *174*(10), 85. https://doi.org/10.1007/s00410-019-1618-y

Shea, T., Lynn, K. J., & Garcia, M. O. (2015). Cracking the olivine zoning code: Distinguishing between crystal growth and diffusion. *Geology*, *43*(10), 935–938. https://doi.org/10.1130/G37082.1

Singer, B. S., Jicha, B. R., Harper, M. A., Naranjo, J. A., Lara, L. E., & Moreno-Roa, H. (2008). Eruptive history, geochronology, and magmatic evolution of the Puyehue-Cordón Caulle volcanic complex, Chile. *GSA Bulletin*, *120*(5–6), 599–618. https://doi.org/10.1130/B26276.1

Sio, C. K. I., Dauphas, N., Teng, F.-Z., Chaussidon, M., Helz, R. T., & Roskosz, M. (2013). Discerning crystal growth from diffusion profiles in zoned olivine by in situ Mg–Fe isotopic analyses. *Geochimica et Cosmochimica Acta*, *123*, 302–321. https://doi.org/10.1016/j.gca.2013.06.008

Teng, F.-Z., Dauphas, N., Helz, R. T., Gao, S., & Huang, S. (2011). Diffusion-driven magnesium and iron isotope fractionation in Hawaiian olivine. *Earth and Planetary Science Letters*, *308*(3), 317–324. https://doi.org/10.1016/j.epsl.2011.06.003

Teng, F.-Z., Wadhwa, M., & Helz, R. T. (2007). Investigation of magnesium isotope fractionation during basalt differentiation: Implications for a chondritic composition of the terrestrial mantle. *Earth and Planetary Science Letters*, *261*(1), 84–92. https://doi.org/10.1016/j.epsl.2007.06.004

Toplis, M. J. (2005). The thermodynamics of iron and magnesium partitioning between olivine and liquid: Criteria for assessing and predicting equilibrium in natural and experimental systems. *Contributions to Mineralogy and Petrology*, *149*(1), 22–39. https://doi.org/10.1007/s00410-004-0629-4

Tuffen, H., James, M. R., Castro, J. M., & Schipper, C. I. (2013). Exceptional mobility of an advancing rhyolitic obsidian flow at Cordón Caulle volcano in Chile. *Nature Communications*, *4*(1), Article 1. https://doi.org/10.1038/ncomms3709

Watkins, J. M., & Antonelli, M. A. (2021). Beyond Equilibrium: Kinetic Isotope Fractionation in High-Temperature Environments. *Elements*, *17*(6), 383–388. https://doi.org/10.2138/gselements.17.6.383

Welsch, B., Faure, F., Famin, V., Baronnet, A., & Bachèlery, P. (2013). Dendritic Crystallization: A Single Process for all the Textures of Olivine in Basalts? *Journal of Petrology*, *54*(3), 539–574. https://doi.org/10.1093/petrology/egs077

Weyer, S., & Seitz, H.-M. (2012). Coupled lithium- and iron isotope fractionation during magmatic differentiation. *Chemical Geology*, *294–295*, 42–50. https://doi.org/10.1016/j.chemgeo.2011.11.020

Winslow, H., Ruprecht, P., Gonnermann, H. M., Phelps, P. R., Muñoz-Saez, C., Delgado, F., Pritchard, M., & Amigo, A. (2022). Insights for crystal mush storage utilizing mafic enclaves from the 2011–12 Cordón Caulle eruption. *Scientific Reports*, *12*(1), Article 1. https://doi.org/10.1038/s41598-022-13305-y

Winslow, H., Ruprecht, P., Stelten, M., & Amigo, A. (2020). Evidence for primitive magma storage and eruption following prolonged equilibration in thickened crust. *Bulletin of Volcanology*, *82*(11), 69. https://doi.org/10.1007/s00445-020-01406-3

Zhou, X. R. (1981). Estimation of oxygen fugacity and its application in petrology. *Geol. Explor.*, *11*, 40–48.

Chapter 5

Conclusion

The mafic enclaves from Cordón Caulle present a unique opportunity to unravel crystal mush storage conditions and processes prior to eruption and give insight toward the mafic nature and origin behind rhyolitic magma generation. I present the first studies determining enclave characteristics, compositions, and distill pre-eruptive magmatic processes and storage constraints. Textural data, geochemistry, and quantitative constraints support the conceptual model that there is a crystal mush underlying Cordón Caulle and that it is directly fueling the shallow rhyolite melt lens cap. Cooling rates and diffusion modeling have revealed three distinct timescale estimates for varying processes operating in the storage system. Olivine core equilibration was used to determine a first estimate for the lifetime of the crystal mush by assuming diffusive re-equilibration had overprinted initial zonation. The lifetime was estimated at ~10,000-80,000 years. This provides a general estimate on the longevity of Cordón Caulle's underlying magma system and that mush assembly may have occurred on the order of tens of thousands of years ago. Puyehue-Cordón Caulle's entire eruptive history stretches back to ~300 ka, and the Cordón Caulle graben experienced both late Pleistocene activity (~54 ka) and Holocene eruptions (~6 ka – present) producing crystal-poor rhyolite (Singer et al., 2008). Cordón Caulle's rhyolitic eruptive activity coincides with our estimated timescales associated with mush assembly as well as continued mush sourced eruptions into present day. To further constrain mush assembly and longevity timescales, U-series methods would provide absolute ages for the crystals that are unaffected by thermal history complexities (Costa & Dungan, 2005;

Ruprecht & Cooper, 2012; Cooper & Kent, 2014). Future work in this direction could corroborate the diffusion estimates.

Thermometry and cooling rate data were used to determine timescales of cooling upon mush disaggregation and rhyolite incorporation. These data estimated that cooling lasted on the order of several hundred to ~1000 years with instantaneous cooling paths indicating enclaves were rapidly incorporated into the rhyolite with extended storage in the rhyolite prior to eruption. If alternative diffusivities are used, these timescales operate on the order of decades to ~300 years using the instantaneous cooling path. The variation is timescales highlights the need for improved understanding of Mg partitioning in plagioclase under varying An conditions. Regardless of which diffusivity is used, enclave incorporation is likely impacted by previous eruptions. Magma chamber dynamic models propose eruptive forces depressurize the magma chamber and increase the efficiency of melt-mush separation (Phelps et al., 2023). This increase in melt separation likely impacts mush disaggregation and incorporation into the rhyolite melt cap. Holocene eruptions (~6 ka-present; Singer et al., 2008) coincide with enclave incorporation timescales of several hundred to several thousand years.

Diffusion modeling in outer olivine rims reveals late-stage crystallization and differentiation occurs on the order of months to years prior to eruption. Nominally shallow pressure estimates calculated from the outer rim of clinopyroxene reflect ascent-driven crystallization in the conduit, corroborating the late-stage crystallization and differentiation.

Cordón Caulle preserves unique information toward rhyolite generation processes and the conditions required to undergo highly efficient differentiation. Similar to Cordón Caulle, Medicine Lake, CA exhibits a large compositional gap with gabbroic enclaves producing silicic eruptions (Grove & Donnelly-Nolan, 1986). Both systems contain shallow magma reservoirs and

highly crystalline mafic endmembers. This study reinforces the claims made in Grove & Donnelly-Nolan (1986), that high volumes of crystallization can occur over a minimal temperature change resulting in drastic differentiation steps. In Cordón Caulle's case, basalt short-circuited typical transcrustal differentiation paths and produced rhyolite in a single step. Experimental work from Grove & Donnelly-Nolan (1986) confirmed these processes only operate at shallow levels. This dissertation corroborates this finding using the shallow crystal-rich mush of Cordón Caulle and highlights the applicability of efficient differentiation at any shallow magma reservoir.

The tectonic environment at Cordón Caulle impacts its volcanic activity and composition. While Cordón Caulle is a part of a larger volcanic complex within a continental arc, local faulting produces an extensional fault-dominated region (Lara et al., 2004; 2006; Jay et al., 2014). The Holocene rhyolitic eruptions have all occurred within the faulted Cordón Caulle graben, and historic eruption vents are along fault lineaments (Jay et al., 2014). As explored in this study, crystal poor rhyolite from the historic eruptions are nearly-identical and proposed to all be sourced from the basaltic crystal mush (Castro et al., 2013; Winslow et al., 2022). It is likely the extensional environment and faulted nature of Cordón Caulle provides accessible pathways for magma migration (Lara et al., 2006). The unperturbed pathways may result in minimal differentiation at depth and preserves basaltic magma through its incorporation into the shallow mush.

This study provides a detailed look into the temporal evolution of crystal mush processes and storage constraints that has yet to be done on an active system and speaks to the utility of mineral-scale analyses to study crystal-rich volcanic systems. Cordón Caulle highlights the capabilities of differentiation in shallow mush systems regardless of tholeiitic or calc-alkaline

compositions. The petrologic constraints collected in this study will contribute toward improving numerical models of melt separation and subsurface magma flow as well as improving interpretations of surficial deformation signals. Together, these datasets will provide a more holistic view of the magmatic system at Cordón Caulle and improve interpretations of precursory eruptive signals, but will also contribute to our understanding of shallow mush systems globally.

References

Cooper, K. M., & Kent, A. J. R. (2014). Rapid remobilization of magmatic crystals kept in cold storage. *Nature*, *506*(7489), 480–483. https://doi.org/10.1038/nature12991

Costa, F., & Dungan, M. (2005). Short time scales of magmatic assimilation from diffusion modeling of multiple elements in olivine. *Geology*, *33*(10), 837. https://doi.org/10.1130/G21675.1

Grove, T. L., & Donnelly-Nolan, J. M. (1986). The evolution of young silicic lavas at Medicine Lake Volcano, California: Implications for the origin of compositional gaps in calc-alkaline series lavas. *Contributions to Mineralogy and Petrology*, *92*(3), 281–302. https://doi.org/10.1007/BF00572157

Jay, J., Costa, F., Pritchard, M., Lara, L., Singer, B., & Herrin, J. (2014). Locating magma reservoirs using InSAR and petrology before and during the 2011–2012 Cordón Caulle silicic eruption. *Earth and Planetary Science Letters*, *395*, 254–266. https://doi.org/10.1016/j.epsl.2014.03.046

Lara, L. E., Lavenu, A., Cembrano, J., & Rodríguez, C. (2006). Structural controls of volcanism in transversal chains: Resheared faults and neotectonics in the Cordón Caulle–Puyehue area (40.5°S), Southern Andes. *Journal of Volcanology and Geothermal Research*, *158*(1), 70–86. https://doi.org/10.1016/j.jvolgeores.2006.04.017

Lara, L. E., Naranjo, J. A., & Moreno, H. (2004). Rhyodacitic fissure eruption in Southern Andes (Cordón Caulle; 40.5°S) after the 1960 (Mw:9.5) Chilean earthquake: A structural interpretation. *Journal of Volcanology and Geothermal Research*, *138*(1–2), 127–138. https://doi.org/10.1016/j.jvolgeores.2004.06.009

Phelps, P. R., Gonnermann, H. M., Winslow, H., Ruprecht, P., Pritchard, M. E., Delgado, F., & Liao, Y. (2023). Feasibility of melt segregation from a crystal mush in response to the 2011-12 eruption at Cordon Caulle. *Geophysical Journal International (in review)*.

Ruprecht, P., & Cooper, K.M. (2012). Integrating the Uranium-Series and Elemental Diffusion Geochronometers in Mixed Magmas from Volcán Quizapu, Central Chile. *Journal of Petrology 53*, 841–871. https://doi.org/10.1093/petrology/egs001

Singer, B. S., Jicha, B. R., Harper, M. A., Naranjo, J. A., Lara, L. E., & Moreno-Roa, H. (2008). Eruptive history, geochronology, and magmatic evolution of the Puyehue-Cordon Caulle volcanic complex, Chile. *Geological Society of America Bulletin*, *120*(5–6), 599–618. https://doi.org/10.1130/B26276.1

Winslow, H., Ruprecht, P., Gonnermann, H. M., Phelps, P. R., Muñoz-Saez, C., Delgado, F., Pritchard, M., & Amigo, A. (2022). Insights for crystal mush storage utilizing mafic enclaves from the 2011–12 Cordón Caulle eruption. *Scientific Reports*, *12*(1), 9734. https://doi.org/10.1038/s41598-022-13305-y